MAX-PLANCK-INSTITUT
FÜR METEOROLOGIE

Kilometer-Scale Ocean Turbulence and Waves in the North and South Atlantic

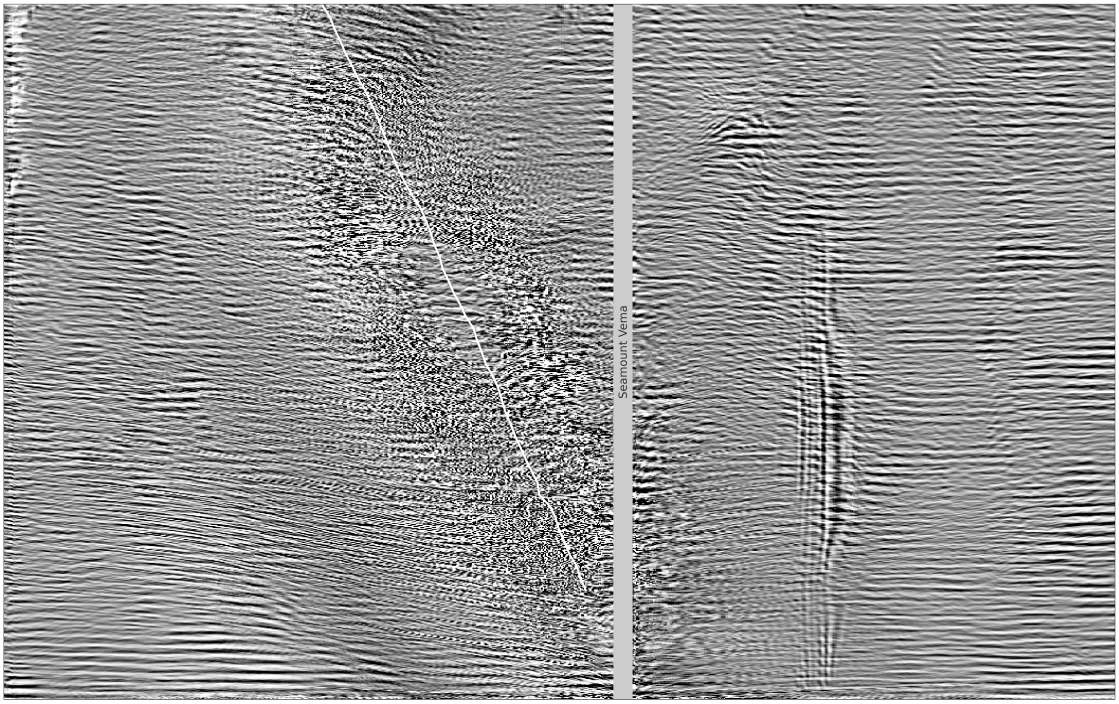

Moritz Epke

Hamburg 2025

Berichte zur Erdsystemforschung
Reports on Earth System Science

290
2025

Hinweis

Die Berichte zur Erdsystemforschung werden vom Max-Planck-Institut für Meteorologie in Hamburg in unregelmäßiger Abfolge herausgegeben.

Sie enthalten wissenschaftliche und technische Beiträge, inklusive Dissertationen.

Die Beiträge geben nicht notwendigerweise die Auffassung des Instituts wieder.

Die "Berichte zur Erdsystemforschung" führen die vorherigen Reihen "Reports" und "Examensarbeiten" weiter.

Anschrift / Address

Max-Planck-Institut für Meteorologie
Bundesstrasse 53
20146 Hamburg
Deutschland

Tel./Phone: +49 (0)40 4 11 73 - 0
Fax: +49 (0)40 4 11 73 - 298

name.surname@mpimet.mpg.de
www.mpimet.mpg.de

Notice

The Reports on Earth System Science are published by the Max Planck Institute for Meteorology in Hamburg. They appear in irregular intervals.

They contain scientific and technical contributions, including PhD theses.

The Reports do not necessarily reflect the opinion of the Institute.

The "Reports on Earth System Science" continue the former "Reports" and "Examensarbeiten" of the Max Planck Institute.

Layout

Bettina Diallo and Norbert P. Noreiks
Communication

Copyright

Photos on the back from left to right:
Christian Klepp, Jochem Marotzke,
Christian Klepp, Clotilde Dubois,
Christian Klepp, Katsumasa Tanaka

Kilometer-Scale Ocean Turbulence and Waves in the North and South Atlantic

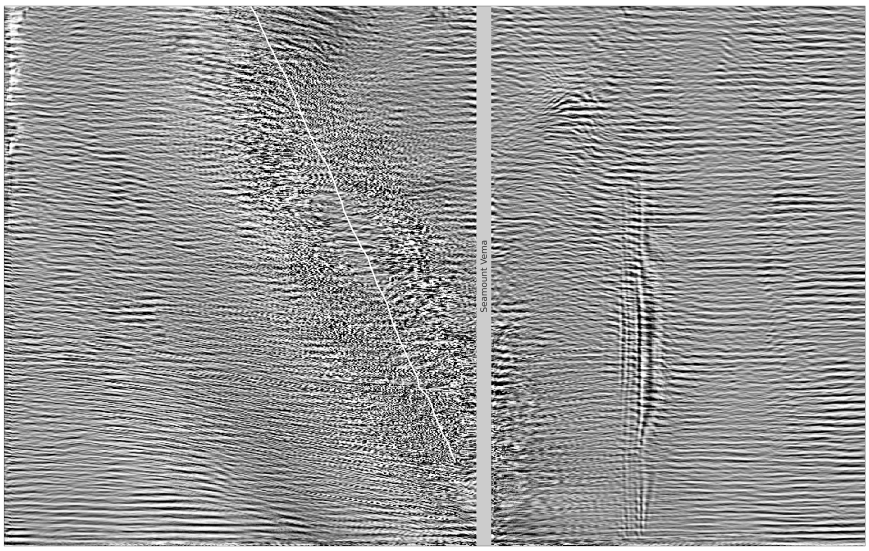

Moritz Epke

Hamburg 2025

Moritz Epke
aus München, Deutschland

Universität Hamburg
Fachbereich Erdsystemwissenschaften
Institut für Meereskunde

Max-Planck-Institut für Meteorologie
Bundesstrasse 53
20146 Hamburg

Tag der Disputation: 16. Mai 2025

Folgende Gutachter empfehlen die Annahme der Dissertation:
Dr. Nils Brüggemann
Prof. Dr. Carsten Eden

Vorsitzender des Promotionsausschusses:
Prof. Dr. Hermann Held

Dekan der MIN-Fakultät:
Prof. Dr.-Ing. Norbert Ritter

Titelgrafik vom Autor:
Eddies and Waves in Motion: This Hovmöller plot of vertical velocity shows an Agulhas Ring interacting strongly with seafloor topography as it crosses the Cape Basin, triggering waves and turbulence. The x-axis represents a zonal transect at Mount Vema, and the y-axis shows time, capturing the evolution of these dynamic ocean features.

Berichte zur Erdsystemforschung / Max-Planck-Institut für Meteorologie 290
Reports on Earth System Science / Max Planck Institute for Meteorology 2025

ISSN 1614-1199 - DOI: 10.17617/2.3658361

ABSTRACT

Despite their fundamental role in ocean dynamics, mixed layer instabilities and internal waves are often underrepresented or entirely absent in numerical ocean models. Their transient nature and small spatial scales make them difficult to observe and simulate, limiting our ability to study them outside of theoretical and idealized frameworks. This lack of comprehensive investigation leaves crucial aspects of their impact on ocean circulation and climate unresolved.

The emergence of advanced numerical models and high-resolution satellite observations is opening new frontiers in ocean science. With kilometer-scale models and refined remote sensing, we can now study submesoscale and wave processes in unprecedented detail. This thesis employs the ICON-SMT model, utilizing telescoping grid refinement to resolve these dynamics at sub-kilometer scales in the Atlantic Ocean.

In the first study, we demonstrated that our model configuration effectively captures mixed layer submesoscale eddies and their role in frontal overturning, restratification, and buoyancy flux. Through an analysis of 45 ocean fronts, we quantified these effects, confirming consistency with theoretical predictions and idealized models. Furthermore, we evaluated the accuracy of two mixed layer eddy parameterizations in replicating the influence of resolved submesoscale eddies.

The second study investigates how tides and submesoscale currents shape the ocean's frequency energy spectrum. Using a series of experiments with varying resolutions, one resolving submesoscale dynamics and another suppressing them in a coarser model, both with and without tidal forcing, we demonstrate that submesoscale dynamics are essential for accurately producing a -2 spectral slope in kinetic energy spectra, that closely matches moored observations. We further show, that tidal forcing significantly improves energy levels at the high frequency end of the sea surface height spectra. Here, the model accurately captures tidal peaks, though the overall energy levels still show some discrepancies compared to observations, which might indicates missing wave-wave interaction. Comparisons with in situ observations suggest that while high-resolution simulations drastically improve the representation of internal wave turbulence, even finer resolutions are needed to fully capture its magnitude.

Finally, we examine how mesoscale Agulhas Rings influence high-frequency ocean dynamics, particularly through interactions with bathymetric features like the Walvis Ridge and Vema Seamount. Eddy-tracking and spectral analysis reveal that energy levels within eddies are substantially higher than in the surrounding ocean, with pronounced increases during topographic encounters. We identify the generation of topographically-induced Karman vortex streets and lee waves, particularly as an Agulhas Ring encounters the Vema Seamount, and further confirm similar wave formation when these rings cross the Walvis Ridge.

Together, these studies provide novel insights into submesoscale turbulence, internal waves, and mesoscale-topography interactions in the Atlantic Ocean, high-

lighting the importance of high-resolution modeling in capturing these complex processes.

ZUSAMMENFASSUNG

Ungeachtet ihrer grundlegenden Rolle in der Ozeandynamik sind Instabilitäten in der Deckschicht und interne Wellen in numerischen Ozeanmodellen oft unterrepräsentiert oder fehlen ganz. Aufgrund ihres transienten Charakters und der kleinen räumlichen Skalen sind sie schwer zu beobachten und zu simulieren, was unsere Möglichkeiten einschränkt, sie außerhalb theoretischer und idealisierter Rahmenbedingungen zu untersuchen. Dieser Mangel an umfassenden Untersuchungen lässt entscheidende Aspekte ihrer Auswirkungen auf die Ozeanzirkulation und das Klima ungelöst.

Das Aufkommen fortschrittlicher numerischer Modelle und hochauflösender Satellitenbeobachtungen eröffnet der Meeresforschung neue Möglichkeiten. Mit Modellen im Kilometermaßstab und verfeinerter Fernerkundung können wir jetzt submesoskalige und Wellenprozesse in noch nie dagewesener Detailfülle untersuchen. In dieser Arbeit wird das ICON-SMT Modell verwendet, das eine Verfeinerung des Teleskopgitters nutzt, um diese Dynamik im Atlantischen Ozean im Subkilometerbereich aufzulösen.

In der ersten Studie haben wir gezeigt, dass unsere Modellkonfiguration submesoskalige Wirbel der Deckschicht und ihre Rolle beim umwälzen von Ozeanfronten, der Neuschichtung und der Auftriebsflüsse effektiv erfasst. Durch eine Analyse von 45 Ozeanfronten konnten wir diese Effekte quantifizieren und die Übereinstimmung mit theoretischen Vorhersagen und idealisierten Modellen bestätigen. Darüber hinaus haben wir die Genauigkeit von zwei Parameterisierungen für die Deckschicht bei der Nachbildung des Einflusses von aufgelösten submesoskaligen Wirbeln bewertet.

In der zweiten Studie wird untersucht, wie Gezeiten und submesoskalige Strömungen das Frequenz-Energiespektrum des Ozeans formen. Anhand einer Reihe von Experimenten mit unterschiedlichen Auflösungen, von denen eines die submesoskalige Dynamik auflöst und ein anderes sie in einem gröberen Modell unterdrückt, sowohl mit als auch ohne Gezeitenantrieb, zeigen wir, dass die submesoskalige Dynamik für die genaue Erzeugung einer -2-Spektralneigung in kinetischen Energiespektren, die eng mit verankerten Beobachtungen übereinstimmt, wesentlich ist. Darüber hinaus zeigen wir, dass der Gezeitenantrieb die Energieniveaus am hochfrequenten Ende des Meeresoberflächenhöhenspektrums deutlich verbessert. Hier erfasst das Modell genau die Gezeitenpeaks, obwohl die Gesamtenergieniveaus immer noch einige Diskrepanzen im Vergleich zu den Beobachtungen aufweisen, was auf fehlende Welle-Welle-Wechselwirkung hinweisen könnte. Vergleiche mit In-situ-Beobachtungen deuten darauf hin, dass hochauflösende Simulationen zwar die Darstellung interner Wellenturbulenzen drastisch verbessern, aber noch feinere Auflösungen erforderlich sind, um deren Ausmaß vollständig zu erfassen.

Zuletzt untersuchen wir, wie mesoskalige Agulhas-Ringe die Hochfrequenzdynamik des Ozeans beeinflussen, insbesondere durch Wechselwirkungen mit bathymetrischen Strukturen wie dem Walvis-Rücken und dem Vema Unterseeberg.

Eddy-Tracking und Spektralanalysen zeigen, dass die Energieniveaus innerhalb der Wirbel wesentlich höher sind als im umliegenden Ozean, mit einem deutlichen Anstieg während topographischer Begegnungen. Wir stellen fest, dass topographisch bedingte Karman-Wirbelstraßen und Leewellen entstehen, insbesondere wenn ein Agulhas-Ring auf den Vema Unterseeberg trifft, und bestätigen außerdem eine ähnliche Wellenbildung, wenn diese Ringe den Walvis-Rücken überqueren.

Zusammengenommen bieten diese Studien neue Einblicke in submesoskalige Turbulenzen, interne Wellen und Wechselwirkungen zwischen Mesoskala und Topographie im Atlantischen Ozean und verdeutlichen, wie wichtig hochauflösende Modellierung für die Erfassung dieser komplexen Prozesse ist.

PUBLICATIONS RELATED TO THIS DISSERTATION

Epke M., Brüggemann N., (2025a): "Overturning of Mixed Layer Eddies in a submesoscale resolving simulation of the North Atlantic", In: *review at Journal of Physical Oceanography*

Epke M., Brüggemann N., (2025b): "Impact of tides and eddies on ocean energy spectra in a submesoscale resolving simulations of the South Atlantic", currently in preparation for submission.

Epke M., Brüggemann N., (2025c): "High-Frequency Variability Generated by Mesoscale Eddies Interacting with Bathymetry in a Submesoscale-Resolving Simulation of the South Atlantic", currently in preparation for submission.

ACKNOWLEDGEMENTS

Er stand am Steuer seines Schiffes, und trotzte dem Ungestüm der Wellen...
Armer Mann!
Sein Schiff war ohne Anker und sein Herz ohne Hoffnung...
Ich sah, wie der Mast brach, wie die Winde das Tauwerk zerissen...
Ich sah, wie er die Hand nach mir ausstreckte...

— Heinrich Heine über Ludwig Börne, 1840

Having experienced and achieved so many things in these last years I don't want to leave doubt, that this would not have been possible without the people who enabled me to do so. However, considering politics this century I also want to highlight how invaluable the liberty to do independent research is.

First I would like to thank my supervisor Nils for giving me this opportunity, who guided me through the entire PhD and taught me how to do science. I thank him for the time and support during our frequent meetings, his optimism and patience, encouragement and positive attitude towards my ideas. Then I would like to express my appreciation to Evridiki Chrysagi, Carsten Eden and Jin-Song von Storch who helped me to keep the larger picture in mind as well to figure out where my research efforts could become most fruitful.

Of course such a study you cannot do isolated on an island. Where is the fun without the social interaction at work? I would like to thank my peers from MPI: in particular my office mates Quan, Maria, Lara and then of course all the others Arim, Veit, Mira, David, Angel, Josie, Fraser, Dominik, Lucas, Zoi, John, Arjun, Marius, Nina, Hans, Abisha just to name a few and of course from University: Pablo, Manita, Ankit, Jan, Silvano, Lars, Johannes, Che and Simon. And all that under the same roof!

But than there are others; I am grateful for the warm welcome in the institute by Dian, Xiuhua, Bo, Fatemeh, Jürgen and Helmut and the endless tea breaks and food discussions.

I had the chance to meet many of my colleagues outside of the office, travelling to a conference, exploring the food options next to conventions centers, or fading in blue nights after endless rows of posters. I would like to thank also researchers I got to know during these events amongst many; David, Pascal, Sarswita, James and Julian.

I am grateful for the financial support of the Collaborative Research Center TRR 181 Energy transfers in Atmosphere and Ocean, founded by the "Deutsche-Forschungsgesellschaft". And if anyone could embody this project I would think about Lea and Jennifer, the project coordinators, who helped me on so many issues.

I am deeply grateful for the opportunity to participate in the observational campaign (SONETT) in the South Atlantic. The ship cruise to the Walvis Ridge, was a highlight of my PhD, I did not only shortly felt like Dana Hilliot who shipped on the *Oedipus Tyrannus* to become a Fireman and to sail the world (Malcolm Lowry's

Ultramarine as part of *The Voyage that Never Ends*) or like one of Joseph Conrad's desperate heroes, who sailed either through the Atlantic Ocean coming from the Indian ocean after passing around the Cape of Good Hope (*The Narcissus*) or the other way around (*Youth*), which was friendly pointed out by my friend James before I embarked on this journey. Although this was not a steamer or charcoal carrier I would like to thank the people who enabled my participation on that cruise, in particular Christian Mertens. Again I want to thank my peers, without whom the weeks on the ship where hardly as exciting and enjoyable (Mariana, Victoria, Ilmar, Peter, Bulik and many more) and also the crew of the *Meteor*, which will soon be dismantled - an honor to sail on one of your last journeys.

Lastly I would like to thank my family and friends outside of academia, with whom I intensely discussed the different stages of my journey - the Dana Hilliot moments as well as those as Bernhard's *Der Untergeher*.

CONTENTS

1 INTRODUCTION

1.1 MOTIVATION

Vous êtes embarqué

— Le pari de Pascal, Blaise Pascal

In his reflections on human decision-making, Blaise Pascal used the metaphor "Vous êtes embarqué" ('You are embarked') to emphasise that we are already part of the journey, unable to avoid the responsibility of making choices in the face of uncertainty. This idea resonates deeply with the challenges for humans on a warming planet. As inhabitants of a planet undergoing rapid and unprecedented change, we are all on a shared journey into an uncertain future.

Climate science can be a useful tool on this journey, tasked with understanding and predicting the behavior of a warming planet. While advances in Earth system science have greatly improved our ability to predict weather, seasonal variations and aspects of climate, significant uncertainties remain - especially when it comes to long-term predictions. These uncertainties carry profound implications for risk assessment and decision-making, challenging humanity to act despite incomplete information. Much like Pascal's metaphorical voyage, there is no opting out of this process. The question is not whether we are part of this journey, but rather how we choose to steer the course.

From past observations and fundamental physical laws, we can develop predictive models to simulate potential future behaviors of the Earth system. These models allow us to explore a range of possible future climates rather than a single deterministic outcome. The use of the plural climates reflects the fact that future climate trajectories are shaped not only by physical processes but also by human behavior, including greenhouse gas emissions, land use changes, and policy decisions. By incorporating different socio-economic scenarios, climate models provide valuable insights into how our choices today influence the range of possible climate futures, and can therefore serve as a compass to navigate our way forward.

One critical part of the Earth's climate system is the ocean, acting as a vast reservoir of heat and carbon that drives atmospheric circulation and regulates global temperatures. Ocean dynamics describe the 'dynamical' share of physical processes in the ocean such as global circulation, currents, waves, eddies and mixing, driven by forces such as wind, tides, buoyancy and Earth's rotation - strongly influencing climate variability and the response of the earth to global warming. The wide range of temporal and spatial scales, from planetary motion to sub-centimeter turbulence, makes these dynamics extremely difficult, if not impossible, to fully simulate.

Global predictive ocean models are designed to simulate some of these dynamics, however they rely on a set of approximations and only partially resolve the full range of processes. The effects of unresolved or missing dynamics are often

neglected or, at best, represented through parameterizations, that rely on simplified physical relationships to approximate their influence. When critical processes are inadequately parameterized, or neglected entirely, these models can become energetically inconsistent, violating fundamental physical principles such as the conservation of energy, mass, and momentum. These inconsistencies can lead to biases in simulations of the current climate, and it is critical for simulating future climates, where nonphysical tuning choices can lead to unforeseen results.

Advances in computational power and our understanding how to translate physical equations into numerical algorithms allows nowadays to study processes on unprecedented resolution. These investigations will certainly improve our understanding of how such fast and small-scale dynamics interfere with larger dynamical processes of the climate system. This study therefore is concerned with investigating two of such fast and small-scale processes: (1) Submesoscale processes, which play a key role in cascading energy across scales and controlling the air-sea exchange of heat, energy and trace gases (Haine and Marshall, 1998; Gula et al., 2021). Within this research field, we focus specifically on mixed layer instabilities, with an emphasis on mixed layer baroclinic instabilities, potentially the most dominant instability mechanism in the upper ocean (Haine and Marshall, 1998). (2) Internal gravity waves, which are essential for redistributing energy throughout the ocean and sustaining the large-scale overturning circulation (Munk, 1966; Wunsch and Ferrari, 2004; Talley et al., 2011). Both, submesoscale processes and internal gravity waves are capable of generating high-frequency motions on 'small' temporal and spatial scales. These motions are inherently challenging to observe and even more difficult to simulate accurately. Note that many other processes, such as wind-driven Ekman dynamics or other local forcing mechanisms, can also contribute to the generation of such high-frequency motions.

As mentioned above, recent advances in ocean modeling have enabled the partial resolution of these high-frequency motions within more realistic oceanic contexts. However, these models remain highly complex and are not yet fully understood, as their complexity increasingly mirrors that of the real ocean. In this study, we leverage such models to investigate these high-frequency motions and assess the extent to which the models align with theoretical predictions, idealized simulations, and observations. Ultimately, we aim to contribute to a deeper physical understanding of these processes and to the development of improved ocean and climate models.

1.2 HIGH-FREQUENCY MOTIONS IN THE OCEAN

... und er fühlte sich wie eine durch beide Flügel geschossene Ente,
die ins Meer der Liebe hinabstürzte und versuchte durch schwimmen zu überleben.

— Der Mann ohne Eigenschaften, Robert Musil

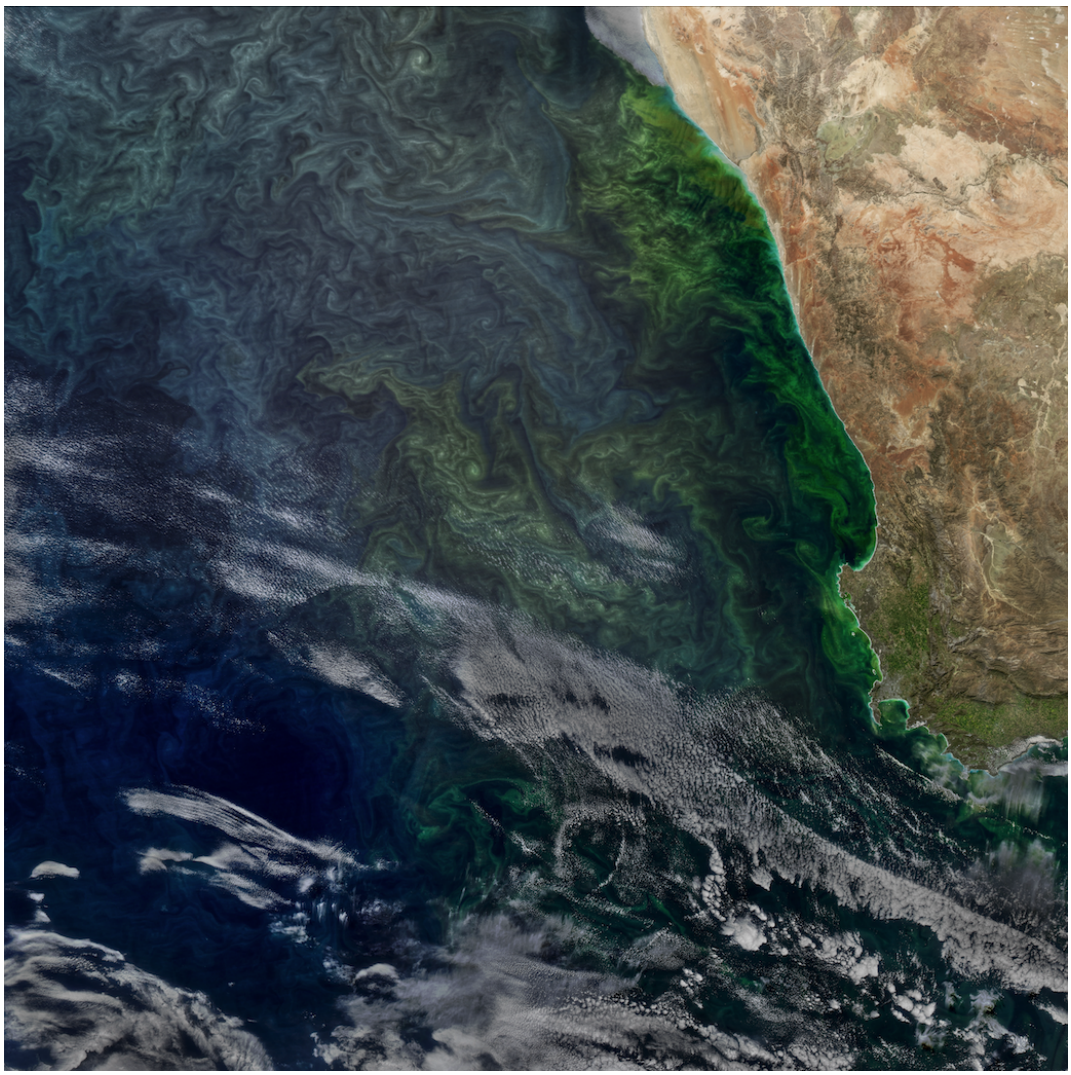

Figure 1: The chlorophyll-a concentration in the South Atlantic, close to the Benguela upwelling region. The phytoplancton blooms trace the eddies and plumes. Note that, this satellite image is postprocessed to enhance the visibility. Credits: NASA Earth Observatory images by Jesse Allen, using data from the Level 1 and Atmospheres Active Distribution System (LAADS), and ocean imagery by Norman Kuring, NASA's Ocean Color web.

A satellite image of the South East Atlantic Ocean, near the Benguela upwelling system, reveals a captivating snapshot of ocean dynamics, see Fig. 1. Beneath thin layers of cloud, vibrant swirls of phytoplankton blooms trace the boundaries of ocean fronts. These blooms are identified by satellite sensors, which measure variations in reflected light wavelengths altered by the presence of chlorophyll-a. This

pigment, abundant in phytoplankton, absorbs blue and red light while reflecting green, imparting a distinct greenish hue to waters with high phytoplankton concentrations.

Phytoplankton blooms depend on the availability of light and nutrients, both regulated by physical oceanic processes, such as upwelling (see Benguela upwelling close to the shore in Fig. 1) or due to submesoscale dynamics (see curls and swirls far away from the coastline in Fig. 1). These processes involve intense vertical motions that transport nutrients into the euphotic zone, where sunlight penetrates and supports photosynthesis (Mahadevan, 2016). Operating on short periods, typically ranging from hours to days, submesoscale processes play a critical role in driving the rapid development and dissipation of blooms (Mahadevan, 2016). As such, mapping chlorophyll-a concentrations offers a powerful method to visualize these submesoscale processes, uncovering features, such as plumes and swirls.

1.2.1 *Submesoscale Dynamics*

Submesoscale dynamics, unlike the synoptic or mesoscale regimes, do not represent a distinct dynamical category but instead bridge the gap between larger-scale geostrophic motions and smaller-scale ageostrophic turbulence. These dynamics are related to a host of mixed layer instabilities, which operate on temporal scales of hours to a few days and spatial scales ranging from a few hundred meters to several tens of kilometers (Haine and Marshall, 1998; Capet et al., 2008a; Brüggemann and Eden, 2014; McWilliams, 2016; Mahadevan, 2016). These motions can be either in large-scale balance (geostrophic) or out of balance (ageostrophic) and are therefore associated with a Rossby and Richardson number of $\mathcal{O}(1)$. Submesoscale dynamics are often defined as processes occurring at scales smaller than the first baroclinic Rossby radius of deformation (Mahadevan, 2016).

Figure 2 illustrates the local Rossby number over a region in the South Atlantic, derived from simulations with horizontal resolutions of roughly 600 m on the one hand and with 5 km and on the other. High Rossby numbers, indicative of strongly ageostrophic motions, are found near intense mesoscale features such as eddies and ocean fronts.

Submesoscale motions are particularly active in the ocean's surface mixed layer, where sharp gradients in temperature, salinity, and density (fronts) often develop. The physical key drivers for submesoscale dynamics and in particular mixed layer eddies are explored in the following section.

1.2.2 *Baroclinic and Symmetric Instability*

Ocean fronts are regions characterized by strong horizontal density gradients, typically found at the boundaries between different water masses, such as the Gulf Stream or subpolar fronts. The available potential energy in these regions is linked to the tilt of isopycnals (surfaces of constant density). Baroclinic instability occurs when isopycnals and surfaces of constant pressure (isobars) are misaligned, creating a baroclinic state. Under these conditions, small perturbations can amplify, converting potential energy into kinetic energy and reducing the steepness of the isopycnals. This process is a primary driver of mesoscale eddies, which dominate

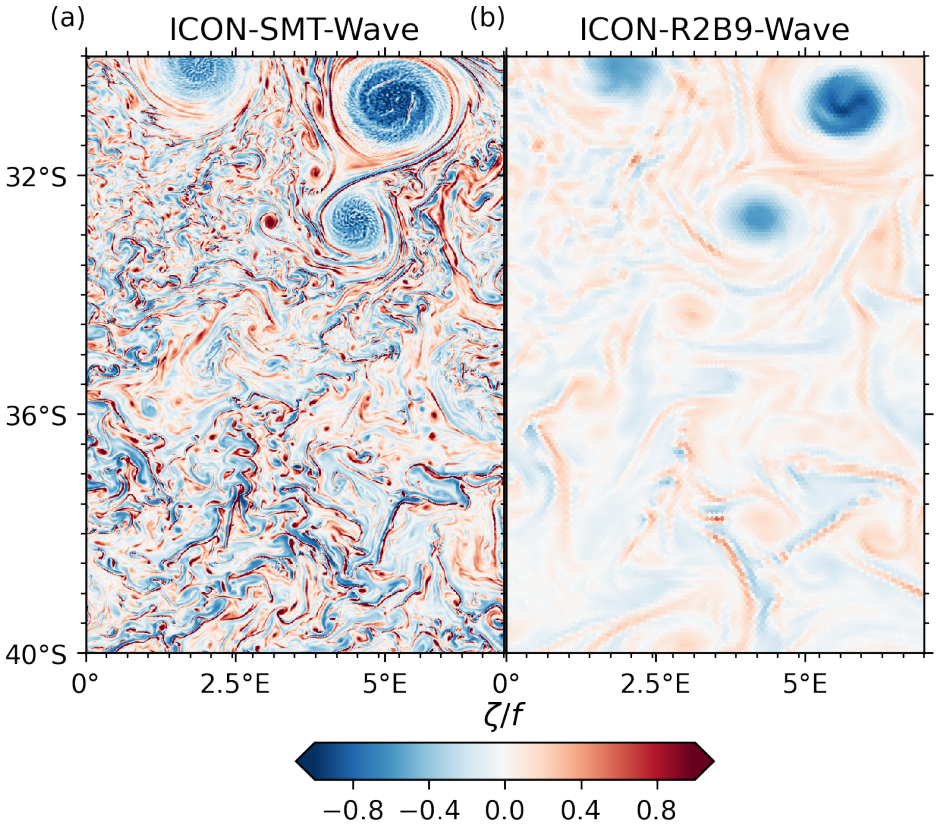

Figure 2: Snapshot of the vorticity of a submesoscale resolving simulation ICON-SMT with roughly 600 m horizontal resolution (a) and an eddy permitting model ICON-R2B9 with 5 km horizontal resolution (b). The snapshot is taken four months after the initialization (for details see also Chap. 2).

the ocean's kinetic energy budget (Olbers et al., 2012) and play a key role in the ocean energy cycle.

However, once generated, this kinetic energy does not remain confined to the mesoscale but undergoes further redistribution through nonlinear interactions. A significant portion of the kinetic energy cascades upscale (inverse cascade) to larger structures and the mean current, where it must ultimately be dissipated. However, the exact mechanisms responsible for this dissipation remain unclear, while possible candidates are Lee wave generation and spontaneous emission of gravity waves.

Under favorable conditions for ageostrophic turbulence, a downscale energy flux (downward cascade) can also be observed (Scott and Arbic, 2007). These motions eventually lead to dissipation and mixing, contributing to the vertical and lateral redistribution of heat, momentum, and tracers.

A well-known theoretical framework for baroclinic instability is the Eady problem (Eady, 1949). In his analysis, Eady linearized the equations of motion for a rotating flow in geostrophic thermal wind balance, assuming a density field with constant vertical and meridional gradients, bounded by rigid surfaces at the top and bottom. Eady demonstrated that small perturbations in this system grow into waves, with the growth rate depending on the wavelength. Initially,

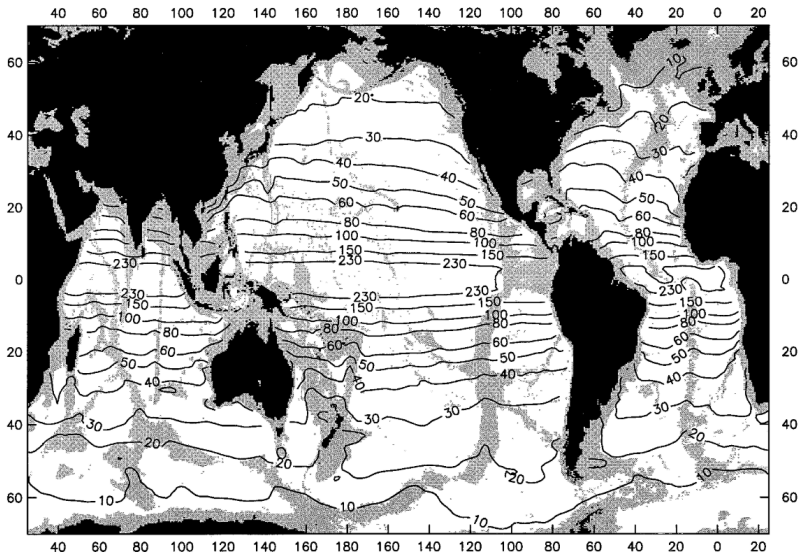

Figure 3: The first baroclinic Rossby radius of deformation calculated for the entire water column. The Rossby radius of deformation is calculated $L_{R_b} = \frac{\overline{N}_b H_b}{\pi f}$ with the bathymetry averaged Brunt-Väisälä frequency $\overline{N}_b = \int_b^t N(z)dz/H_b$, the bathymetry H_b and the local Coriolis frequency f. Taken from Chelton et al. (1998).

multiple modes grow exponentially, but over time, only the fastest-growing mode dominates. The most unstable mode or wave-like perturbation corresponds to a wavelength of $\lambda = 1.6/L_R$ with the first baroclinic Rossby radius of deformation, $L_R = NH/f$, the Brunt Väisäla Frequency N and the Coriolis parameter f (see also Fig. 3). The Rossby radius of deformation is typically $10 - 50\,\mathrm{km}$ in the mid-latitudes (see Fig. 3). The maximum growth rate is given by $\gamma \approx 0.3M^2/N$ with $M^2 = g|\partial\bar{\rho}/\partial y|/\rho_0$. It turns out, that the largest growth rates are typically observed in regions with intense mesoscale kinetic energy, such as western boundary currents (Olbers et al., 2012).

Stone expanded the Eady model for ageostrophic and for non-hydrostatic conditions (Stone, 1966; Stone, 1970; Stone, 1972). His solutions reveal that the fastest-growing modes depend on the background conditions, specifically characterized by the Richardson number (see Fig. 4). Stone identified three distinct instability modes, each dependent on the background state characterized by the Richardson number: (1) Kelvin-Helmholtz instability dominates when $Ri < 1/4$, as it has the fastest exponentially growing mode; (2) symmetric instability is dominant for $1/4 < Ri < 0.95$ and (3) baroclinic instability takes over when $Ri > 0.95$, exhibiting the fastest growth rate in this range.[1]

Baroclinic instability in the mixed layer is another mode of instabilities that arise when the density profile is not vertically constant but has two (or more) layers, one with small stratification and one with higher stratification. In this case, there are two unstable modes, one that produces unstable profiles only in the weakly stratified layer, that grows faster and at shorter wave lengths, and one that extends

1 Note that a later study showed that symmetric instability has the largest growth rate for $Ri < 0.95$ and that Kelvin-Helmholtz instabilities do not occur in the Eady problem, see (Vanneste, 1993).

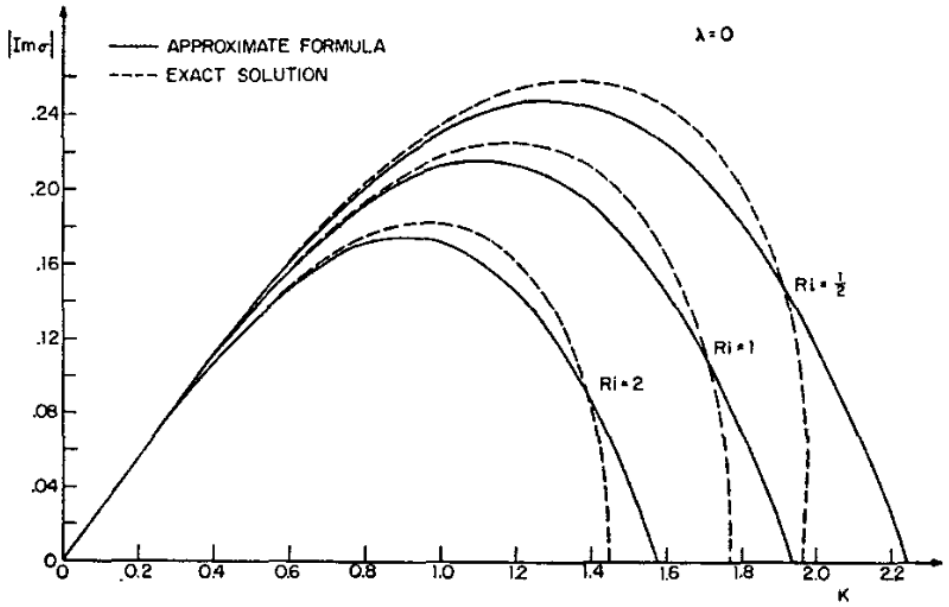

Figure 4: The growth rate over the zonal wavenumber k and the complex frequency σ for exact and approximate solutions, taken from Stone (1970). The strongest growths rates are associated with geostrophic baroclinic instability for $\mathrm{Ri} > 0.95$, symmetric instability $1/4 < \mathrm{Ri} > 0.95$ and with Kelvin-Helmholtz instability $1/4 < \mathrm{Ri}$.

over the entire water column with smaller growth rates at larger wave lengths (Sören et al., 2014). The first produces submesoscale mixed layer eddies (MLEs), the second mesoscale eddies.

A typical life cycle of mixed layer instabilities works as follows (Haine and Marshall, 1998; Fox-Kemper et al., 2008; Callies and Ferrari, 2018b; Verma et al., 2019; McWilliams, 2016; Gula et al., 2021): Wind forcing or buoyancy loss can create conditions that favor Kelvin-Helmholtz instabilities ($\mathrm{Ri} < 1/4$), leading to a well-mixed background with low potential vorticity. Once this mixing occurs, lateral density gradients can trigger symmetric instabilities ($1/4 < \mathrm{Ri} < 0.95$), which quickly re-stratify the density fronts. This re-stratification continues until symmetric instabilities are suppressed, allowing baroclinic instabilities $0.95 < \mathrm{Ri}$ to take over and further re-stratify the density fronts.

1.2.3 *Parameterizing the effect of unresolved eddies*

In ocean modeling, many instabilities and the resulting turbulent motions are not well resolved, leading to significant biases. If baroclinic instability is inappropriately resolved, there is no or too little transformation of available potential energy (inherent to any tilted isopycnal) to eddy kinetic energy. As a consequence, the isopycnals remain too steep and the flow lacks eddy kinetic energy in such a simulation. Parameterizations improve the realism of large-scale ocean circulation and enable long-term climate simulations at reasonable computational cost.

The Gent-McWilliams (GM) parameterization (Gent and Mcwilliams, 1990) is designed to represent the effects of unresolved mesoscale eddies in ocean models. It introduces an eddy-induced overturning velocity to flatten isopycnals, mimicking

the re-stratification caused by mesoscale eddies and thus improves the realism of large-scale ocean simulations without explicitly resolving eddies.

In the surface mixed layer, MLE parameterizations are used to capture the effects of unresolved submesoscale eddies. These smaller eddies also act to re-stratify the mixed layer by flattening tilted isopycnals. MLE parameterizations typically introduce an eddy-induced overturning streamfunction to simulate both lateral and vertical tracer transport, thereby improving the representation of mixed layer dynamics in coarse-resolution models (Stone, 1966; Green, 1970; Fox-Kemper et al., 2008). This type of parameterization is discussed in more detail in Chap. 2. While both parameterizations follow the same principle of introducing eddy fluxes to flatten isopycnals, the main difference is that GM targets mesoscale processes under well stratified ocean conditions, and MLE parameterizations focus on submesoscale processes under weak stratification in the surface mixed layer.

For ensemble studies and long-term climate simulations, the GM parameterization remains highly relevant, especially for coarse-resolution or eddy-permitting models. However, in state-of-the-art eddy-resolving models with horizontal resolutions of $1/10^\circ$ ($\approx 10\,\mathrm{km}$) or finer, the GM parameterization becomes redundant since mesoscale eddies can be resolved dynamically. Despite advances in high-resolution modeling, global submesoscale-resolving simulations remain sparse due to their computational cost, storage requirements, and technical constraints. Such simulations are currently limited to short timescales and are not yet practical for long-term climate studies. Therefore, parameterizations such as GM and MLE will remain essential to simulate unresolved processes in global climate models, at least until km-scale simulations become feasible on climate time scales of several decades.

1.2.4 *Internal Waves*

Internal waves are a ubiquitous feature of the ocean, yet they are challenging to observe in their classic form due to the complexity of overlapping dynamic processes. Susanto et al. (2005) captured an echogram of an internal wave in the Lombok Strait, Indonesia, which was remarkable not only for its clarity but also for the wave's extreme characteristics, see Fig. 5. The wave passed beneath the ship at a speed of $1.5\,\mathrm{m\,s^{-1}}$ with an amplitude of 100 m, making it an extraordinary example of internal wave dynamics. Such observations are rare, as the signals of internal waves are often masked by other dynamic processes. This observation highlights the significant imprint of internal waves on high-frequency oceanic motion.

Internal waves occur in stratified fluids under the influence of gravity and rotation. These waves arise when water parcels are displaced, creating buoyancy forces that attempt to restore equilibrium in the stratified water column. In contrast to air-surface gravity waves, the stratification is weak and the periods range from approximately 20 min in the well-stratified upper ocean, to a few hours in the weakly stratified deep ocean (Talley et al., 2011). The maximum frequency is limited by the stratification N, while the lowest frequency of internal waves is limited by the inertial frequency, thus $f < \omega < N$. The range of spatial and temporal scales of internal waves, determined by their dispersion relation, can be seen in Fig. 6.

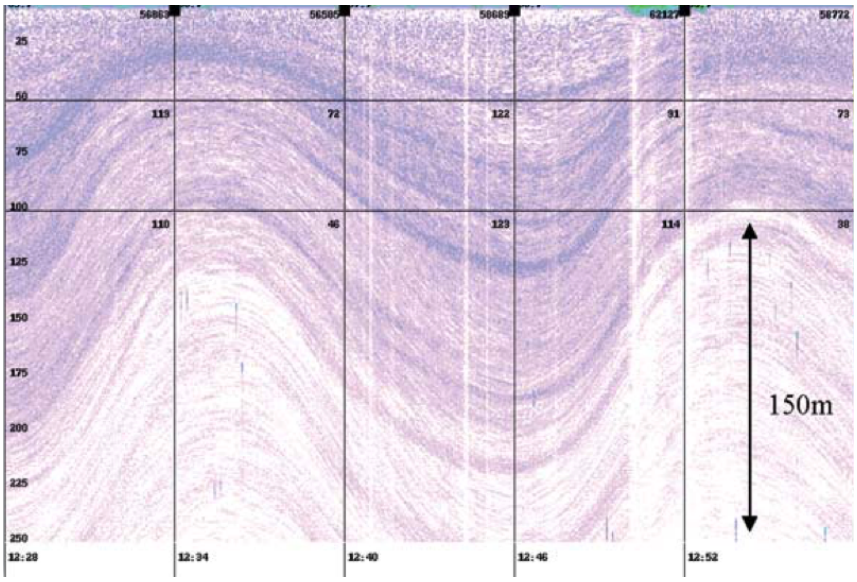

Figure 5: Echogram of the water column obtained by an EK500 Echosounder operating at frequency of 38 kHz during the 2005 INSTANT Indonesian throughflow cruise. The echogram clearly shows the internal waves in the Lombok Strait. The ship was on standby when waves with a wavelength of 1.8 km passed under the ship with a speed of $1.5\,\mathrm{m\,s^{-1}}$. The wave amplitude (peak to trough) exceeds 100 m. Higher backscatter values indicate higher plankton concentration or large schools of fish. Vertical axis is depth in meters. Taken from (Susanto et al., 2005)

Along internal waves the scale of other important oceanic processes are shown alongside the range of scales covered by typical simulations. This comparison indicates the limitations of current global climate simulations, which remain constrained by existing computational and storage resources. Additionally, the range of scales necessary to resolve submesoscale dynamics (as discussed in Sec. 1.2) and the range of scales covered by submesoscale resolving models are highlighted in Fig. 6. While eddy-resolving simulations capture only a small fraction of the spatial scales of internal waves, newer submesoscale resolving models are capable of resolving a significantly broader range of these waves. However, those models cannot be run over long periods, necessary to investigate climate time scales. It is evident that internal waves and submesoscale motions overlap extensively in both spatial and temporal scales, see Fig. 6.

1.2.5 *Internal Tides and Lee Waves*

A dominant source for internal waves originates from tidal forces, which are the gravitational interactions between the Earth, Moon, and Sun. The resulting tidal forces cause periodic displacements in the entire water column, generating barotropic tides that propagate horizontally over large scales, often exceeding thousands of kilometers (Bell, 1975; Nikurashin and Ferrari, 2013; Olbers et al., 2012). The interaction of barotropic tides with bathymetry can cause baroclinic tides with wavelength typically ranging from 10 to 100 km and periods matching tidal frequencies such as semi-diurnal and diurnal. They are internal gravity waves forced at tidal frequencies, thus covering a specific frequency range of the internal wave

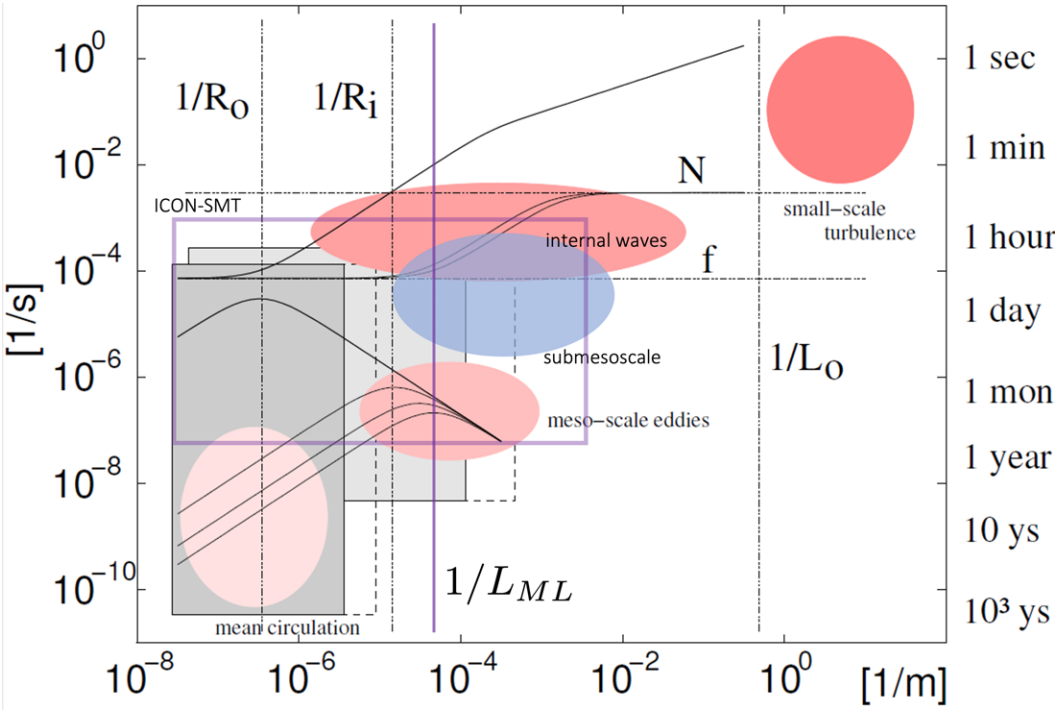

Figure 6: Space-time scales of important oceanic processes (pink areas) and scales explicitly resolved by ocean models (grey rectangles). Also shown are the dispersion curves (solid lines) of Rossby waves (lower left), internal waves (between N and f) and the surface gravity waves (upper center). The spatial and temporal constraints of ICON-SMT are included indicating the regime or dynamics, which the model theoretically permits (purple box). Dotted lines indicate the first external R_o and the first internal R_i Rossby radii and the Ozmidov length scale L_σ. Additionally, the maximum growth rate of mixed layer instability is included, (here $L_{ML} \approx$ 40 km, see Fig. 9 in Chap. 2) for the computation of the estimate. Figure adapted from Olbers et al. (2012).

spectrum. Baroclinic tides dominate the internal wave field at generation sites, particularly near steep bathymetric features like continental slopes, ridges, and seamounts (Legg and Adcroft, 2003; Garett and Kunze, 2007). They can interact with the ocean's mesoscale flows (Kunze, 1985), leading to energy transfer across different scales and processes.

While internal tides are generated by tidal flow over topography, lee waves arise from the interaction of steady currents with bathymetry. Lee waves typically have shorter wavelengths than internal tides (Garett and Kunze, 2007; Nikurashin and Ferrari, 2013). With their characteristics depending on current strength, obstacle size, stratification, and frequency, lee waves can be either steady or transient but eventually break, leading to enhanced mixing (Musgrave et al., 2022). Global estimates emphasise their significant role in turbulence generation and energy dissipation (Nikurashin and Ferrari, 2013; Musgrave et al., 2022).

1.2.6 *Separation of eddies and waves*

Identifying internal waves in complex oceanic flow fields has long been a challenge due to the overlapping spatial and temporal scales of waves and eddies (Olbers et al., 2012; Bühler, 2014; McWilliams, 2016; Shakespeare et al., 2021). A key difficulty lies in the nonlinear interactions that govern these systems (Ferrari and Wunsch, 2009), including wave-wave (Hasselmann, 1966; Eden et al., 2019b), wave-mean flow (Bartello, 1995), wave-eddy (Sebastia Saez et al., 2024) and tide-eddy (Dunphy and Lamb, 2014) interactions. These nonlinear processes transfer energy, momentum, and other properties across scales, complicating the separation of internal waves from the surrounding flow and their contributions to the oceanic energy cascade (Bühler and McIntyre, 2005).

Nonlinear wave interactions occur when different components of the wave field interact in ways that deviate from simple superposition principles, redistributing energy across scales (Shakespeare et al., 2021). Near-inertial waves, for example, are strongly influenced by the vorticity of mesoscale (Kunze, 1985; Klein et al., 2004) and submesoscale (Brunner-Suzuki et al., 2014) dynamics, which can modify their propagation and energy transfer. These nonlinear eddy-wave interactions, but also wave-wave interactions enable energy to cascade across scales, either from large to small scales (forward cascade) or from small to large scales (inverse cascade), significantly influencing the dynamics of ocean currents and waves (Brunner-Suzuki et al., 2014; Riley and Lelong, 2000). These interactions play a critical role in ocean mixing and energy dissipation.

Various methods have been developed to distinguish internal waves from other flow components. These include Eulerian temporal and spatial filters, Lagrangian filtering techniques (Shakespeare et al., 2021), and decompositions into balanced and unbalanced flows, as described by (Chouksey et al., 2018; Eden et al., 2019a; Masur and Oliver, 2020; Chouksey et al., 2023). However, many of these approaches depend on regular grid systems, limiting their applicability to unstructured grid models increasingly used in modern ocean modeling. An alternative is the Helmholtz wave-vortex decomposition, which separates the flow into rotational and irrotational components (e.g. Bühler et al., 2017; Vanneste and Young, 2022). However, this method presents challenges, such as the choice of boundary conditions and the assumption of linear superposition of the rotational and irrotational components, which can be problematic given the nonlinear interactions common in the ocean (see above).

1.3 RESEARCH OBJECTIVES AND APPROACH

Mixed layer instabilities and internal waves are crucial for energetically consistent ocean models, yet they are often poorly represented or entirely missing. Their small scales and rapid evolution make them extremely challenging to observe and simulate. As a result, these processes remain largely unexplored, with most research limited to theoretical and idealized simulations, leaving a significant gap in our understanding.

Significant advances have been made in both fields. Improved computational power and better numerical methods now allow for the study of ocean processes

at unprecedented resolution. Similarly, recent satellite missions have revolutionized remote sensing, providing higher-resolution observations. With the advent of kilometer-scale ocean models and advanced satellite technology our ability is rapidly enhancing to observe and simulate submesoscale dynamics.

We aim to leverage these advancements to improve our understanding of mixed layer eddies and their representation in global circulation models. Additionally, a comprehensive evaluation of how well parameterizations capture these processes in realistic ocean environments remains a crucial yet largely unfulfilled objective. To address this gap, we pose the following research question:

How well do theoretical estimates and parameterizations capture the restratification of mixed layer fronts by submesoscale instabilities in a kilometer-scale ocean simulation with realistic forcing?

This study utilizes a novel model configuration, ICON-SubMesoscale-Telescope (ICON-SMT), which takes advantage of ICON's unstructured grid to enable continuous refinement toward a specific focus area, such as the North Atlantic. Figuratively, this can be visualized as a discretized sphere where grid cells are dynamically "pulled" or "pushed" to concentrate resolution in regions of interest. This adaptive approach allows for the simulation of global ocean processes while achieving unprecedented resolution in targeted areas (Korn et al., 2022; Hohenegger et al., 2023).

The first application of ICON-SMT focuses on the Gulf Stream separation region in the North Atlantic, a critical zone where large-scale western boundary currents interact with fresher waters from higher latitudes and the central gyre, driving water mass transformation and mixing. The obliquity of ocean fronts across multiple scales gives rise to instabilities that fuel intense mesoscale and submesoscale activity. In particular, the prevalence of mixed layer eddies in this region makes it an ideal testbed for addressing the research question.

Submesoscale instabilities and internal tides play a key role in driving ocean variability. However, disentangling these processes from other sources of high-frequency variability, such as wind forcing or Ekman fluxes, remains challenging. The extent to which these mechanisms contribute to high-frequency energy levels in the ocean is still unclear. We summarize this open question as follows:

What impact do mixed layer eddies and tides have on high-frequency ocean dynamics?

To address this research question, we apply a second ICON-SMT configuration focused on the region near the Walvis Ridge. This area is notable for its coherent anticyclones, known as Agulhas rings, as well as strong baroclinic tides generated by the interaction of the barotropic tide with the ridge. Using this high-resolution setup, we analyze high-frequency ocean variability at previously unresolved scales.

The focus region aligns closely with the study area of a two concurrent observational campaigns conducted as part of the collaborative project TRR181. The measurements obtained in this campaigns provide high-frequency in situ data using ADCPs and PIES over a two-year period, offering an invaluable dataset to evaluate and validate the new model configuration and to obtain independent information about the energy frequency spectrum.

To this end, we conduct dedicated sensitivity experiments to isolate different processes. For example, we run our configuration with and without tides, with submesoscale dynamics resolved in ICON-SMT, and with submesoscale dynamics suppressed in a coarse reference run. Each experiment is designed to give insight in which processes are setting up the energetics. In particular, we analyze which processes of baroclinic, barotropic instabilities, mesoscale, submesoscale or wave processes have a dominant contribution to high-frequency ocean energetics.

While the previous research question focuses on how the suppression or addition of general physical processes influences ocean variability, here we aim to explore the impact of more distinct processes. Mesoscale eddies have a dominant influence on ocean variability. As they propagate through basins, they interact strongly with topography, generating high-frequency motions across multiple scales and depth levels. Our goal is to shed light into the contributions of these distinct processes to ocean variability. We phrase our research question as:

What is the influence of mesoscale eddies and their interaction with bathymetry on high-frequency variability? Which role do topographically-generated internal waves play here?

We apply the same ICON-SMT configuration as described above, as the region is ideal for studying individual mesoscale eddies. Using an eddy tracking algorithm, we assess the effect of these eddies on the background ocean energetics, and investigate the role of eddy-bathymetry interactions, particularly in relation to topographically generated internal waves. Specifically, we focus on the generation of internal waves through interactions with topography, examining how these waves are generated, propagate, and influence broader ocean dynamics.

Through our analysis, we pioneer the investigation of high-frequency and small-scale dynamics in realistic high-resolution ocean model configurations, complemented by novel observational products. We also aim to contribute to the understanding of kilometer-scale models, which are growing in complexity and increasingly resemble the dynamics of the real ocean.

1.4 OVERVIEW

This thesis is structured into three main parts, each addressing a key research question presented in the Introduction. The second Chapter 'Overturning of Mixed Layer Eddies in a submesoscale resolving simulation of the North Atlantic' is a reprint of the manuscript which has been submitted to the Journal of Physical

Oceanography. Note that the novel model configuration is introduced here. The third Chapter 'Impact of tides and eddies on ocean energy spectra in a submesoscale resolving simulations of the South Atlantic' is manuscript in preparation for submission. This study exploits the synergies of our novel ICON configuration and the SONETT cruise. The fourth Chapter 'High-Frequency Variability Generated by Mesoscale Eddies Interacting with Bathymetry in a Submesoscale-Resolving Simulation of the South Atlantic' is an early-stage manuscript. Finally, Chapter 5 presents the conclusions of this thesis.

2

OVERTURNING OF MIXED LAYER EDDIES IN A SUBMESOSCALE RESOLVING SIMULATION OF THE NORTH ATLANTIC

This chapter is a reprint of the manuscript, that has been submitted as:

Epke, M., Brüggemann, N., (2025): "Overturning of Mixed Layer Eddies in a submesoscale resolving simulation of the North Atlantic", In: *review at Journal of Physical Oceanography*

ABSTRACT:

To study submesoscale instabilities in the ocean mixed layer, this study uses the novel ICON-SMT configuration that exploits a telescoping grid refinement to achieve a horizontal resolution finer than 1 km over wide areas of the North Atlantic. The model's ability to simulate mesoscale to submesoscale turbulence is validated by comparing spatial power spectra of sea surface temperature and height with satellite data and a 10 km eddy-resolving simulation. We find more realistic variability in the refined grid simulation compared to the coarser simulation over a wide range of scales, including the mesoscale eddy regime. Furthermore, the high-resolution permits submesoscale baroclinic instabilities at ocean fronts and we observe strong frontal overturning and re-stratification. Overturning rates are diagnosed from eddy buoyancy flux and mean front characteristics such as horizontal and vertical density gradients. To accurately capture the vertical extent of mixed-layer eddy instabilities, commonly used threshold algorithms for identifying the mixed-layer depth must be modified. We compare spatial and time filtering approaches for estimating submesoscale eddy fluxes and find qualitative similarity, although time filtering yields stronger fluxes. The diagnosed overturning rates are compared to two submesoscale baroclinic instability parameterizations. Both capture overturning magnitude at ocean fronts within an order of magnitude but overestimate it at eddy rims. Comparing submesoscale eddy fluxes in the entire study area shows two different regimes where the parameterizations slightly differ in the ability to capture the diagnosed eddy fluxes.

STATEMENT

In this study, we use the ICON model with a novel configuration that allows to have a flexible horizontal resolution. With that configuration, we achieve a horizontal resolution finer than 1 km over large parts of the North Atlantic. This allows us to study so-called submesoscale ocean eddies that occur on small spatial scales at upper-ocean density fronts. Based on a comparison with high-resolution satellite data, we can show that our configuration better captures the variability on

small scales compared with coarser configurations. Furthermore, we quantify how rapidly the sub-mesoscale eddies turn over the density fronts and we evaluate how well parameterizations would be able to capture such a submesoscale eddy overturning. These findings advance understanding of submesoscale dynamics, their role in ocean energy transfer and mixing.

2.1 INTRODUCTION

The upper-ocean boundary layer is a crucial player within the climate system since momentum, heat and trace gases need to pass this layer to be exchanged between the atmosphere and the deep ocean. This layer is the place of various turbulent processes interacting with each other and impacting the ocean-atmosphere exchange. Typically, the vertical density stratification is low in this also called upper-ocean mixed layer and often strong lateral density gradients occur due to the vibrant mesoscale eddy field or wind-driven currents. Along those fronts, submesoscale eddies can emerge that crucially impact the air-sea exchange by modifying the vertical stratification and by advecting e.g. heat or trace gases. The purpose of this study is to investigate such submesoscale eddies in a realistic ocean simulation and to assess how vigorously these submesoscale eddies re-stratify upper-ocean fronts. Therefore, we use novel configuration of the ocean model ICON-O that allows to refine the horizontal grid to achieve a sub-kilometer scale resolution over large parts of the North Atlantic that is required to study those submesoscale dynamics.

Turbulence in the upper-ocean is triggered by a large variety of instability processes. Often the life-cycle of such upper ocean turbulence works in the following way (see e.g. Haine and Marshall, 1998; Fox-Kemper et al., 2008; Callies and Ferrari, 2018a; Verma et al., 2019; Zheng and Jing, 2024): Wind forcing or buoyancy loss induces favorable conditions for Kelvin-Helmholtz instabilities that provide a well mixed background state with low potential vorticity. Afterwards, in the presence of lateral density gradients, symmetric instabilities can occur that rapidly re-stratify the density fronts up to a level of re-stratification where symmetric instabilities are suppressed and baroclinic instabilities finally re-stratify the density fronts.

Compared with symmetric instability, baroclinic instability usually persists much longer and therewith determines the mixed layer eddy fluxes over a substantial amount of time. The eddies that occur due to baroclinic instabilities in the upper-ocean mixed layer are often called submesoscale to indicate that they have spatial scales that are smaller than those of deeper mesoscale eddies (e.g. Thomas, 2005). If subject to down-front winds, the conditions for mixed layer baroclinic instability can be further extended Thomas (2005) since the down-front winds lead to a cross-front Ekman transport, which destabilizes the water column and leads to convection opposing the eddy overturning circulation. Thus, down-front winds act to maintain upper ocean fronts, while up-front winds have the opposite effect by inducing an Ekman transport that supports the mixed layer eddy overturning (Mahadevan et al., 2012; Mahadevan, 2016). However, even after the passage of a storm event, submesoscale re-stratification remains rather persistent and maintains reduced mixed layer depths (MLD) (Chrysagi et al., 2021).

The eddies associated with upper-ocean symmetric and baroclinic instabilities rapidly re-stratify the ocean by overturning the density fronts and thereby affect-

ing the vertical small-scale turbulent transport of e.g. heat, salt and other tracers (Haine and Marshall, 1998; Boccaletti et al., 2007; Capet et al., 2008a). Furthermore, the strong vertical velocities associated with submesoscale eddies transport tracers such as nutrients into the euphotic layer and thus orchestrate marine life cycles, e.g. phytoplankton blooms (Mahadevan, 2016). Recent observations from gliders and mooring arrays show enhanced vertical buoyancy fluxes at strong buoyancy gradients (Yu et al., 2019; Zhang et al., 2021; Zheng and Jing, 2024). In addition, submesoscale turbulence can provide energy transfer to smaller scales (Capet et al., 2008b; Molemaker et al., 2010; Schubert et al., 2020) and thus may be an important component of the ocean energy cycle (Brüggemann and Eden, 2015).

Within the upper ocean mixed layer, the horizontal spatial scales of mixed layer eddies (MLEs) show large seasonal and spatial variations as they depend on the ocean MLD. The mixed layer Rossby radius, given by

$$L_{ML} = \frac{2\pi}{1.6}\sqrt{\frac{1+Ri}{Ri}}\frac{N_{ML}H_{ML}}{f} \tag{1}$$

is a spatial scale often associated with submesoscale baroclinic MLEs, as it is proportional to the length scale of the fastest growing mode according to linear stability analysis (Stone, 1966). Here N^2_{ML} is the vertical stratification averaged over the mixed layer, H_{ML} is the mixed layer depth, f is the Coriolis parameter, and Ri is the balanced Richardson number averaged vertically over the mixed layer depth.

$$Ri = \frac{N^2_{ML} f^2}{M^4_{ML}} \tag{2}$$

with M^2_{ML} denotes the horizontal buoyancy gradient averaged over the mixed layer. Similarly, the maximum growth rate σ_{ML} of such instabilities can be estimated from linear instability to

$$\sigma_{ML} = 0.3\sqrt{\frac{Ri}{1+Ri}}\frac{M^2}{N}. \tag{3}$$

These length and time scales indicate that during winter conditions, when stratification is low and the mixed layer is deep, MLEs grow faster at larger spatial scales. This is why MLEs are found to be more intense in winter conditions (Callies et al., 2015; Mahadevan, 2016; Sasaki et al., 2017; Dong et al., 2020b).

To account for the re-stratifying effects of MLEs, parameterizations for submesoscale baroclinic mixed layer instabilities were developed (e.g. Fox-Kemper et al., 2008; Stone, 1966; Zhang et al., 2023; Bodner et al., 2023; Green, 1970). These parameterizations estimate eddy buoyancy fluxes based on the baroclinicity of the current (baroclinicity indicates the presence of fronts). The parameterized fluxes act to flatten isopycnals and thereby re-stratify the upper ocean. To this end, they act in a similar way to the Gent-McWilliams parameterization (Gent and Mcwilliams, 1990), which accounts for mesoscale baroclinic instabilities in the interior of the ocean (see Gula et al., 2021). Numerous studies have evaluated and optimized MLE parameterizations in idealized setups (Stone, 1966; Fox-Kemper et al., 2008; Mahadevan et al., 2010; Brüggemann and Eden, 2014; Zhang et al., 2023; Bodner et al., 2023). While Zhang et al. (2023) and Bodner et al. (2023) include frontal straining into the scaling assumption of the frontal width to improve the parameterization, Calvert et al. (2020) and Bodner et al. (2023) also evaluate the impact of

the parameterization applied in coarse resolution models, on e.g. the mixed layer depth.

Evaluations of such parameterizations in realistic model configurations that simulate dynamic flow conditions, with time-varying background currents, a rich mesoscale eddy field, realistic surface wind and buoyancy forcing, and small-scale turbulence, are sparse, although a few studies do exist (e.g. Capet et al., 2008a; Gula et al., 2014; Su et al., 2018; Chrysagi et al., 2021; Uchida et al., 2022). Most of these configurations, however, are regional models nested within coarser global ocean models, often relying on rather unrealistic or engineered boundary conditions at each nest. Uchida et al. (2022) use model simulations with submesoscale resolution in the North Atlantic and perform some basic evaluations of the parameterization proposed by Fox-Kemper et al. (2008). Yet, they only evaluate the vertical buoyancy flux and only focus the average effect within a large spatial domain. A detailed analysis of the re-stratification of ocean fronts by submesoscale MLEs and a comprehensive assessment of how parameterizations capture this process in a realistic environment is still lacking.

In this study, we investigate re-stratification of upper-ocean fronts by submesoscale MLEs in a realistic model configuration[1] with a regional resolution that allows for an appropriate quantification of submesoscale overturning in the presence of background currents, Ekman buoyancy fluxes and diabatic mixing. Therefore, we use a novel global ocean model configuration with a telescoping grid that resolves the submesoscale over a large region in the North Atlantic. We apply a spatial resolution of less than 1 km which is therefore, much finer than what is typically used in realistic ocean model simulations and that is also finer compared to the simulations analyzed in Uchida et al. (2022). We furthermore assess how two parameterizations for MLEs, one parameterization from Stone (1966) based on ageostrophic linear stability analysis; one parameterization from Fox-Kemper et al. (2008) based on parcel theory are able to capture mixed layer overturning.

This paper is structured as follows: In Sec. 2.2 we introduce the novel ICON configuration and evaluate its ability to resolve dynamics on the kilometer-scale with, among others, novel satellite data from the SWOT mission. In Sec. 2.3 we analyze how submesoscale eddies re-stratify ocean fronts, we diagnose eddy buoyancy fluxes and the corresponding overturning streamfunction. Additionally, potential challenges in accurately diagnosing the mixed layer depth within the novel submesoscale resolving ICON configuration are addressed. In Sec. 2.4, we evaluate how well two parameterizations for submesoscale eddies are capable of representing the diagnosed eddy fluxes. To this end, we analyze the situation at individual fronts and eddies but also for an entire domain in the North Atlantic. We close this study with a brief summary of the results and concluding remarks in Sec. 2.5.

1 We use 'realistic' in the sense that we apply realistic topography and use re-analysis data as surface boundary conditions. Despite that our model configuration is subject to inaccuracies originating from errors due to numerics and parameterizations.

2.2 SUBMESOSCALE TELESCOPE MODEL

2.2.1 *Model Configuration*

Simulating submesoscale dynamics on a global scale remains challenging due to the high computational demands required. In our study, we reduce those computations by employing a novel configuration of the ocean model ICON-o (Korn et al., 2022; Hohenegger et al., 2023), which supports local grid refinement. In this configuration, submesoscale eddies are only resolved within a focus area. Therefore, we refer to this simulation as the ICON SubMesoscale Telescope configuration or ICON-SMT. The structure-preserving discretization of the primitive equations in ICON-O allows to continuously refine the grid resolution (see Korn et al., 2022). In ICON-SMT, the horizontal resolution[2] varies between 530 m in the focus area that we chose to be in the North Atlantic and 11 km away from this focus area (see Fig. 7 for more details regarding the horizontal resolution). We will show in the following, that this resolution allows simulating submesoscale dynamics in the upper-ocean of the North Atlantic. The vertical grid consists of 112 layers with a resolution of less than 3.5 m in the upper 152 m, allowing a good representation of mixed layer processes, even in winter conditions where the deepest mixed layers are expected to reach 400 m, we obtain a maximum level thickness of 20 m.

In ICON-o, we solve the primitive equations where Boussinesq, hydrostatic and traditional approximations were made. We furthermore use a prognostic equation for turbulent kinetic energy (TKE) following (Gaspar et al., 1990) to simulate vertical mixing of tracer and momentum. We do not use any explicit horizontal tracer diffusion but employ an advection scheme which is explained in detail in Korn (2017). For horizontal momentum dissipation, we apply a biharmonic friction operator where the biharmonic viscosity varies with the grid resolution according to $K^{\nu} = K_{\text{ref}}\sqrt{|e||e^{\perp}|}^{3}$, with $|e||e^{\perp}|$ the edge length and the cell center distance, respectively and $K_{\text{ref}} > 0$ is a fixed reference viscosity (Korn et al., 2022).

We initialize ICON-SMT by interpolating data from a coarser ICON-o simulation with 10 km grid spacing (ICON-R2B8) that ran for more than 100 years forced in the initial phase by the MPI-OMIP forcing (Chassignet et al., 2020, see) and for the years 1960-2010 with ERA5 reanalysis data (Hersbach et al., 2023). ICON-SMT continues ICON-R2B8 by running from 1st January 2010 forced with ERA5 data of that period. We use identical parameters in both configurations except for time step and biharmonic viscosity coefficient that have been adjusted according to the lower resolution of ICON-SMT. ICON-SMT is run from January to March 2010, with model output generated at two-hour intervals. A period in the late winter is selected for this study, as the appearance of SMD are known to be more pronounced during this time (e.g. Mahadevan, 2016).

During the spinup of the submesoscale eddy field that roughly takes two weeks, we observe that the mesoscale fronts of the input data become unstable and a vibrant submesoscale eddies emerge that are characterized by enhanced local Rossby numbers (defined as relative vorticity divided by planetary vorticity, see Fig. 7).

2 Note that the resolution in ICON is defined as the square root of the area of a triangle face. This definition overestimates the geometric resolution by 25% (Danilov, 2022) Regarding this geometric definition of resolution, the highest ICON-SMT resolution is 662.5 m.

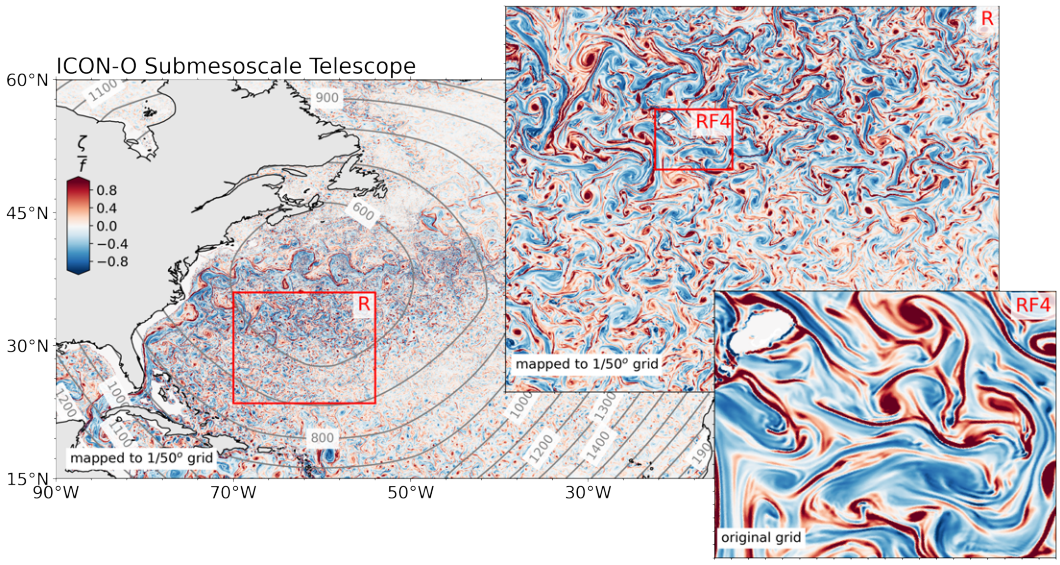

Figure 7: A snapshot of the Rossby number (relative over planetary vorticity) on 18 March 2010 in the North Atlantic and the horizontal resolution of the ICON-SMT grid as grey contours. R: Zoom in on the focus region with the highest horizontal model resolution. RF4: A submesoscale filament shown at grid scale.

Rossby numbers of order one that indicate the presence of ageostrophic dynamics are merely absent in ICON-R2B8 with 10 km resolution but they can be frequently found in the area of ICON-SMT where the grid is refined (see Fig. 7R).

2.2.2 *Model Evaluation*

Observing MLEs poses significant challenges due to their spatial scales, which are too small to be adequately covered by previous satellite missions, and too large to allow frequent and systematic ship- or glider-based observations (McWilliams, 2016). Nevertheless, new satellite products have emerged that allow to observe scales close to the kilometer scale and even beyond. In this section, we apply several such satellite products to demonstrate the ability of ICON-SMT to resolve the scales required to simulate submesoscale turbulence in the mixed layer.

Before we start with this evaluation, we begin with examining the model's MLD and compare it with a recent climatology (Boyer Montégut C., 2023). Since the vertical and horizontal MLE scale and the strength of MLE fluxes depend on the mixed layer depths, this assessment is crucial to classify the realism of the simulated MLE fluxes. Afterwards, we assess the anticipated horizontal length scales of MLEs to estimate how well these eddies can be resolved in ICON-SMT. Finally, we examine satellite products and a high-resolution intercomparison study by Uchida et al., 2022 to assess submesoscale surface variability in wavenumber and frequency space, respectively.

It is important to note that due to the short run time of ICON-SMT, the slowly varying ocean quantities such as the large-scale currents and meanders will not deviate much from the spinup (see Korn et al., 2022 for a validation of the simulation that we used as spinup). This is why many biases of the ICON-SMT simulation

e.g. regarding the position of the Gulf Stream and North Atlantic current as well as mixed layer depth and water mass properties are inherited from the coarser spinup simulation. We nevertheless apply some evaluation of these background characteristics in order to provide an estimate to which degree the subsequently developing submesoscale eddies might be affected by the biases of the spinup. Here, we focus on evaluating quantities within the study area that are relevant to submesoscale instabilities and eddies, such as the MLD, the Sea Surface Temperature (SST)-, and Sea Surface Height (SSH)-variability at and below the mesoscale Rossby radius.

2.2.2.1 *Mixed Layer Depth*

The mixed layer depth is a crucial diagnostic for the evaluation of MLE, as it influences the characteristic length scale of the corresponding dynamical regime (see following Sec. 2.2.2.2). In this study, we use offline density threshold diagnostics (de Boyer Montégut, 2004) on both monthly and weekly averages to diagnose the MLD. The density is computed from averaged potential temperature and absolute salinity fields using the python GSW package (**McDougall2011**). Monthly averages are used to validate the background MLD in agreement with large-scale observational estimates based on ARGO data (Wong et al., 2020) which are averaged over comparable time periods. The latter weekly averaging period, appears more appropriate for determining the vertical scale of MLEs on MLE time scales which are on the order of days and typically shorter than a month (see Sec. 2.3.3 for a more detailed analysis of vertical MLE scale).

In Figure 8, we compare the monthly mean MLD of the present model with a recent climatology from Boyer Montégut C., 2023. We note that the climatological dataset is based on monthly averages of March over several decades, whereas our model average is based on a single month and is therefore imposed by non-averaged mesoscale features such as eddies and currents. The density threshold of $\Delta\rho = 0.03\,\mathrm{kg\,m^{-3}}$ based on de Boyer Montégut, 2004 is used for both datasets after applying the time average.

It is apparent, that the ICON-R2B8 spinup suffers from a too zonal crossing of the North Atlantic Current and a missing Northwest Corner. The integration period of the ICON-SMT simulation is too short to substantially change these characteristics and therefore inherits some related biases from the coarser ICON-R2B8 spinup. This can e.g. be seen in the SST bias (see Fig. 22), where the onshore temperatures are too warm compared to observations while the offshore temperatures are too cold. In particular, the missing Northwest Corner leads to a cold temperature bias and to too shallow mixed layer depths east of Newfoundland. The model also underestimates the MLD in the eastern half of the North Atlantic and in the tropical Atlantic. However, within the region of primary interest (denoted by the red rectangle in Fig. 8), we observe a generally reasonable agreement of the MLD between our model and observations. ICON-SMT shows more horizontal variability compared to the observations. This is most likely related to the limited amount of data points of the observations data and the extrapolation to areas with limited data coverage. The mixed layer depth in the study area varies between 15 m and 300 m and at least in ICON appears to be correlated with mesoscale eddy structures.

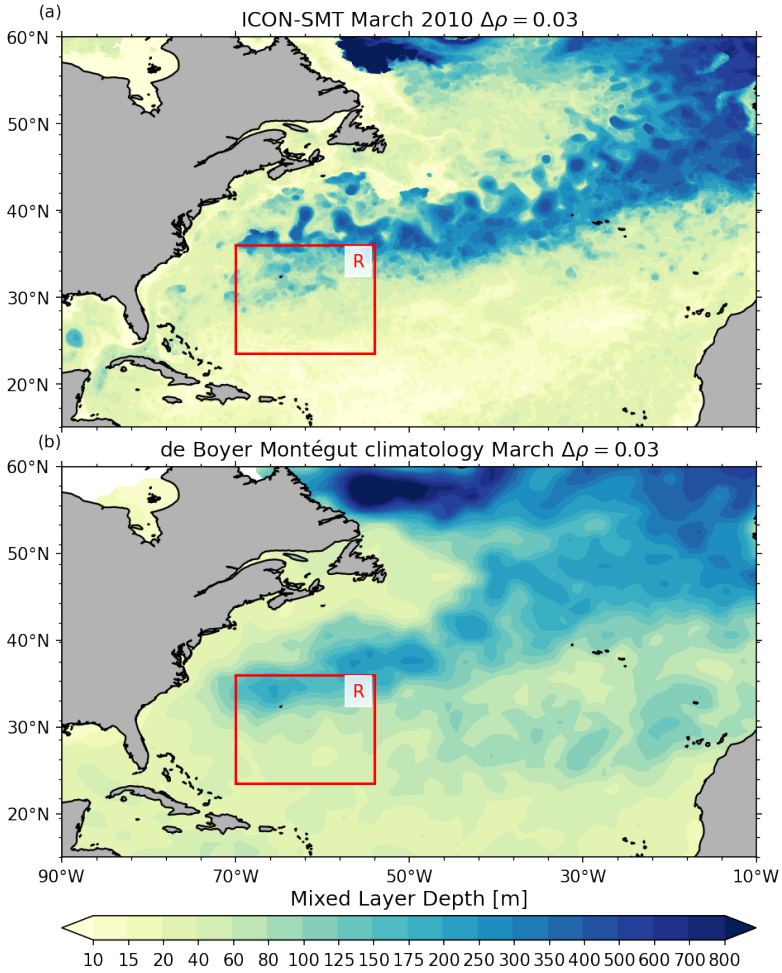

Figure 8: The mean MLD of March 2010 from ICON-SMT is compared to the MLD climatology for March from Boyer Montégut C. (2023), which is based on measurements collected between 1970 and 2021. The red box indicates the study area. Note the varying spacing in the contour levels.

2.2.2.2 *Wavelength of the fastest growing mode*

The first baroclinic Rossby radius of deformation serves as a critical measure for the spatial scales of mesoscale eddies. In our focus area, it is typically between 30 and 60 km, (see Fig. 6 in Chelton et al., 1998). Mixed layer eddies, in contrast, appear on much smaller scales. When originating from baroclinic instability, the scale of the fastest growing unstable mode is given by Eq. 1. In our study area L_{ML} varies between 15 and 50 km (see Fig. 9a) and matches well with the fastest growing linear mode computed from observations by Dong et al. (2020a). Note that the wavelength of the fastest growing mode L_{ML} strongly correlates with the mixed layer depth (see also Fig. 8a).

In ICON-SMT, the horizontal resolution is substantially smaller compared with the wavelength of the fastest growing mode (see grey contour lines in Fig. 8). In regions with deep mixed layers, the model resolution appears to be up to 100 times finer than the wavelength ($L_{ML} >> 50$ km), however towards the southern boundaries of the study area the ratio drops below 40, corresponding to the shal-

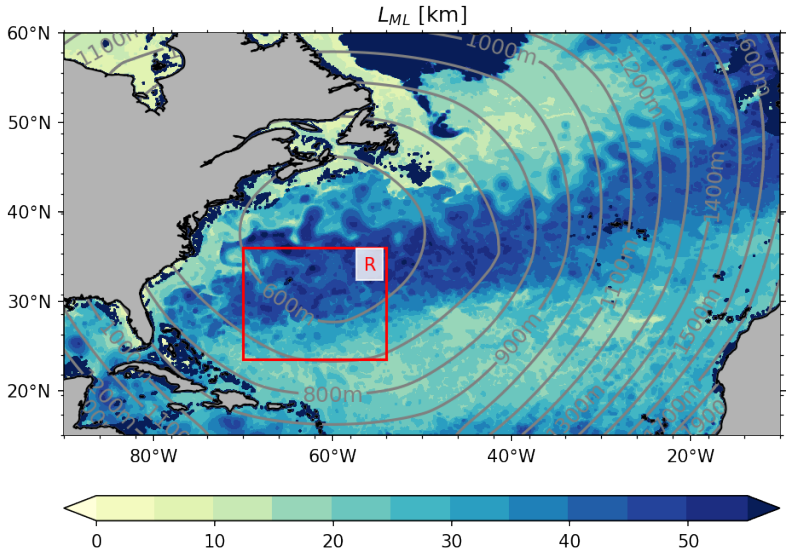

Figure 9: The wavelength of the fastest growing mode calculated via Eq. 1. The MLD is diagnosed with $\Delta\rho = 0.2\,\mathrm{kg\,m^{-3}}$ criterion. Grey contour lines indicate the horizontal resolution of ICON-SMT.

lower MLD and wavelength of ($L_{ML} < 20\,\mathrm{km}$). Typically, $10-20$ grid points are necessary to fully resolve a wave; here ICON-SMT satisfies this requirement even in regions with shallower mixed layer depths within the study area. For the evaluation of frontal dynamics (see selected fronts in Sec. 2.3.1), we exceed a ratio of 40 (not shown). This gives us confidence that our resolution is sufficiently high to resolve MLEs, but it also highlights the observations of Hohenegger et al. (2023), where submesoscale dynamics were largely suppressed at resolutions greater than 1.25 km. Moreover, we find strong overturning circulation at strong frontal gradients, which correspond to deep mixed layers as will be shown below (see Sec. 2.3). We apply a vertical resolution of less than 3.5 m in the upper 152 m which implies roughly 20 levels in the southern half of our study area where the MLD is roughly 60 m deep and more than 50 levels in the northern half, where the MLD is deeper than 150 m (see Fig. 8).

2.2.2.3 *Variability on small and large scales*

Resolved MLEs can lead to increased variability of ocean quantities in space and time, which can be easily inferred by comparing ICON-SMT with coarser resolution models, such as ORAS5 (0.25°), e.g. a widespread increase in oceanic energy throughout the North Atlantic (not shown). In this section we seek to evaluate the variability of ICON-SMT with satellite observations and recent submesoscale resolving simulations. Therefore, we examine some commonly used satellite products such as the SST from Modis-Aqua, 2019 (L3 product at 4.63 km) and the SSH from Aviso-C3S, 2021 (L4 product at 0.25°). However, these products suffer from relatively coarse spatial resolution, which prevents them from capturing the essential high-resolution features that we seek to validate. Thus, we also include the SSH from SWOT, 2023 (L3 product at 2 km), the recently launched Surface Water

and Ocean Topography (SWOT) mission. Also, we include the 10 km spinup run (ICON-R2B8), which serves as a reference for eddy resolving models.

COMPARISON TO MODIS-AQUA AND AVISO-C3S The SST measurements of Modis-Aqua (2019) are based on an infrared radiometer, which cannot penetrate clouds what severely limits the evaluation. Here, the snapshot (not shown) with the largest coherent cloud-free area over the North Atlantic in March 2010 is selected to evaluate zonal and meridional wavenumber spectra. The SST of ICON-SMT and ICON-R2B8 are interpolated from the native grid to regularly spaced sections with approximately 660 m and 10 km spacing, respectively. The corresponding satellite resolution is 4.63 km. For ICON-SMT and Aviso-C3S each domain consists of 180 realizations (or temperature sections), while the coarser resolution of ICON-R2B8 allows only 90 realizations. Finally, the wavenumber spectra of each realization is computed[3] and averaged to an overall zonal (see Fig. 10) and meridional wavenumber spectra. The meridional averaged spectra does not show any qualitative difference to the zonally averaged spectrum (not shown).

For the evaluation of SSH variability with Aviso-C3S (2021), we use basically the same diagnostic as above, but with some specific adaptations. Unlike Modis-Aqua (2019), Aviso-C3S (2021) is based on microwaves and is able to penetrate clouds, thus allowing more temporal realizations (Aviso-C3S, 2021 L4 product has a daily temporal resolution). A trade-off is that the spatial resolution is about an order of magnitude coarser. Therefore, we refined the diagnostic approach by selecting slightly larger spatial domains (not shown) and incorporating daily temporal snapshots from January to March, resulting in a total of 5400 realizations.

The zonal wavenumber spectra of SST and SSH are shown in Fig. 10. We observe larger confidence intervals for ICON-R2B8 associated with the smaller number of realizations in subfig. 10a. However, the inclusion of additional temporal realizations helps to reduce the width of the confidence intervals, as can be seen in subfig. 10b.

Throughout the observed wavenumber band of the SST and SSH spectra ICON-SMT is in good agreement with observations, while ICON-R2B8 has significantly lower amplitudes at intermediate wavelengths, see Fig. 10. However, for each spectral estimate we note the dominance of white noise towards the high wavenumber end of the spectrum (or close to respective sampling frequencies/rates). This is probably a consequence of the increasing dominance of instrumental noise in the observations and grid noise in the model. However, the method to derive spectrum may also have a small influence, as subsampled model datasets show white noise at the high wavenumber end of the spectra (not shown).

We conclude that the high resolution of ICON-SMT leads to an increased energy in the spectra on nearly all scales and aligns well with the observed satellite spectra.

3 Method: Each signal is detrended by its mean. Then the numpy fft function is applied and multiplied by its complex conjugate and scaled by the factor $1/(fs(n/2))$, with the sampling frequency (grid spacing in m) f_s and the number of samples n. Since the number of realizations is sufficient, no smoothing techniques are applied. Remaining data gaps are filled by linear interpolation. The 95% confidence intervals are added, assuming a T-Distribution, typically used when the sample size is small or the population variance is unknown. Note that n does not represent truly independent realizations, which could introduce dependencies that the t-distribution assumption does not account for fully.

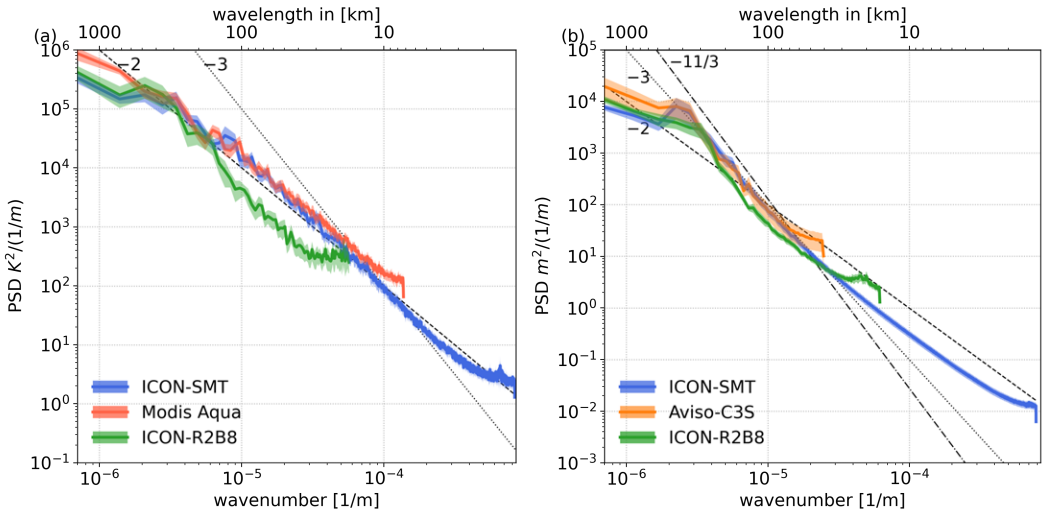

Figure 10: The zonal wavenumber spectra of the SST (a) and the SSH (b) from model and satellite observations. The color shadings along the spectral lines indicate the 95% confidence intervals. The Nyquist wavenumbers differ due to the differences of model resolution and mean latitude of the subdomains. Note, that the Nyquist wavenumber for ICON-SMT is roughly 1.2 km.

By explicitly resolving smaller scales, we do not only resolve submesoscale features but also improve the representation of the larger scales. As a result, we find more realistic variability at both small and large scales. Due to the resolution limitations of the satellite data, we cannot validate the full extent of the resolved submesoscale band with these commonly used satellite products.

COMPARISON TO SWOT Obviously, the resolution of Aviso-C3S, 2021 is too coarse to evaluate the simulation on scales where MLEs occur. The recently launched SWOT mission provides a useful alternative with higher resolution. Here, we make a first attempt to use SWOT, 2023 to evaluate a realistic simulation resolving MLEs. Therefore, we compare the SWOT along-track spectra with our ICON configurations. SWOT, 2023 now offers the first L3 processing products that interpolate gaps and handle flags from the L2 product. More importantly, it introduces an AI-based, noise-reduced SSH anomaly with a resolution of 2 km along the track, allowing the first comparison of SSH wavenumber spectra at these scales. However, as the L3 product, and in particular the AI-based noise reduction, is still under development, the results should be treated with caution.

To cover the entire planetary surface, SWOT's Ka-band Radar Interferometer (KaRin) instrument completes a cycle every 21 days. From a single cycle in March 2023, we selected 27 satellite tracks covering our study area, shown in Fig. 29. Satellite tracks with gaps larger than 15% are dropped, see Fig. 29 the remaining tracks have gaps which are typically smaller than 1%. The SSH of ICON-SMT and ICON-R2B8 are interpolated on the satellite tracks and times (each track is treated as a snapshot with a mean time). Since the resolution of ICON-R2B8 is coarser and the resolution of ICON-SMT is finer than the along-track sampling of SWOT, ICON-R2B8 is mapped to a subsampled satellite track, corresponding to 10 km resolution, while ICON-SMT is mapped to an oversampled satellite track

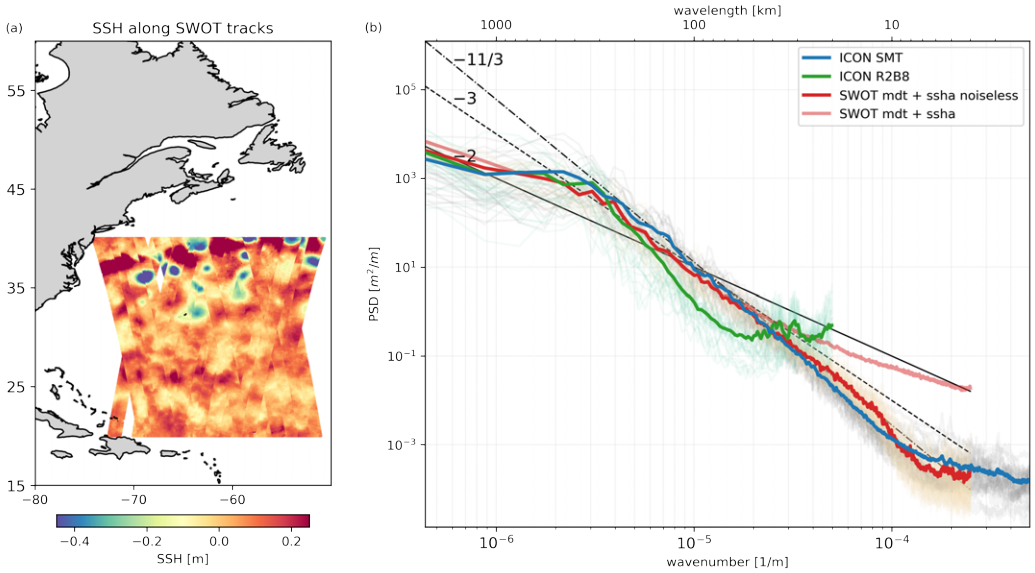

Figure 11: (a) the SSH anomaly of along SWOT satellite tracks. (b) the along-track SSH anomaly wavenumber spectra of SWOT noiseless (red), SWOT 'raw' (light red), ICON-SMT (blue) and ICON-R2B8 (green). Each track consists of 69 realizations, which are averaged to a single spectrum. Thus, we present the mean spectra of all relevant tracks (full color) and the mean spectra of each individual track (shown in same color with less opacity).

of approximately 1 km resolution. Note that the ICON simulations cover a winter period in 2010, not 2023. Each track consists of 69 realizations, which are used to compute a mean wavenumber spectra. Due to significantly larger datasets the python software XRFT (Fourier Transform for xarray) (**Uchida2023_xrft**) is used to compute the wavenumber spectra. The applied configuration includes linear detrending and a hanning window (see Uchida et al., 2022, for more details). The overall mean spectra and the corresponding satellite tracks are shown in Fig. 29.

The small spread between the mean of all tracks and the mean of each individual track (same color with less opacity) indicates a robust method for both the model configurations and SWOT. We find an overall agreement for wavelengths $\lambda > 300$ km. For intermediate wavelengths, the variability of ICON-R2B8 decreases and shows a steeper slope. For ICON-SMT and SWOT we observe a strong agreement up to wavelengths $\lambda > 60$ km. At these wavelengths, the noise from the SWOT interferometer becomes significant, as shown by the flatter slope of the raw spectra compared to the noise-filtered SWOT spectra. Towards wavelengths $\lambda > 10$ km the noise-filtered SWOT spectra is slightly shallower than ICON-SMT. These differences could be attributed to either insufficient model resolution or inadequacies in the AI-based noise reduction method used in SWOT (2023), which is still under development and should be approached with caution. We emphasize that we are evaluating a wavenumber range of the SSH anomaly that was, until recently, unknown to both observations and simulations. We note that the slope of ICON-SMT is slightly steeper than SWOT. Future products from SWOT (2023) may allow an assessment closer to the native 250 m KaRin resolution.

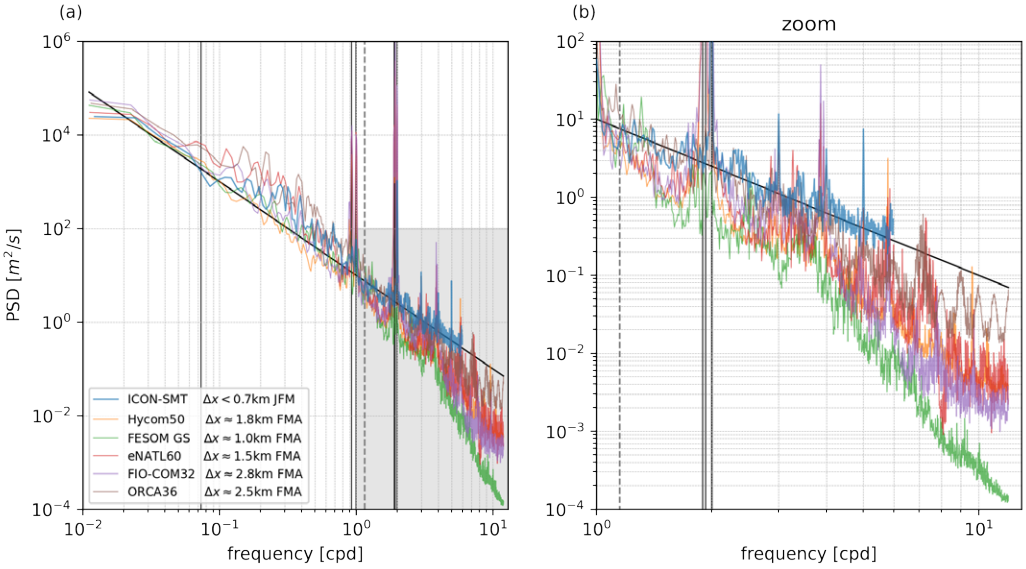

Figure 12: The SSH frequency spectra of a 3-month time series over the North Atlantic. Curves for all models except of ICON-SMT are reproduced from Uchida et al. (2022). The approximate grid resolutions are given in the legend. Note that the simulation of ICON-SMT, FESOM-GS and ORCA36 are not tidally forced. The vertical lines indicate the first eight major tidal frequencies (see Gill, 1982), the dashed vertical line indicates the Coriolis frequency at 35°N. Additionally, the spectral slope of -2 is included.

COMPARISON WITH RECENT HI-RES SIMULATIONS To further evaluate the performance of ICON-SMT, we compare SSH frequency spectra with some exemplary models from Uchida et al. (2022). Notable differences between our simulation and that from Uchida et al. (2022) are: (1) the time period covered by the models, in Uchida et al. (2022) this is from February to April and thus one month later compared to our simulation, and (2) the sampling interval in ICON-SMT is every 2 hours while it is one hour for the other models. However, we do not expect major influences from those differences. We compute the spectra using from time series from January to March for all grid points within the Gulf Stream separation region in the North Atlantic (see Uchida et al., 2022). Finally, we average all obtained spectra that we obtained for this domain. Also, note that ICON-SMT has a higher resolution compared to the simulations used in Uchida et al. (2022).

The SSH frequency spectra shown in Fig. 12 are calculated according to Uchida et al. (2022) for ICON-SMT and for some exemplary models of Uchida et al. (2022) that were available to us[4]. Note that the tidal forcing in ICON-SMT is switched off in the present configuration, while some reference models include tidal forcing (for a detailed description of model configurations see Uchida et al., 2022). On large and intermediate scales, periods from months to days, we observe good agreement between ICON-SMT and the reference models. The diurnal and semi-diurnal peaks are visible in ICON-SMT despite the absence of tidal forcing. Moreover, at the high frequency end of the spectrum, ICON-SMT shows slightly higher energy

4 The data of the model simulation from Uchida et al. (2022) that we used here can be found at `https://github.com/roxyboy/swot_adac_ogcms/tree/notebook`. It is licensed under the Apache License 2.0.

levels compared to all reproduced models. However, these energy levels might be similar to LLC4320 (not shown, since due to data access issues, the output of the LLC4320 and GIGATEL model could not be reproduced and are therefore not included in this evaluation), which have slightly higher amplitudes than other recalculated spectra (see their Fig. 4a in Uchida et al., 2022). Nonetheless, it appears that the model resolution is of similar importance as the tidal forcing, and thus the number of resolved constituents. Considering our comparison with satellite observations, we argue that we need more rather than less variability towards high frequencies (see Fig. 29). Despite the absence of tidal forcing, which also affects the energy levels at the high-frequency end of the spectrum, ICON-SMT has comparable maybe somewhat higher energy levels compared with the other models.

2.3 MIXED LAYER EDDIES

After having demonstrated the ability of the model to resolve ocean variability on scales far smaller than the mesoscale (defined by the first baroclinic Rossby radius), we now focus on the role of MLEs in re-stratifying the ocean mixed layer. To quantify submesoscale eddy fluxes, we apply the usual Reynolds decomposition of the buoyancy equation (see e.g. Olbers et al., 2012):

$$\partial_t \overline{\mathbf{b}} + \nabla \cdot \overline{\mathbf{v}}\overline{\mathbf{b}} + \nabla \cdot \overline{\mathbf{v}'\mathbf{b}'} = Q \tag{4}$$

where b denotes buoyancy, $\mathbf{v}$ denotes velocity, Q denotes any diabatic terms from forcing and molecular diffusion. An average is denoted by an overline $\overline{(\cdot)}$ and deviations from that average are denoted by a prime $(\cdot)' = (\cdot) - \overline{(\cdot)}$. Such an average could be constructed for instance by a time, space or ensembles filter. In this study we apply a one-week time filter and also a spatial filter for comparison (see Sec. 2.3.3 and Sec. 2.4.3). For spatial filtering, we use a Gaussian filter with a standard deviation of 30 km based on Uchida et al. (2022) to facilitate model inter-comparisons. Here, we used the Python package GCM-FILTERS (Grooms et al., 2021) for applying the spatial filter. Analogous to the temporal decomposition, the spatially smoothed field describes the mesoscale and the residual describes the submesoscale.

Following Andrews et al. (1987) the eddy fluxes can be decomposed into a parallel and perpendicular component,

$$\overline{\mathbf{v}'\mathbf{b}'} = \psi \nabla_{rot} \overline{b} - \nabla \cdot K_d \nabla \overline{b} \tag{5}$$

with the diapycnal diffusivity K_d and the overturning streamfunction ψ. Note that the operator is defined as $\nabla_{rot} = (-\partial z, \partial y)$. With Eq. (5) the buoyancy equation Eq. (4) can be written as

$$\partial_t \overline{\mathbf{b}} + \nabla \cdot (\overline{\mathbf{v}} - \nabla_{rot}\psi)\overline{\mathbf{b}} = Q + \nabla \cdot K_d \nabla \overline{b}, \tag{6}$$

where $\nabla \cdot K_d \nabla \overline{b}$ denotes the diffusive eddy fluxes. In this study we focus on the overturning by MLEs and and do not consider K_d in the following.

We choose mesoscale fronts and eddies to define the background field for the MLEs. We describe a front by two non-dimensional numbers and two-dimensional parameters. Here, we follow the notation of Brüggemann and Eden (2014) who

chose the mixed layer depth H and the Coriolis parameter f as dimensional parameters and further characterize the background state by two non-dimensional numbers, (1) the balanced Richardson number $Ri = \frac{N^2 f^2}{M^4}$ where $N^2 = \frac{\partial}{\partial_z}\overline{b}$ is the vertical buoyancy gradient and $M^2 = \frac{\partial}{\partial_{\hat{y}}}\overline{b}$ is the horizontal or more precisely the cross-frontal buoyancy gradient and (2) by the ratio of the horizontal buoyancy gradient and the Coriolis parameter $\alpha = M^2/f^2$ (see Brüggemann and Eden, 2014, for details). Here, we simplify the nomenclature by using rotated coordinate systems, where $\hat{x}$ denotes the along-front direction and $\hat{y}$ denotes the cross-front direction and $\hat{u}$ and $\hat{v}$ for the respective along-front and across-front velocities. Note that we will define such coordinate systems individually for each detected front.

Using the above notation and coordinate system, the streamfunction in Eq. (5) can be expressed as

$$\psi = \frac{\overline{\hat{v}'b'}N^2 - \overline{w'b'}M^2}{|\nabla\overline{\mathbf{b}}|^2}. \tag{7}$$

The definition of the streamfunction is such that a positive value indicates a clockwise and a negative value a counterclockwise circulation. Note that the first term in the numerator in Eq. (7) tends to be much larger than the second term and thus dominates the streamfunction in most situations. Exceptions occur under extremely strong lateral gradients and vertical buoyancy fluxes, as highlighted by the differences shown in Fig. 24. Note also that there are other formulations of the streamfunction that only consider one of the terms in the numerator in Eq. (7) (Held and Schneider, 1999; Andrews and McIntyre, 1976). We discuss problems with these simpler forms that arise in diagnosing the streamfunction in Appendix 2.6.

2.3.1 *Phenomenology of submesoscale fronts*

Since submesoscale eddies are known to occur along strong horizontal density fronts that are baroclinically unstable, we begin with a simple approach to detect individual ocean fronts and diagnose their background characteristics before we derive the associated eddy fluxes and the MLE overturning circulation. MLEs develop due to baroclinic instability in which course energy is transferred from the available potential energy, associated with tilted isopycnals, to the eddy kinetic energy. The net effect is the flattening of the isopycnals. Linear stability analysis suggests that the maximum growth rate σ of such instabilities scales with the cross-front buoyancy gradient $\sigma \propto M^2/N^2$ (Stone, 1966). This indicates that the most unstable fronts can be found for fronts with strong lateral buoyancy gradient and weak stratification.

To isolate the processes occurring on individual submesoscale fronts, we use the horizontal buoyancy gradient (Fig. 13a) from a seven-day time average to visually identify 45 fronts within domain R. We furthermore encapsulate each front in a rectangular box (red dotted lines in Fig. 13), where the along- and across-front directions define the coordinates $\hat{x}$ and $\hat{y}$, respectively. The lengths and widths of the boxes are furthermore used to restrict respective along-front and across-front averages. A closer inspection of all 45 fronts, indicates that they are characterized by enhanced horizontal buoyancy gradients (Fig. 13a, b, g and h) and weak bal-

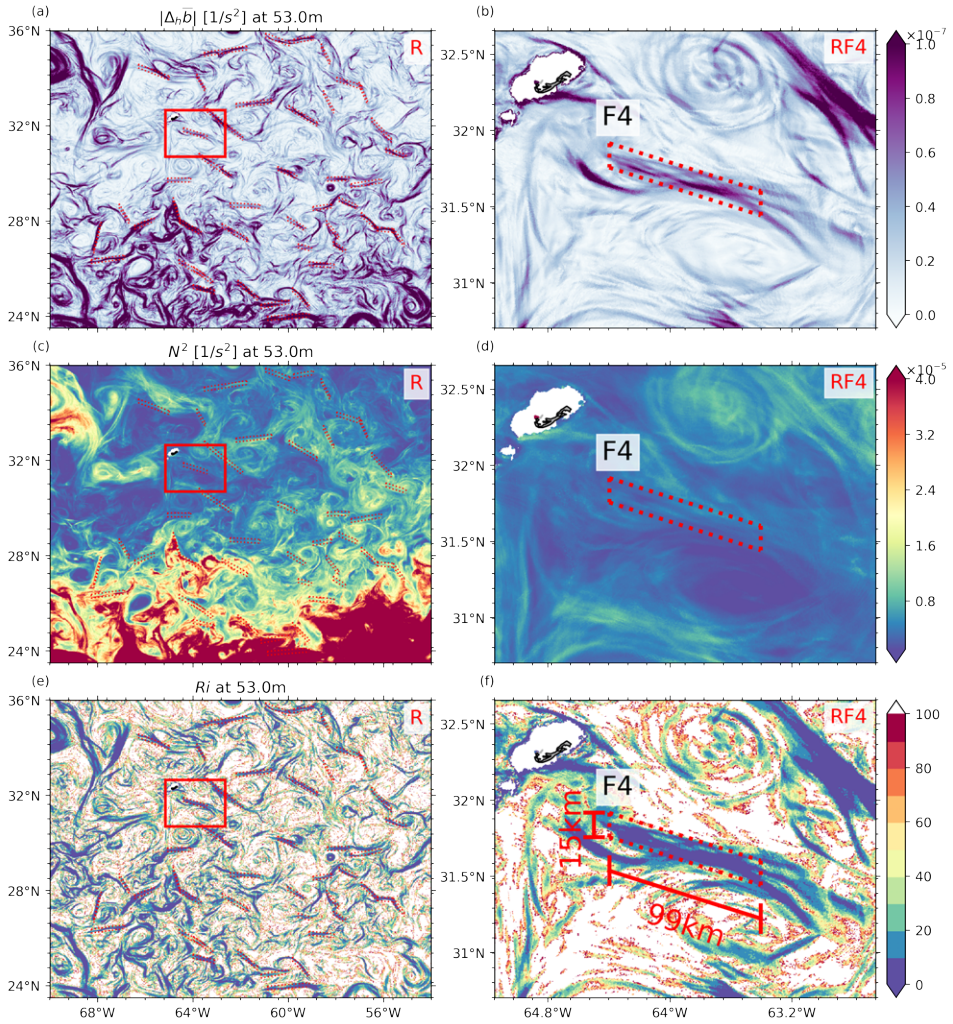

Figure 13: Upper-ocean fronts within the entire study area (left) and zoom onto a single front (right). Colors show absolute values of the lateral buoyancy gradient (a and b), the squared Brunt-Väisälä Frequency (c and d), the local balanced Richardson number (e and f). The detected fronts are indicated by red dotted rectangles.

anced Richardson numbers (Fig. 13e and f). We note that for many fronts even the vertical stratification appears to be enhanced, which is probably a consequence of the already ongoing re-stratification process by MLEs. We note further, that the Richardson number within each front drops to a value smaller than ten and thus closer to one.

It is illustrative to discuss the dynamics at a characteristic front in more detail. To this end, we apply in Fig. 14 along-front averages of the front F4 (depicted in the right column in Fig. 13) of some important background quantities as vertical and horizontal density gradient but also of the vertical and meridional eddy fluxes as well as the eddy streamfunction. It becomes apparent that a well-defined maximum in the magnitude of the lateral density gradient (Fig. 14a) with reduced balanced Richardson number (Fig. 14c) is located at the center of the front above the base of the mixed layer. The margins of the front (indicated by the black vertical

lines) are roughly located where the lateral buoyancy gradient is small. These margins are also used later on for cross-front averages. The front marks the boundary between water masses with different levels of stratification (Fig. 14b). The northern side (right side in Fig. 14) is colder and less stratified, while the southern side is warmer and more stratified. This pattern is consistent across all fronts in the region, which is not surprising given that the area is strongly influenced by a latitudinal thermal gradient. We also observe an increase in stratification within the front which indicates the re-stratification of the front compared to its environment. Furthermore, we also observe enhanced vertical (Fig. 14d) and cross-front (Fig. 14e) eddy fluxes at the center of the front within the mixed layer. These eddy fluxes yield an eddy overturning (Fig. 14f, derived from Eq. 7) that re-stratifies the front.

Albeit the presence of wind, buoyancy forcing, turbulent mixing, and a potential advection of the front, these eddying overturning resembles remarkable similarities to that of earlier more idealized studies (e.g. Haine and Marshall, 1998; Boccaletti et al., 2007) and that of linear stability analysis (Stone, 1966).

An additional across-front average of the quantities depicted in Fig. 14 illustrates that the vertical stratification is enhanced at the top and base of the mixed layer (Fig. 15a). This could be an indication for stronger MLE re-stratification at the top and bottom of the mixed layer as suggested by Fox-Kemper et al. (2008). The time evolution for the stratification can be obtained by vertically differentiating Eq. 4. If one assumes that the eddy fluxes are the dominant source for re-stratification, this requires enhanced vertical gradients of the eddy fluxes at the top and base of the mixed layer (see Fox-Kemper et al., 2008). Indeed, we can confirm that the vertical gradients of the eddy fluxes are enhanced at the top and base of the mixed layer.

In general, we find a good agreement of the frontal characteristics including the eddy overturning with more idealized studies (e.g. Fox-Kemper et al., 2008; Brüggemann and Eden, 2014). Regarding the cross-frontal eddy fluxes, linear stability analysis (Stone, 1966) and idealized simulations Brüggemann and Eden (2014) suggest that they have a constant profile. Here, we frequently find enhanced eddy cross-frontal eddy fluxes at the surface which are likely a consequence of an additional Ekman component. For many fronts, the vertical profile indeed appears constant below a depth of 50 m. However, we acknowledge that the vertical profiles of the cross-frontal buoyancy fluxes in these simulations with background flow and wind forcing are more complex compared with idealized simulations.

We have extended the above evaluation to all 45 fronts, shown in Fig. 13 that vary in background characteristics such as stratification, mean flow, lateral gradient strength, MLD and forcing. Towards higher latitudes, an almost linear increase in MLD and vertical eddy flux is observed, coinciding with a decrease in stratification (not shown). Profiles of along- and across-averaged stratification, and vertical eddy fluxes for all other fronts are shown in the Appendix Fig. 25. While front 9 is rather similar compared to front 4, front 24 is characterized by a double mixed layer with a weak intermediate pycnocline at 40 m. While we observe the strongest vertical MLE fluxes above the intermediate pycnocline, we find non-negligible vertical buoyancy fluxes until the secondary pycnocline at 100 m. This example indicates the importance of a sensible mixed layer base definition and detection algorithm to

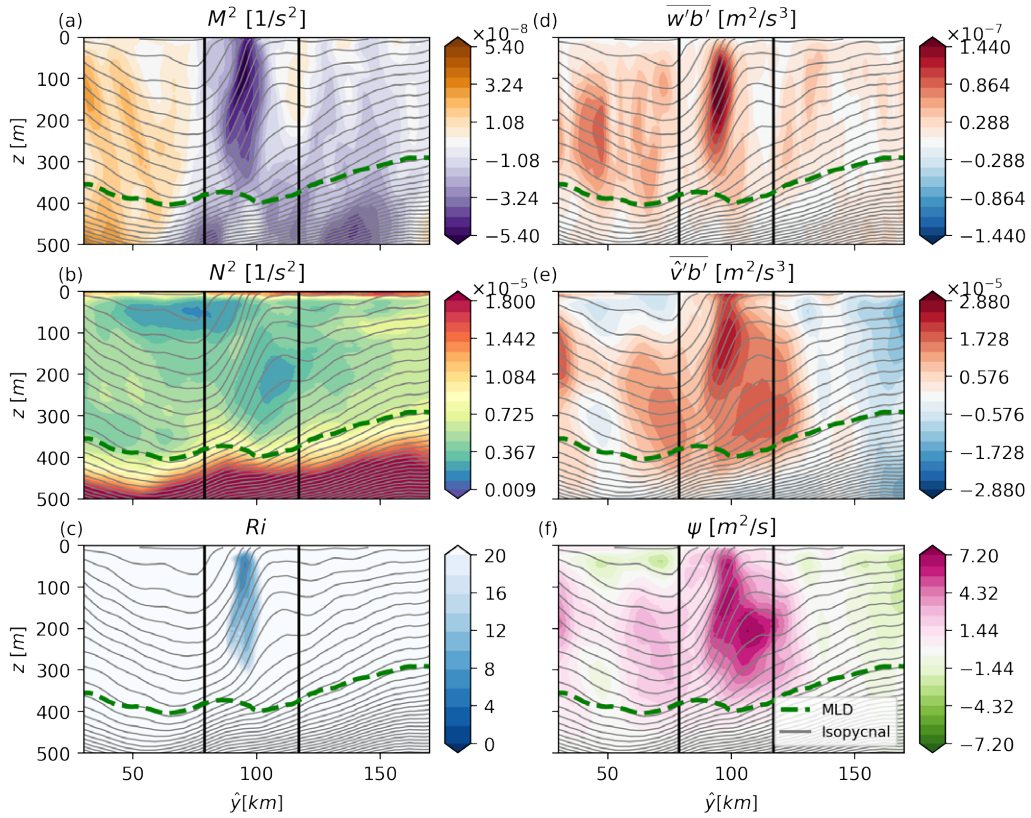

Figure 14: Section across the front F4 depicted in Fig. 13. (a) shows the lateral buoyancy gradient M^2, (b) the stratification N^2, (c) the Ri-number, (d) the vertical eddy flux $\overline{w'b'}$, (e) the cross-front eddy flux $\overline{\hat{v}'b'}$ and (f) a mainly positive (clockwise) eddy stream function ψ calculated via Eq. (7). All variables are averaged along the front F4 in $\hat{x}$ direction. The gray lines denote isopycnals (constant potential density) and the green dashed line denotes the mixed layer base (specified with the threshold criterion $\Delta\rho = 0.2\,\mathrm{kg\,m^{-3}}$). The Coriolis parameter at front F4 is 7.64×10^{-5} rad s^{-1}. The black vertical lines indicate the lateral margins of the front, corresponding to the red dotted rectangle in Fig. 13.

achieve appropriate estimates for the MLE depth scale as we will discuss in more detail below.

Albeit there are notable exceptions, roughly 30 of the 45 fronts show similar characteristics as we discussed for front 4 (Fig. 14 and 15). These include the U-shaped stratification profile and strong vertical eddy fluxes with a parabolic profile peaking at the center of the mixed layer (see e.g. Fig. 15a,c or Fig. 25). In most cases the lateral buoyancy gradient extends beyond the pycnocline, which is not surprising for mesoscale fronts (Mahadevan et al., 2010). In roughly half of the evaluated cases the lateral eddy flux is constant throughout the mixed layer, weakens towards/below the base and peaks towards the surface. The near surface values are 5-10 times stronger, and likely Ekman buoyancy fluxes superimposing the MLE signal. The remaining 15 fronts are somewhat different in the one or the other way. For instance, it is sometimes very difficult to assess a proper mixed layer base due to strong vertical variations in the vertical stratification (see e.g. Front 7, 11, 15, 17, 19,

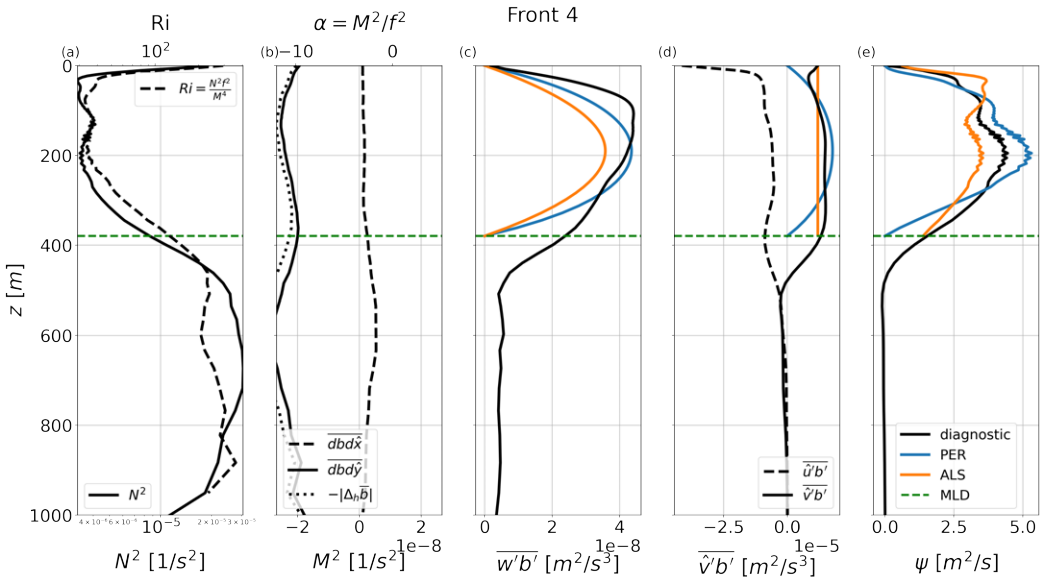

Figure 15: The along- and cross-front averaged variables of front F4 for N^2 solid line and Ri dashed line in (a), across-front (solid line), along-front (dashed line) and absolute (dotted line) horizontal density gradient M^2 and α (b), vertical eddy flux $\overline{w'b'}$ (c), horizontal eddy flux $\overline{\hat{v}'b'}$ (d), and eddy overturning streamfunction Ψ (e). Colored lines in c-e indicated results obtained for the parameterization from ALS (orange) and PER (blue) which are introduced in Sec. 2.4. Note that the secondary axis in (a) represents the Richardson number, while in (b), it reflects an alternative scaling of M^2. The MLD is indicated by a green dashed line (specified with the threshold criterion $\Delta\rho = 0.2\,\mathrm{kg\,m^{-3}}$). The tuning coefficients for the parameterizations are $C_{per} = 0.06$ and $C_{als} = 0.33$, see Sec. (2.4).

in Fig. 25). A negative overshoot of the vertical MLE fluxes can be observed at 12 of the 45 fronts (see e.g. front 25 in Fig. 25).

While the vertical eddy flux generally resembles well the situation in idealized simulations, we note that the lateral eddy flux can substantially deviate from a constant vertical profile that was found in more idealized simulations (see Brüggemann and Eden, 2014) and predicted by linear stability analysis (Stone, 1966). Instead, we often find that the cross-front buoyancy fluxes are either further enhanced or diminished close to the surface while they are constant below (see Fig. 25). The reason for this might be time varying Ekman buoyancy fluxes that we do not distinguish from MLE fluxes in our analysis. This deviation also has consequences for the streamfunction which in some cases does not vanish at the surface.

Overall, we conclude that strong vertical buoyancy fluxes are present at all 45 fronts and in most cases we can as well identify a strong frontal overturning by MLEs (see Fig. 25). Comparing the eddy fluxes with idealized simulations and linear stability analysis, we find that the cross-front eddy fluxes show some differences, but the vertical eddy fluxes show quite a good agreement. Before, we discuss the amplitude of the eddy fluxes and their resemblance with idealized simulations and theoretic estimates, we will provide some more information regarding the synoptic forcing situation and difficulties in estimating the mixed layer base.

2.3.2 *Influence of realistic wind Forcing*

Wind and buoyancy fluxes influence the upper ocean stratification and hence have a potentially strong impact on the overturning circulation (Mahadevan, 2016; Gula et al., 2021). Since our study period is in winter, there a strong heat losses over our study area leading to surface cooling and static instabilities (not shown). Within the averaging time period of one week, significant variations in the wind direction and strength are observed, corresponding to the passage of low and high pressure systems across the study area, see e.g. snapshots of the mean sea level pressure over the North Atlantic in Fig. 16a and b. Short-term variations, such as wind bursts, occur on timescales of $\mathcal{O}$(hours). Despite these fluctuations, westerly winds prevail on average as can be seen in Fig. 16c. In order to assess the influence of the mean wind on the overturning circulation we compute the Ekman buoyancy flux (EBF), which is the rate of change in buoyancy induced by the cross-front Ekman flow (e.g. Gula et al., 2021)

$$\mathrm{EBF} = \frac{\boldsymbol{\tau} \times \mathbf{k}}{\rho_0 f} \cdot \nabla_h \overline{b} \tag{8}$$

with the wind stress $\boldsymbol{\tau}$ and the background density ρ_0.

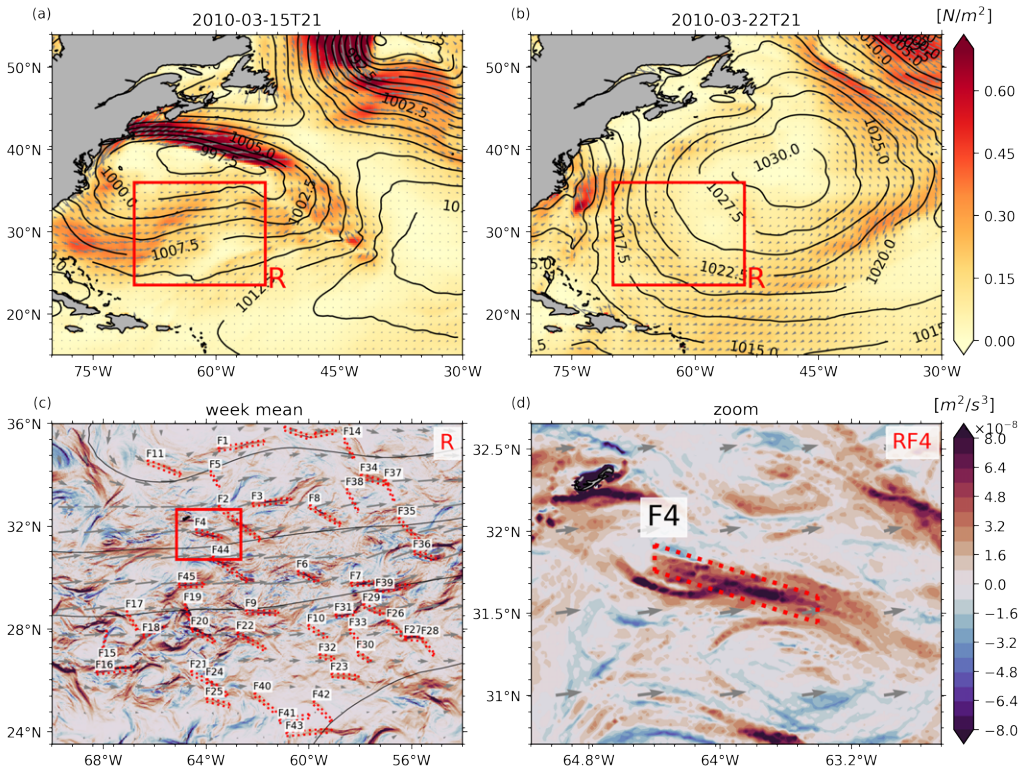

Figure 16: The forcing state over the North Atlantic: Snapshots of the low and high pressure systems crossing the study area. The magnitude (color) and the wind direction (arrows) of the wind stress are shown at the beginning (a) and end (b) of the averaging period. The isobars indicate mean sea level pressure. The lower figures show the mean Ekman buoyancy flux (see Eq. 8) over the study area (c) and at a single front (d).

Most fronts in the study area are oriented in north-west direction with lighter waters on their south-eastern side. Together with the mean westerly wind this implies a substantial down-front component of the wind field (see Fig. 16c,d) yielding an Ekman buoyancy flux across the front from its cold towards its warm side (note that the fronts hardly move during the seven day averaging period). These cross-front flows may induce gravitational instabilities and hence vertical convection, which destabilize the water column and counteract the MLE overturning circulation. Although, on average these buoyancy fluxes are 2-3 orders of magnitude weaker than their MLE buoyancy fluxes (see e.g. the lateral buoyancy flux in Fig. 15d). In addition to the cross-front flows, the predominant surface cooling might as well trigger convection and acts to destabilize the water column. However, frequent studies have shown that even in the presence of convection and also shortly after storms mixed layer instabilities show a rather persistent behavior (e.g. Gula et al., 2021; Chrysagi et al., 2021). Despite, the wind and surface buoyancy fluxes, we find that mixed layer instability remains the dominant process for the underlying fronts, and we find re-stratification at all those fronts (see Fig. 25).

2.3.3 *Estimation of the mixed layer depth*

An accurate estimate of the mixed layer depth is essential for estimating MLE processes since not only their spatial scale but also the horizontal and vertical MLE buoyancy fluxes depend on this scale (see Eq. (1) and Eqs. (10-11)). To identify the mixed layer depth, often an approach is chosen where the base of the mixed layer is identified as that depth where the density difference between the local depth and the surface density (Monterey and Levitus, 1997) or the density at 10 m (Kara et al., 2000) exceeds a certain threshold (see de Boyer Montégut, 2004; Holte et al., 2017, for a discussion of optimal thresholds and climatologies). Note that temperature thresholds are also commonly used (de Boyer Montégut, 2004), especially for observational data, but are less robust than density thresholds in regions with small temperature variations, such as the tropics. This approach works well in situations, where the mixed layer is nearly homogeneously mixed and where density increases rapidly below the mixed layer within the pycnocline. However, the approach becomes problematic in situations with less rigorous mixing and remaining vertical (but small) density gradients up to the surface, in cases of a double mixed layer, and in scenarios where strong temporal variations of mixed layer processes cannot be averaged out by long enough time averages. In such scenarios, the mixed layer depth estimated by this method strongly depends on the applied density threshold and globally defined thresholds can lead to misleading results in certain areas or times of the year.

When considering the vertical density stratification along a section through our study area (Fig. 17a), we note that the stratification is enhanced during a small band close to the surface and at around 600 m depth within the main pycnocline. When applying the commonly used density threshold of $\Delta\rho = 0.03\,\mathrm{kg\,m^{-3}}$, the upper-ocean band of enhanced stratification is detected as mixed layer base but not the top of the main thermocline. In contrast, a larger density criterion of $\Delta\rho = 0.2\,\mathrm{kg\,m^{-3}}$ reliably depicts the top of the main thermocline.

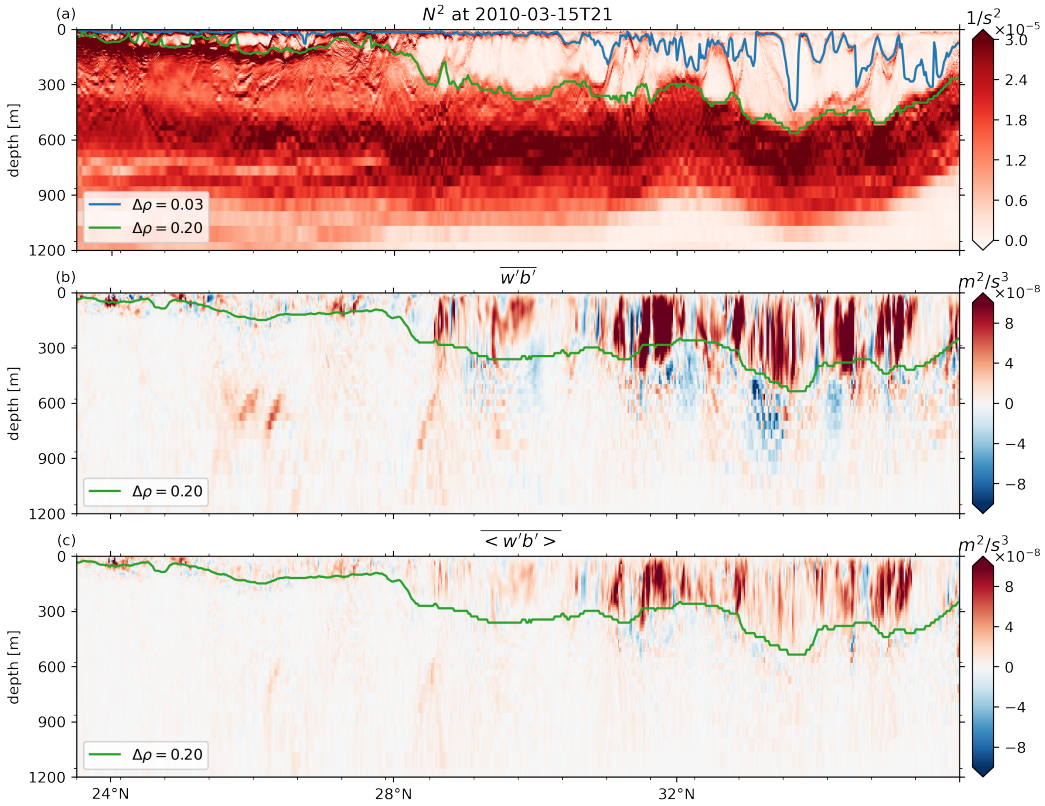

Figure 17: Section through the study area (see rectangular in Fig. 7) at 62°W: Snapshot of N^2 (a) and the vertical buoyancy fluxes, computed as fluctuations from the mean state, with the Reynolds mean defined by a time filter (b) and a spatial filter (c), as shown in Sec. 2.3. While the overline denotes a temporal mean, the angle brackets indicate a spatial mean. The mixed layer depths estimated with both threshold methods $\Delta\rho = 0.03\,\mathrm{kg\,m^{-3}}$ and $\Delta\rho = 0.2\,\mathrm{kg\,m^{-3}}$ are indicated as blue and green lines, respectively.

To assess which approach more accurately represents the vertical scale of MLEs, we compare both methods against the vertical MLE buoyancy fluxes derived using temporal and spatial filtering (see Fig. 17b and c). Our analysis reveals that in nearly all regions with enhanced vertical buoyancy fluxes, these fluxes consistently decay at the depth identified as the mixed layer base by the algorithm using the larger density threshold. Therefore, we will use the larger density threshold of $\Delta\rho = 0.2\,\mathrm{kg\,m^{-3}}$ in the following to determine the mixed layer depth and therewith the vertical scale of MLEs.

Note that a snapshot of a spatially filtered section $< w'b' >$ shows strong but noisy buoyancy fluxes clearly visible between the mixed layer and the seafloor (not shown). To reduce these fluctuations a subsequent additional time average is applied to the spatially filtered field $\overline{< w'b' >}$, see Fig. 17c. This highlights the importance of applying a temporal average to eliminate noise from fields derived using a spatial filter (see Fig. 17c). For a more detailed discussion of the eddy fluxes derived from both filters, refer to Sec. 2.6.

2.4 PARAMETERIZATION OF MIXED LAYER EDDIES

In the previous section, we showed how MLEs re-stratify ocean fronts by MLE overturning in ICON-SMT. Coarser model configurations that are e.g. used in coupled climate models are not able to resolve this MLE driven overturning. Consequently, they are biased in terms of mixed layer depth and the uptake and storage of heat and trace gases (Fox-Kemper et al., 2011). Here, parameterizations can be used to introduce missing MLE fluxes, leading to isopycnal slumping and re-stratification (Fox-Kemper et al., 2011). Two parameterizations are considered here: the parameterization proposed in Fox-Kemper et al. (2008) which is based on potential energy release (PER) and a parameterization based on ageostrophic linear stability analysis (ALS) as first introduced in Stone (1966). Evaluations with more realistic simulations were done by Uchida et al. (2022) who use a couple of relatively high-resolution simulations to estimate vertical MLE fluxes and to compare them with the parameterization of Fox-Kemper et al. (2008).

In this section, we investigate in more detail compared to previous studies how those two parameterizations perform when compared with a realistic submesoscale resolving ocean configuration like ICON-SMT. Therefore, we compare simulated and parameterized eddy fluxes in three different scenarios: (a) for dedicated fronts described in the previous section, (b) for non-frontal structures with enhanced horizontal buoyancy gradients, like eddies, and (c) across the entire domain. While (a) captures conditions for which the parameterizations are ultimately designed, namely baroclinic instability, (b) tests their robustness outside these ideal conditions, and (c) provides a comprehensive assessment that reflects realistic ocean model applications that need to represent frontal instabilities in both strong and weak density gradient regions.

The two parameterizations, PER and ALS, differ from each other by (1) a different dependency of a non-dimensional factor $\sqrt{1+Ri}$ and by (2) a different vertical structure function for the eddy fluxes, but they are equal regarding another important non-dimensional parameter $\alpha = M^2/f^2$ that indicates the frontal strength (see Brüggemann and Eden, 2014, for a more detailed discussion on the differences and similarities). Parameterizations for the submesoscale eddy fluxes based on ALS can be expressed as

$$\overline{\hat{v}'b'} = -\frac{8}{5} C_{als} \sqrt{1+Ri} \alpha^3 H^2 f^3 \tag{9}$$

$$\overline{w'b'} = C_{als} \mu_{als}(z) \frac{1}{\sqrt{1+Ri}} \alpha^2 H^2 f^3, \tag{10}$$

with tuning constant C_{als}, the mixed layer depth H, the lateral gradient $\alpha = \frac{M^2}{f^2}$ and a vertical structure function $\mu_{als} = -4\frac{z}{H}(\frac{z}{H}+1)$. For parameterizations based on PER the submesoscale eddy fluxes are given by

$$\overline{\hat{v}'b'} = -2 C_{per} \mu_{per}(z) Ri \alpha^3 H^2 f^3 \tag{11}$$

$$\overline{w'b'} = C_{per} \mu_{per}(z) \alpha^2 H^2 f^3, \tag{12}$$

with a tuning constant C_{per} and a vertical structure function $\mu_{per} = -4\frac{z}{H}(\frac{z}{H}+1)(1+\frac{5}{21}(2\frac{z}{H}+1)^2)$.

2.4.1 *Evaluation at individual fronts*

We begin with evaluating both parameterizations for the 45 fronts introduced in the previous section. Therefore, we apply in addition to the along- and across-front averages also a vertical average of the vertical and cross-front density gradients, N^2 and M^2, respectively, to estimate the averaged parameters Ri and α. These two parameters, together with the Coriolis parameter f and the mixed layer depth H, are then used to calculate the eddy fluxes and overturning rates using Eq. (10) for ALS and (11) for PER.

In Fig. 15, we depict one front that has a simple structure with a single mixed layer (Fig. 15a) and with relatively constant horizontal buoyancy gradients (Fig. 15b). For this front, diagnosed and parameterized eddy fluxes for the vertical eddy fluxes match quite well (see Fig. 15c; the tuning coefficients C_{als} and C_{per} used here are the same as discussed below). The maximum of the parameterized fluxes is slightly underestimated and the fluxes drop to zero at slightly too shallow depths. Despite that, there is quite some resemblance between parameterized and diagnosed eddy fluxes. Note that as mentioned by Fox-Kemper et al. (2008), the polynomial of order two assumed for the vertical structure function in ALS leads to a vertically constant rate of re-stratification and therefore cannot explain the maxima of N^2 at the top and base of the mixed layer that can be seen in Fig. 15a. Using a higher order polynomial for ALS could therefore be an essential step to improve the ALS parameterization.

For the lateral eddy fluxes, the situation is more complex. While ALS suggests a constant profile of the lateral fluxes (Stone, 1966), PER assumes a parabolic structure μ_{per} of the lateral eddy fluxes (Fox-Kemper et al., 2008). The idealized simulations carried out in Brüggemann and Eden (2014) rather favored a vertically constant profile. Also, our diagnostics for the front shown in Fig. 15 and for many other analyzed fronts (Fig. 25) suggest a rather constant profile throughout large parts of the mixed layer (see Fig. 15d). However, frequently the lateral fluxes are enhanced at the top of the mixed layer which might be a result of non-vanishing Ekman buoyancy fluxes.

The diagnosed overturning streamfunction depicted in Fig. 15e which vanishes at top and base of the mixed layer is well captured by both parameterizations. Note that the cross-front eddy flux has a substantial impact on the overturning streamfunction derived from Eq. (7) in both diagnostics and parameterization, since for this front but also most other fronts, we find that $\overline{\hat{v}'b'}N^2 \gg \overline{w'b'}M^2$. For ALS, this means that enhanced stratification at the top and at the bottom is required to bring the streamfunction to zero which is the case for the depicted front. Note that for some fronts, even the diagnosed streamfunction is intensified at the surface and has to vanish in a very thin boundary layer. In such cases, we also find an intense cross-front eddy flux probably associated with enhanced eddy buoyancy fluxes.

An important aspect for the evaluation of the MLE parameterization is the determination of the tuning coefficients C_{als} and C_{per} in Eqs. (9-10) and Eqs. (11-12), respectively. Here, we first determine the tuning coefficients separately for Ψ,

	C_{per}	E_{per}	C_{als}	E_{als}
ψ $[m^2/s]$	0.0409	2.83	0.289	2.71
$\overline{\hat{v}'b'}$ $[m^2/s^3]$	0.0518	2.22E-10	0.274	2.25E-10
$\overline{w'b'}$ $[m^2/s^3]$	0.0454	2.42E-16	0.274	3.54E-16

Table 1: Tuning coefficients C_{per} and C_{als} for ψ, $\overline{\hat{v}'b'}$, $\overline{w'b'}$ and mean errors E_{per} and E_{als} for PER and ALS. The coefficients are calculated using all 45 individual fronts shown in Fig. 13.

$\overline{w'b'}$ and $\overline{\hat{v}'b'}$ by minimizing the mean difference E between parameterized and simulated parameterizations or eddy buoyancy fluxes for all fronts:

$$E_\theta = \frac{1}{n}\sum_i^n (\theta^i_{diag} - \theta^i_{param})^2 \tag{13}$$

with θ being either $\theta = \overline{w'b'}, \overline{\hat{v}'b'}$, or ψ and where i runs over all $n = 45$ fronts. The derived coefficients are listed in Tab. 1.

We find similar coefficients for each parameterization no matter which variable is chosen for the tuning. For PER, we roughly estimate a value of $C_{per} = 0.04$, which is slightly below the range of $0.06 < C_{per} < 0.09$ that was found in Fox-Kemper et al. (2008) and Brüggemann and Eden (2014). For ALS, we obtain $C_{als} = 0.27$, which is about a third of the value obtained in Brüggemann and Eden (2014), but within the range $0.1 < C_{als} < 0.9$ estimated by Fox-Kemper et al. (2008). These coefficients are also used in Fig. 15 for scaling the profiles of the parameterizations. The remaining errors E_{per} and E_{als} in Tab. 1 give an impression about which parameterization can be more appropriately tuned. It turns out that there are no substantial differences between both parameterization with one exception: for $\overline{w'b'}$ the remaining error is nearly 1.7 times larger for the ALS parameterization compared to PER, meaning that the latter will on average more accurately reproduce the vertical eddy buoyancy flux $\overline{w'b'}$. In the following, we continue with the optimal tuning coefficients from $\overline{w'b'}$.

Using the derived optimal tuning coefficients for all fronts, we test the dependence of lateral and vertical eddy fluxes on α and Ri (Fig. 18a,b and c,d). Both parameterizations have an α^3-dependency for $\overline{\hat{v}'b'}$ and an α^2-dependency for $\overline{w'b'}$. The diagnosed slopes are somewhat smaller than those values (see Fig. 18a and b). Note, however, that the Richardson number also differs for each front and if the eddy fluxes have a dependency on Ri then there the theoretical slopes might not be obtained from this analysis. Therefore, we also show the predicted eddy fluxes of the ALS and PER parameterizations to assess their dependence on α. Here, we note that both parameterizations are not too far apart from each other and not too far apart from the diagnosed fluxes either. This indicates that the predicted α-dependency of the parameterizations is relatively well-matched. For more details on the α-dependency see Sec. 2.4.3.

The Richardson number dependence is harder to evaluate due to significant scatter, which impacts the reliability of the regression (see Fig. 18c and d). We suspect this scatter arises from (1) the influence of other physical phenomena, such

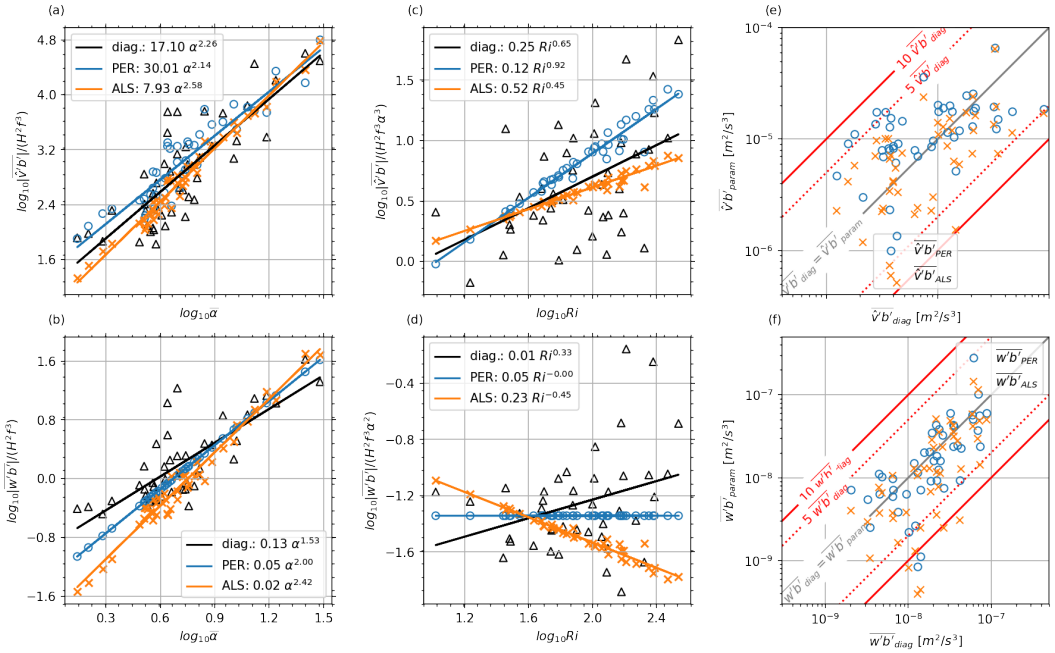

Figure 18: The figure shows the dependence of the eddy fluxes on $\overline{\alpha}$ (a and b) and Ri (c and d), as well as the parameterization bias (e and f). The top row shows lateral (cross-front) buoyancy fluxes, while the bottom row shows vertical buoyancy fluxes. Regression coefficients for sub-figures (a-d) are given in the legend. Also note the different scalings on the ordinate. In figures (e-f), points in the lower right triangle indicate underestimation of the eddy fluxes by the parameterizations, while points in the upper left triangle indicate overestimation. Red solid lines indicate a factor of ten deviation between diagnosed and parameterized eddy fluxes, and red dashed lines indicate a factor of five deviation. As tuning coefficients for C_{per} and C_{als} we used the values based on $\overline{w'b'}$ from Tab. 1.

as surface currents, eddies, or Ekman pumping, and/or (2) imprecise frontal definitions, e.g., averaging along meandering fronts or including non-frontal regions with weak gradients and large Ri values (see Fig. 14). However, we also want to note that the Ri-dependency is smaller (no Ri-dependency for PER and only mildly square-root dependency for ALS). Therefore, the range of scaled eddy fluxes is smaller (note the different scalings on the ordinate of Fig. 18a-d). Overall, it is apparent that PER seems to slightly better match the diagnosed eddy fluxes $\overline{\hat{v}'b'}$ and $\overline{w'b'}$ compared with ALS.

An estimate about the spread between diagnosed and parameterized eddy fluxes can be obtained from Fig. 18e and f. Values close to the diagonal indicate good agreement between diagnosed and parameterized fluxes. The predicted eddy fluxes are scattered around their diagnosed counterparts but hardly ever deviate by more than a factor of ten and often even less than a factor of two for eddy fluxes that vary over two orders of magnitude. This indicates that both parameterizations appear to have reasonable skill to reproduce the diagnosed eddy fluxes.

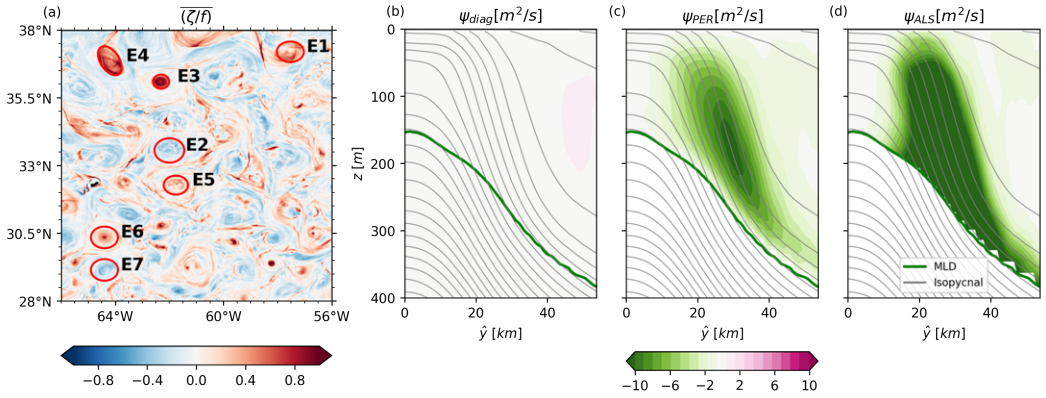

Figure 19: (a) Seven-day average of the Rossby number at 50 m depth where the red shading indicates cyclones and blue shading indicates anticyclones. We arbitrarily depicted seven eddies for our analysis from observing time averages of vorticity and lateral density gradients and determined the respective eddy rims based on the location of the strongest lateral buoyancy gradient. The latter is indicated by red circles. Panels b-d show perimeter averages of the diagnosed overturning streamfunction (b), the PER parameterization (c) and the ALS parameterization (d) for eddy E3. Note that a negative streamfunction value indicates a counterclockwise circulation. Isopycnals are indicated by gray lines and the mixed layer depth based on the density criterion with $\Delta\rho = 0.2\,\mathrm{kg\,m^{-3}}$ is indicated by green lines. Note that the core of the eddy is at $R = 0$. The eddy rim can be inferred from the strong lateral buoyancy gradient and is roughly at 30 km. The tuning coefficients for the lateral buoyancy flux in Tab. 1 are used to compute the overturning rates for the parameterizations in c and d.

2.4.2 *Evaluation at individual mesoscale eddies*

Strong lateral buoyancy gradients are not restricted to mesoscale fronts, as they also occur at the edges of mesoscale ocean eddies. In this section, we investigate whether submesoscale eddies form at the rim of these eddies, potentially driving overturning, and evaluate how well parameterizations capture this process in the context of ocean eddies. We analyze seven eddies, five cyclones and two anticyclones (as shown in Fig. 19a), and evaluate eddy overturning using the same approach applied to ocean fronts (Sec. 2.3.1).

To obtain the overturning of the buoyancy front at the eddy rim, we chose an elliptical coordinate system where we map all model points of the eddy to 70 ellipses with different radii that provide the across-front coordinate $\hat{y}$. Half of the ellipses were inside and half are outside the eddy rim. The eddy rim was chosen based on the location of the strongest lateral buoyancy gradient, a change in the sign of the vorticity, a significant variation in stratification, and in some cases weak Richardson numbers (not shown). It is denoted by the red ellipses in Fig. 19. All quantities are then averaged along the ellipses (providing the along-front coordinate $\hat{x}$). The perimeters of the depicted eddies range from about 240 km to 300 km and are thus long enough for mixed layer instabilities to grow on (compare with the length scale of the fastest growing mode Fig. 9) and to be resolved by ICON-SMT.

We present the resulting eddy fluxes for eddy E3, which shows only very weak overturning rates (Fig.19b). In contrast, both parameterizations significantly overes-

timate the eddy overturning, predicting an overturning cell that tends to re-stratify the frontal structures at the eddy rim (see Fig.19c and d). The weak overturning observed at the eddy rim is unexpected, as the enhanced density gradients, low stratification, and low Richardson numbers would typically favor the development of a submesoscale eddy field.

For three other eddies (E1, E2, E4), we observe strong vertical eddy fluxes and low Richardson numbers, consistent with the findings of Brannigan et al. (2017) and Marez et al. (2020b), who reported intense submesoscale overturning in cyclones. However, even in these cases, we do not clearly identify strong fluxes aligned with tilted isopycnals; instead, the fluxes appear to be largely independent of the mean background stratification. For the remaining eddies (E5, E6, E7), we detect only very weak overturning rates, accompanied by similarly weak parameterized overturning rates. In contrast to the other eddies, these have weaker 'unstable front' characteristics, insufficient to drive strong eddy fluxes, according to both diagnostics and parameterizations.

Note that eddies (E1, E3, E4) were selected even though they are outside the study area near the Gulf Stream meander because they have much higher velocities along the eddy perimeter. The eddy E4 for instance just forms from a mesoscale front that merges into a strongly meandering eddy and can thus be regarded as a 'young' eddy, which is also accompanied by strong vertical buoyancy fluxes. In contrast, E3 shows surprisingly weak eddy fluxes (see above) but strikingly strong symmetries that are not related to frontal meanders or external interactions, suggesting that it is an 'old' eddy. Investigating how vertical buoyancy fluxes at the eddy rim evolves with eddy age could be a focus for future studies.

Overall, the eddies appear to encounter less re-stratification along the eddy rim than the parameterizations suggest with much smaller diagnosed compared to parameterized overturning rates. Consequently, implementing MLE parameterizations in eddy-resolving ocean models may interfere too strongly with the ocean eddy field, likely by overly damping eddies.

2.4.3 *Evaluation in the entire domain*

Evaluations for individual fronts and eddies, as we have done in the previous sections, are not feasible during the runtime of a numerical model. To assess how well PER and ALS capture the situation for general flow situations, we apply a different procedure that does not only consider individual fronts but evaluates the entire study area (see the red rectangle in Fig. 13). This means that not only frontal regions and mesoscale eddies are included in the evaluation, but also regions with weak lateral density gradients. This implies that the Richardson number strongly varies across the domain with small values of Ri-numbers at the center of fronts and much larger Ri-numbers in non-frontal areas (see Fig. 14).

We apply two distinct techniques, (1) a one-week time filter and (2) a 30 km spatial filter to isolating the higher frequent submesoscale motions from the ambient circulation and the mesoscale eddy field (for details see Sec. 2.3.1). The submesoscale eddy fluxes outside frontal areas are typically much smaller than those within frontal areas.

To facilitate the evaluation, we project the horizontal eddy fluxes onto the local buoyancy gradient to obtain something like a cross-front buoyancy flux (in cases without a particular front, this is just like an along-gradient flux, but we will stick with the term 'cross-front' to indicate the similarity with the previous discussions).

$$\overline{\hat{v}'b'} := \frac{1}{|\nabla_h \overline{b}|} \begin{pmatrix} \overline{u'b'} \\ \overline{v'b'} \end{pmatrix} \cdot \begin{pmatrix} \frac{\partial \overline{b}}{\partial_x} \\ \frac{\partial \overline{b}}{\partial_y} \end{pmatrix} . \tag{14}$$

The sign convention here defines positive cross-front buoyancy fluxes as upgradient and negative fluxes as downgradient. Our focus is on the downgradient components of the buoyancy fluxes (the negative projected buoyancy flux and the positive vertical buoyancy flux), which represent the components of the eddy fluxes that act to flatten the isopycnals. Buoyancy fluxes which are not downgradient are masked from the field.

For a local evaluation, we calculate eddy quantities as fluctuations from a time mean and alternatively from a spatial mean at any given grid point in the domain. Furthermore, we average the eddy fluxes vertically within the mixed layer (remaining negative vertical eddy fluxes are masked). We then group all pairs of time mean Ri and α into bins of similar Ri and α and compute the mean eddy fluxes and the corresponding standard deviation for each Ri or α bin.

Two different Ri-number regimes are apparent from Fig. 20, the first for approximately $Ri \leqslant 8$ and the second for $Ri \geqslant 8$. In both regimes, we observe an almost linear dependence for the lateral and vertical eddy flux in the double logarithmic scaling with a slope differing for each regime. Note that in this diagram, values of $Ri \leqslant 8$ rather correspond to frontal areas (see Fig. 13e) while larger Ri-numbers correspond to regions of the ambient flow and mesoscale eddy field.

Parameterized eddy fluxes can now be derived as before following Eq. (11) and (12) for PER and Eq. (9) and (10) for ALS from the time averaged horizontal and vertical stratification at each single grid point. The scaling coefficients for cross-front and vertical eddy fluxes are calculated at each location, with the median used to derive the final tuning coefficients (Tab. 2). We applied this optimization process for the entire domain (not shown) and for a subset of the domain, where we only kept points with $Ri < 8$ for optimization process. Since, the latter is closer to our previous evaluation, we will discuss this scaling in the following.

In Fig. 20, a linear regression is shown for both Ri regimes. We diagnose in the small Ri regime a slope of $a_1 = 0.58$ for the cross-front buoyancy flux, which is closer to that from ALS of 0.5 compared with that from PER of 1. For the vertical eddy flux (Fig. 20b), we determine a negative slope of $a_1 = -0.31$ in the small Ri regime, which again is slightly closer to -0.5 (ALS) than to 0 (PER).

Repeating the evaluation using a two-day instead of a one-week time window for the Reynolds decomposition shifts the small Ri number regime to smaller Ri numbers, since the Ri number increases when temporal averaging is applied (see also discussion above). With the same Ri threshold, this would lead to steeper cross-frontal eddy fluxes ($a_1 = 0.96$) and weaker slopes ($a_1 = -0.02$) for the vertical eddy fluxes, which are then more consistent with PER than ALS. However, using a smaller Ri threshold (e.g. $Ri \leqslant 4$) results in eddy flux dependencies that are more consistent with previous results for a one-week time window (see above).

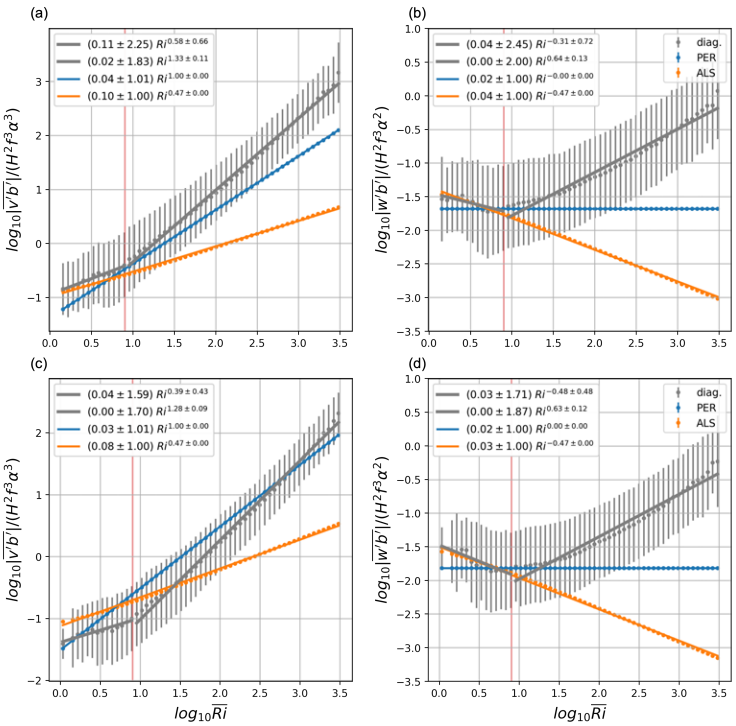

Figure 20: The dependence of the lateral (left) and vertical (right) eddy flux on the local Ri number, derived using a temporal (upper) and a spatial (lower) filter to compute the eddy fluxes. The colored lines resemble the Richardson number dependencies of ALS (orange) and PER (blue) given in Eqs. (9-12). Data from the entire regional field are binned and presented as means (gray dots) with error bars computed from bin-stds (gray lines). Linear regression is applied for a small $Ri < 8$ and a large $Ri > 8$ Ri regime. The tuning coefficients for $\overline{w'b'}$ in Tab. 2 are used.

A filter with an averaging window of two days most likely filters too much of the submesoscale eddy fluxes, however we mention it here to provide an assessment on the sensitivity of our results. We also applied the evaluation of the parameterizations within a larger region of the North Atlantic ($80-55°$W, $23-38°$N) but the results were hardly different (not shown).

Using a spatial instead of a temporal filter to calculate eddy fluxes has little impact on their dependence on Ri (see Fig. 20c,d). However, we observe a shift of the diagnosed lateral buoyancy fluxes towards smaller values. The vertical buoyancy fluxes, in contrast, only show a minor shift (see Sec. 2.6 for a comparison of the eddy fluxes). This affects the tuning coefficients, which are up to a factor of two smaller for $\overline{w'b'}$ and up to a factor of five smaller for $\overline{\hat{v}'b'}$.

Uchida et al. (2022) evaluated $\overline{w'b'}$ from PER by testing both, a constant and a time dependent tuning coefficient in a region that focuses on the Gulf Stream front. They determined eddy fluxes from spatial filtering as we did here. Their study revealed substantial variability in tuning coefficients across models ranging from 0.02 to 0.2. We repeated their analysis in their domain and also in our study area (results for our study area are shown in Fig. 26) and we found large differences of the tuning coefficients depending on the chosen domain. For more details about the variability of tuning coefficients with their approach see Sec. 2.6.

	C_{per}	C_{als}	filter	Ri threshold
$\overline{\hat{v}'b'}$ $[m^2/s^3]$	0.0263	0.0698	time	$Ri < 8$
$\overline{w'b'}$ $[m^2/s^3]$	0.0208	0.0530	time	$Ri < 8$
$\overline{\hat{v}'b'}$ $[m^2/s^3]$	0.0456	0.5829	time	–
$\overline{w'b'}$ $[m^2/s^3]$	0.0697	0.6846	time	–
$\overline{\hat{v}'b'}$ $[m^2/s^3]$	0.0069	0.0178	space	$Ri < 8$
$\overline{w'b'}$ $[m^2/s^3]$	0.0153	0.0386	space	$Ri < 8$
$\overline{\hat{v}'b'}$ $[m^2/s^3]$	0.0086	0.1116	space	–
$\overline{w'b'}$ $[m^2/s^3]$	0.0419	0.4123	space	–

Table 2: Table of tuning coefficients C_{per} and C_{als} for lateral and vertical buoyancy fluxes. The first block uses a temporal filter for eddy flux computation, while the second employs a spatial filter. Optimal coefficients are provided for the 'small' Ri regime and the full domain as a reference.

The mean magnitude of the parameterized eddy fluxes is modulated by the tuning coefficients. Considering the small Ri regime, the tuning of ALS indicates a more appropriate tuning than PER. However, this seems to come at the cost of a more variable tuning coefficient (see differences between Ri-masked and full domain in Tab. 2).

To assess if both parameterizations show the correct dependence on α, we now bin all points according to similar α values. Then, we apply a linear regression to the logarithmically scaled eddy fluxes averaged within each bin and the logarithmic α parameter (see Fig. 21. The averaged eddy fluxes in the linear regression are weighted by the standard deviation of the eddy fluxes in each bin). We furthermore scale the eddy fluxes by all parameters except of α such that the slope of the regression line provides information about the exponential dependence of the eddy fluxes on α. Since PER and ALS suggest a different dependence on Ri, we scale the eddy fluxes twice for each of the respective Ri-dependency (Fig. 21a and b for PER and Fig. 21c and d for ALS). For a correct dependency of the parameterizations on α and Ri, the slope of the regression line should be three for $\overline{\hat{v}'b'}$ and two for $\overline{w'b'}$ for both, ALS and PER. We find that the slope for PER is indeed close to three for $\overline{\hat{v}'b'}$ and close to two for $\overline{w'b'}$ while for ALS there is a larger discrepancy of 2.5 for $\overline{\hat{v}'b'}$ and 1.4 for $\overline{w'b'}$.

Since we observe differences of the Ri-dependency in the small and large Ri-regimes (where regime shift occurred close to $Ri = 8$), we also investigate how the results change once we filter regions with larger Richardson numbers that are not associated with frontal structures. Here, we observe that slopes become smaller if less points are filtered. For PER, this means that the predicted slopes do not match the theoretical ones that well anymore for any Ri-restriction. For ALS, in contrast, we find an optimum once only points of $Ri < 50$ are taken into account. Here, the predicted slopes of ALS and the theoretical slopes are nearly identical. This analysis confirms our results from above that ALS better reproduces eddy fluxes in regions with lower Richardson number. If only those values are considered,

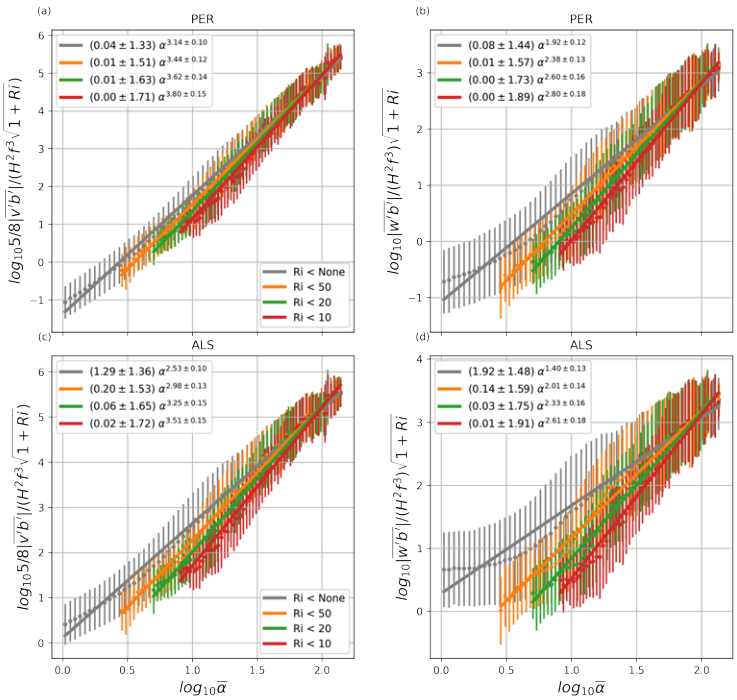

Figure 21: The dependence of the lateral (left) and vertical (right) eddy flux on the cross-frontal buoyancy gradient $\overline{\alpha}$ for PER (upper) and ALS (lower). The evaluation is repeated where points of the domain are filtered according to different thresholds of Ri (see legend). The tuning coefficients for $\overline{w'b'}$ in Tab. 2 are used. Note that here high Ri go along low α and thus filtering high Ri also effectively filters small α.

the agreement is even stronger than for PER. If in contrast the entire domain is considered, PER seems to better reproduce the diagnosed eddy fluxes.

2.5 SUMMARY AND CONCLUSION

In this study, we investigated the frontal overturning of mixed layer eddies (MLEs) in a new configuration of ICON-o (SubMesoscale Telescope configuration referred to as ICON-SMT) that permits the simulation of submesoscale eddies in the North Atlantic. In contrast to more idealized configurations which have been extensively used to study frontal overturning (Haine and Marshall, 1998; Boccaletti et al., 2007; Fox-Kemper et al., 2008; Mahadevan, 2016; Brüggemann and Eden, 2014), the submesoscale dynamics that we study are subject to the combination of realistic wind forcing, diabatic mixing and a vibrant background flow field (see Sec. 2.2). We study submesoscale dynamics with a spatial resolution of less than 1 km that is similar but slightly higher compared the model simulations applied in Uchida et al. (2022). To which degree this slightly higher resolution is critical is unclear and probably model dependent. For ICON it was shown that a horizontal resolution below 2.5 km is essential to resolve submesoscale dynamics in our study area (Hohenegger et al., 2023).

We demonstrate that the spectral sea surface height and temperature distributions in ICON-SMT resemble those of state-of-the-art satellite observations (includ-

ing those from the novel SWOT mission, see Sec. 2.2.2.3). The variability of sea surface height and temperature is therefore far better matched on high and on intermediate scales compared to an ICON reference simulation with only 10 km resolution.

The main focus of this study is to investigate frontal overturning by MLEs. Therefore, we study submesoscale eddy fluxes at dedicated fronts and eddies with high lateral buoyancy gradients but also in the entire domain that includes situations with weaker lateral gradients. For each of 45 selected fronts, we identify intense submesoscale eddy fluxes and frontal overturning re-stratifying the fronts. Therefore, we can demonstrate that frontal overturning can be identified in realistic ocean configurations under the influence of surface wind and buoyancy fluxes and in the presence of a vibrant mesoscale eddy field. We find that the submesoscale eddy fluxes observed here act similarly as suggested by more idealized simulations (Sec. 2.3). We also discuss some complications that naturally in realistic configurations as studied here. Those include e.g. the presence of surface Ekman buoyancy fluxes, sensitives of the analysis with respect to the depicted spatial and temporal averaging, and the determination of the mixed layer depth.

One important finding of this study is that the vertical scale of MLEs cannot be obtained from the mixed layer depth simply determined by the commonly used density difference algorithm with a threshold of $\Delta\rho = 0.03\,\mathrm{kg\,m^{-3}}$. Instead, we first assess the vertical scale of MLEs by determining where the vertical eddy buoyancy fluxes vanish then we tune the density threshold to the more than ten times larger value of $\Delta\rho = 0.2\,\mathrm{kg\,m^{-3}}$ for which the mixed layer depth fits best to the vertical MLE scale. We find that for our study area and study period, the enhanced threshold leads to a more appropriate identification of the main thermocline, and it avoids that enhanced density gradients as part of a double mixed layer are depicted as mixed layer base. We do not claim that the enhanced threshold found here should be considered as a universal value, but we rather want to raise the attention that a careful examination of the mixed layer base is required in order to associate it with the vertical MLE scale.

Since climate models are still not able to resolve submesoscale eddies and since they will not be able to do so in the near future, we also examined how well parameterizations for submesoscale baroclinic instability are able to capture the detected MLE fluxes. To this end, we diagnosed the vertical and horizontal density gradients at 45 mixed layer fronts to derive parameterized eddy fluxes from two different parameterizations. The first parameterization, ALS, is based on linear stability analysis following Stone (1966) and the second, PER, is based on a potential energy release following Fox-Kemper et al. (2008). Both parameterizations differ in their dependence on the Richardson number: $\overline{\hat{v}'b'} \propto \sqrt{1+\mathrm{Ri}}$, $\overline{w'b'} \propto \sqrt{1+\mathrm{Ri}}^{-1}$ (ALS) and $\overline{\hat{v}'b'} \propto \mathrm{Ri}^{1}$, $\overline{w'b'} \propto \mathrm{Ri}^{0}$ (PER). They also differ regarding the vertical profile of the cross-front buoyancy fluxes. Here, PER suggests a parabolic shape and ALS suggests a vertically constant flux. However, both parameterizations have the same dependency on a parameter $\alpha = M^2/f^2$ (e.g. Brüggemann and Eden, 2014) that is a non-dimensional coefficient determining the strength of the buoyancy front.

Overall, we find that both parameterizations capture the essential features of the overturning process at the depicted fronts and correctly determine the order of magnitude of the diagnosed fluxes. The major reason for the similarity

of both parameterizations is that they both predict the same dependency of the eddy fluxes on α. Since the α-dependency involves a larger exponent compared to the Ri-dependency, the eddy fluxes are more sensible regarding variations of α. Our analysis shows that this dependency on α is relatively well-matched. Therefore, both parameterizations predict the diagnosed eddy fluxes in general relatively well.

However, differences of both parameterizations regarding their Ri-dependency also leads to differences of the performance of both parameterizations. Overall, we conclude that PER better captures the diagnosed fluxes if all points of the domain are taken into account. Once, however, the domain is filtered by selecting only regions with smaller Richardson number, the performance of ALS substantially increases and becomes even better than that of PER. We also find that the vertical profile of the lateral eddy fluxes is rather constant over large parts of the mixed layer and is therefore better matched by ALS.

In non-frontal regions, such as eddies, both parameterizations sometimes overestimate the MLE fluxes (see Sec. 2.4.2), despite that the length of the perimeter and the size of the eddies would allow for the development of submesoscale eddy fluxes and ICON-SMT to resolve them. Identifying the driving mechanism of this discrepancy remains a topic for future investigation.

Overall, we can summarize the following main conclusions of this study:

- ICON-SMT with a resolution of less than 1 km over large parts of the North Atlantic can successfully simulate mixed layer submesoscale eddies.
- Once submesoscale processes are resolved in ocean models, there is an increase of the variability not only on the kilometer scale of submesoscale eddies but also on larger scales. The enhanced variability is in better agreement with observations from established and novel satellite missions compared with a coarser model configuration.
- Once submesoscale processes are resolved, submesoscale eddies lead to overturning of ocean fronts, re-stratifying these fronts and providing a downward buoyancy flux.
- The depth scale of MLEs is not matched by the mixed layer depth identified from simple density criteria (de Boyer Montégut, 2004) if a frequently used density threshold is used. Once the threshold is adjusted, however, the method can successfully estimate the vertical extent of MLE fluxes. It remains to be shown, if the adjustment applied here is universal or if other regions or seasons require different thresholds as well.
- MLE fluxes determined from time filtering are qualitatively similar compared to those obtained from a spatial filter. However, the latter are systematically smaller in magnitude which points to more carefully depicting the spatial filter length scale.
- Parameterizations for MLEs can capture the effect of the mixed layer overturning within an accuracy that lies within an order of magnitude.
- Both parameterizations differ with regard to a dependency on the non-dimensional Richardson number. If the entire Richardson regime is considered,

PER seems to better match the diagnosed dependence. For the low Richardson regime, in contrast, ALS seems to better match the Richardson dependence.

- PER uses a higher order polynomial as structure function for the vertical eddy fluxes. This appears to be more appropriate than the structure function suggested by Stone (1966) and used for ALS since the former suggests strong re-stratification at the mixed layer top and bottom – a feature that we frequently observe at many ocean fronts.
- The vertical profile of the cross-front eddy fluxes, in contrast, appears to be closer matched by the profile suggested in ALS. Nevertheless, we note that the diagnosed eddy fluxes often show deviations from the constant structure, potentially caused by Ekman buoyancy fluxes.
- The strength of the eddy fluxes in both parameterizations is strongly determined by the non-dimensional parameter α. Here, both parameterizations have the same dependency and we note that this dependency is well matched once we compare parameterized and diagnosed eddy buoyancy fluxes.

Realistic model simulations of kilometer-scale resolution will become more and more frequent in the future. Our study showed that those simulations are superior in producing small-scale variability compared with simulations applying spatial resolutions of O(10 km) (the so-called eddy resolving configurations). Furthermore, we show in this study that such simulations are well able to capture submesoscale eddies and the associated overturning at upper-ocean density fronts. They will therefore become a powerful tool to study submesoscale processes under realistic conditions for a variety of applications.

Although the availability of submesoscale resolving simulations will increase, there will also still be the requirement for submesoscale eddy parameterizations, in particular in coupled climate models. We demonstrated that submesoscale eddy resolving simulations like ICON-SMT can identify where existing parameterizations are successful and where they might require improvements.

ACKNOWLEDGMENTS. This work was founded by the German Research Foundation (DFG project number 274762653) and is part of the subproject "L4: Energy-Consistent Ocean-Atmosphere Coupling" of the collaborative research center TRR-181 "Energy Transfer in Atmosphere and Ocean". This work used resources of the Deutsches Klimarechenzentrum (DKRZ) granted by its Scientific Steering Committee (WLA) under project ID bm1102. We would also like to thank Leonidas Linardakis for running the numerical simulation and Jin-Song von Storch for providing valuable feedback.

DATA AVAILABILITY STATEMENT. The ICON model code is available through the ICON GitLab repository: https://gitlab.dkrz.de/icon/icon-model. ICON is distributed under a BSD 3-clause license, allowing its use, modification, and distribution with appropriate attribution.

2.6 APPENDIX A

MODEL VALIDATION

Spinup bias in SST

The correct position of the Gulf Stream and the location where it separates from the coast is a frequent bias in ocean models. Here, we briefly discuss the SST bias of ICON-SMT by comparing a monthly mean of simulated SST with observational data from Modis-Aqua satellite (see Fig. 22). Since mesoscale features do not averaged out within a month, an evaluation of this time period implies locally larger biases. We note that the Gulf Stream detaches to far north, which leads to a warm bias northern and to a cold bias southern from the mesoscale Gulf Stream front. Such biases lead to strong non-physical sensible heat fluxes since the these fluxes depend on the ocean-atmosphere temperature difference. However, a similar bias is commonly observed in other high resolution models, see e.g. Chassignet and Marshall (2008). Note that the bias is comparatively small in our study area which is slightly south of the Gulf Stream and North Atlantic Current front (see rectangular in Fig.7). Note further that this bias is inherited from the coarser model spinup since the integration time of a couple of weeks of ICON-SMT is too short for any major adjustment of that bias.

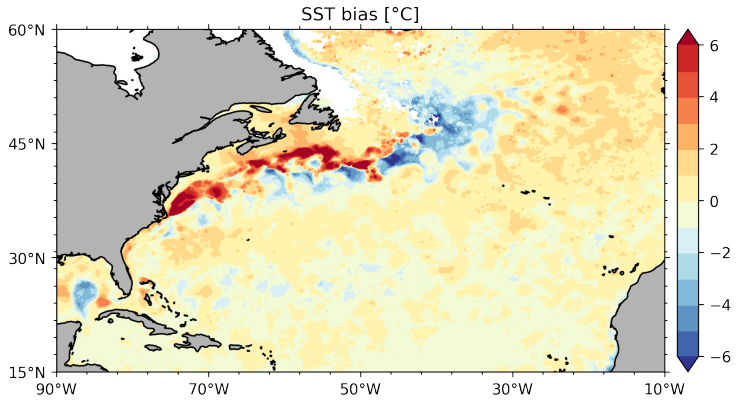

Figure 22: The SST bias between the SMT-Model and the Modis-Aqua Satellite product $T_{ICON-SMT} - T_{Modis-Aqua}$. Here the monthly mean of March 2010 is evaluated on a 0.1° regular grid.

APPENDIX B

DIAGNOSING EDDY FLUXES

Eddy fluxes derived using spatial and temporal filtering

This section compares eddy fluxes derived from spatial filters with those derived from temporal filters. In both methods, the filter is used to define a mean quantity $\bar{\phi}$ that is used to derive a fluctuating or eddy quantity by $\phi' = \phi - \bar{\phi}$. For

the temporal filter, we use one week and for the spatial filter a length scale of 30 km. For consistency when comparing both methods, we average the spatially filtered fluxes over a week, and we smooth the temporally filtered fluxes with the same spatial filter. Figure 23a and b show stronger vertical buoyancy fluxes with temporal filtering (see also the sections in Fig. 17b and c). A direct comparison of the correlation of both fluxes (Fig. 23c) confirms that temporal filtering consistently leads to stronger fluxes. However, it also shows a good correlation between both methods indicating that either could be used to estimate eddy fluxes once appropriate scaling coefficients are depicted.

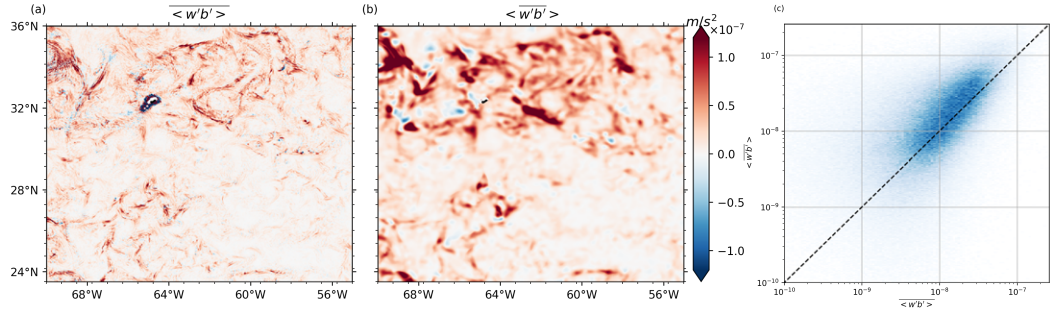

Figure 23: The vertical buoyancy flux calculated with a spatial (a) and temporal (b) filter. For comparison, the field (a) is additionally averaged over the entire week, and the field in (b) is spatially averaged. Both fields are averaged over the mixed layer. The correlation of both eddy fluxes is given in (c).

Choice of overturning stream function

Fox-Kemper et al. (2008) suggest using the Held-Schneider streamfunction $\psi = \overline{w'b'}/M^2$ that is based on the vertical eddy fluxes following Held and Schneider (1999) to describe MLE overturning instead of Eq. (7). However, we find that this version can become problematic in realistic model applications with strongly varying isopycnal slopes. In regions with vanishing lateral density gradients, the Held-Schneider streamfunction can take very large values that require compensation by residual fluxes (**Plumb2005**). Specifically, in 'non-frontal' regions M^2 tends to decrease more rapidly than $\overline{w'b'}$, resulting in an undefined streamfunction (see Fig. 24). An alternative formulation, following Andrews and McIntyre (1976), defines the streamfunction as $\psi = \overline{\hat{v}'b'}/N^2$. This form also becomes undefined when $N^2 = 0$, a situation that is likely to occur within the mixed layer. Interestingly, we rarely find occasions of vanish N^2 at ocean fronts when considering time-averaged fields, probably as a consequence of submesoscale eddy re-stratification (see Fig. 24). To avoid these complications of vanishing lateral or vertical gradients, we decided to use the full streamfunction as defined in Eq. (7) but we would like to note that this streamfunction is often determined by the cross-front eddy fluxes and therefore resembles that of Andrews and McIntyre (1976).

In Fig. 15, we show horizontal averages of key parameters, eddy fluxes and overturning streamfunction for one of the 45 selected fronts that are used for evaluating parameterizations. While this front is similar to many other fronts, there are also some fronts that behave rather similar. In Fig. 25, we show the same horizontal aver-

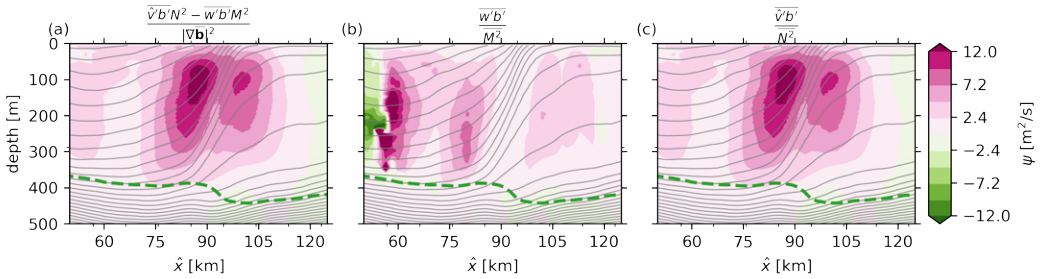

Figure 24: Comparison of streamfunction formulations applied to diagnosed fields of front F1: the 'full' formulation following Andrews and McIntyre (1978) (a), the formulation by Held and Schneider (1999) (b), and the formulation following Andrews and McIntyre (1976) (c).

ages as in Fig. 15 but this time for all 45 fronts. A notable difference from idealized studies is that we observe a surface intensification of the cross-front eddy flux for most of the fronts. This cross front flux can presumably be associated with Ekman buoyancy fluxes. Furthermore, we also frequently observe fronts where strongly varying vertical stratification. For some fronts this results in arguably mixed layer depth determinations even with the adjusted threshold. However, these latter cases remain the exception.

APPENDIX C

PARAMETERIZATIONS OF MIXED LAYER EDDY FLUXES

Comparison to recent MLE evaluation

In this section we apply the methodology of Uchida et al. (2022) to our simulation (around the Gulf Stream separation region) and extend it to include ALS. Figure 26 shows the diagnosed and parameterized spatial median vertical eddy fluxes, along with parameterized fluxes and time-dependent tuning coefficients. Both parameterizations capture the median vertical eddy flux, with PER showing slightly better agreement than ALS. Compared to the models in Uchida et al. (2022) (their Fig. 6), ICON-SMT produces diagnosed vertical eddy fluxes about an order of magnitude stronger than most models (5 out of 7), but in closer agreement with two of the higher-resolved models, namely, LLC4320 and FIO-COM32.

The tuning coefficients for vertical eddy fluxes (Tab. 3) differ by an order of magnitude to those in Uchida et al., 2022 (note that Uchida et al. (2022) investigate a domain slightly north-west to ours which encloses large parts of the Gulf Stream, where the MLE fluxes are substantially stronger than in our domain but probably also contaminated by mesoscale eddy fluxes). Furthermore, these coefficients deviate significantly from those derived in the previous section (especially when time filters are applied) and from values reported in earlier studies (e.g. Fox-Kemper et al., 2008; Brüggemann and Eden, 2015).

In this analysis, we use the MLD diagnosed with $\Delta\rho = 0.2\,\mathrm{kg\,m^{-3}}$, identified to represent the effective vertical extent of MLE fluxes (see Sec. 2.3.3). Using the common smaller threshold of $\Delta\rho = 0.03\,\mathrm{kg\,m^{-3}}$ produces fluxes with a similar


F1
F2
F3
F4
F5
F6
F7
F8
F9
F10
F11
F12
F13
F14
F15
F16
F17
F18
F19
F20
F21
F22
F23
F24

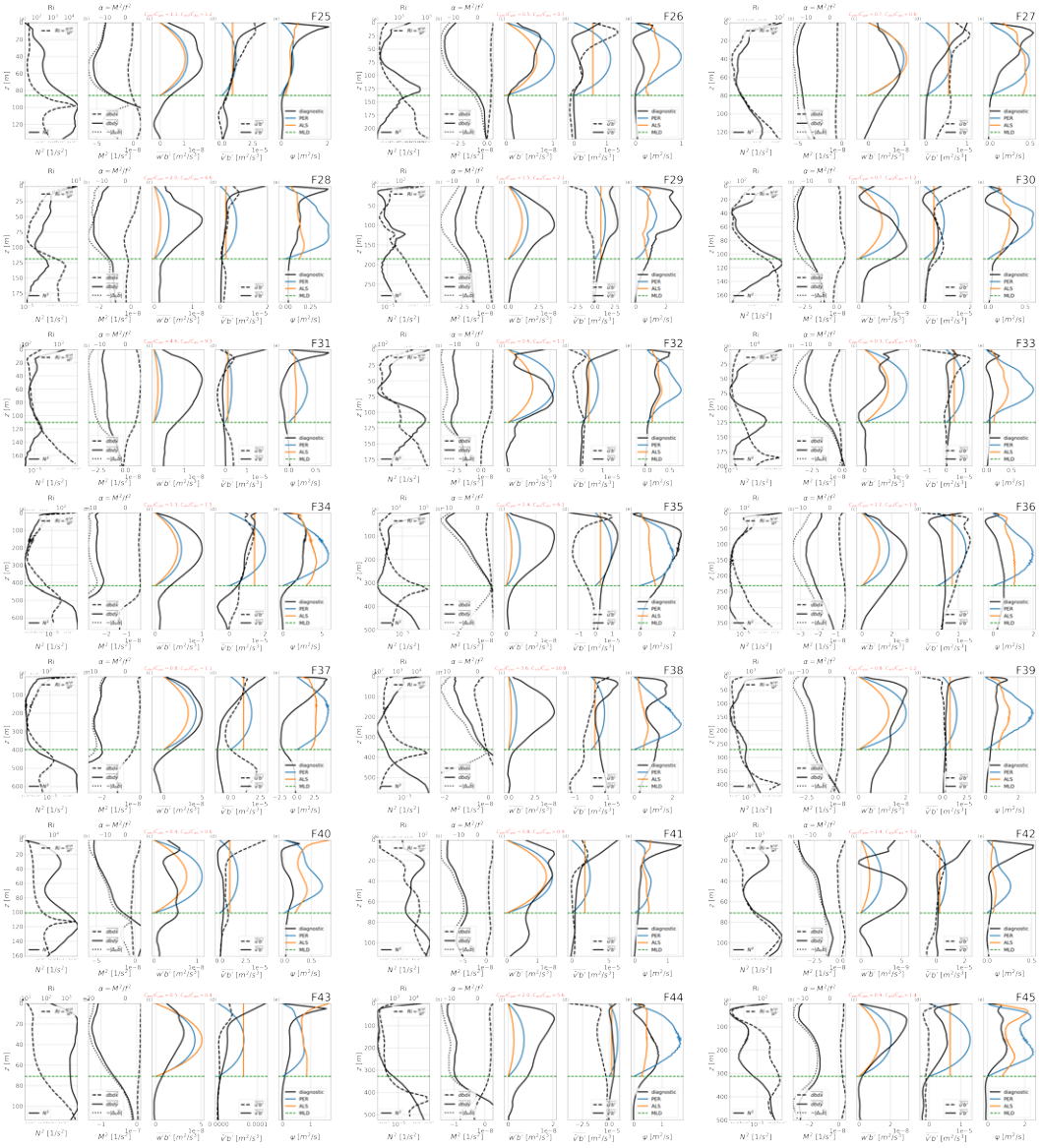

Figure 25: Overview over all evaluated fronts (Part 1 on previous page). The location and extent of each front are shown in Fig. 13. For visualization purposes, the optimal tuning coefficient for each front has been calculated. To assess the variation, the scaling (indicated in red) between the individual tuning coefficients and the overall tuning coefficient (see Tab. 1) is computed. Note that, due to the wide range of maxima and minima, the limits have been adjusted individually for each front.

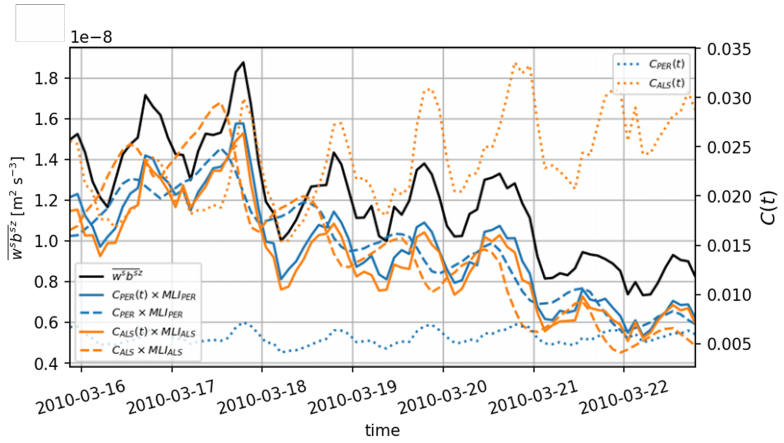

Figure 26: Time series of the spatial median of the submesoscale vertical buoyancy flux averaged over the MLD and its prediction from the MLE parameterizations during a single week in March, adapted from Uchida et al. (2022). The prediction with temporally varying C(t) is shown in blue and orange solid curves and with a temporally averaged (constant) C in blue and orange dashed curves. Note the secondary axis to the right with a tuning coefficient for C(t) for ALS and PER in dotted blue and orange lines, respectively.

	study area	C_{per}	C_{als}
$\overline{w'b'}$ [m^2/s^3]	R	0.002872	0.011148
$\overline{w'b'}$ [m^2/s^3]	their	0.005629	0.023526

Table 3: Tuning coefficients C_{per} and C_{als} for the lateral and vertical buoyancy flux of both parameterization PER and ALS in our study area (see red rectangle in Fig. 7) and their study area (Uchida et al., 2022).

magnitude, but the far shallower mixed layer leads to a substantial increase of the tuning coefficients. Inaccuracies in determining the vertical extent of MLEs therefore have a strong effect on estimating the tuning coefficients. This could be a potential reason for the large variability in tuning coefficients found across the models configurations used in Uchida et al. (2022) (e.g. the surprisingly shallow MLD in LLC4320 noted by Uchida et al. (2022)).

3

IMPACT OF TIDES AND EDDIES ON OCEAN ENERGY SPECTRA IN A SUBMESOSCALE RESOLVING SIMULATIONS OF THE SOUTH ATLANTIC

This chapter is a reprint of the manuscript **Epke, M., Brüggemann, N.**, (2025): "Impact of tides and eddies on ocean energy spectra in a submesoscale resolving simulations of the South Atlantic", currently in preparation for submission.

ABSTRACT:

Comprehending how submesoscale dynamics and their potential interplay with tides affect climate models is challenging due to their small scales and high computational demands. To address this challenge, our approach integrates modelling and observational methods. In this study, we investigate the impact of internal tides, eddies and submesoscale currents on the frequency energy spectrum of the ocean. To this end, we apply a novel simulation with telescopic grid refinement to achieve a horizontal resolution finer than 600 m over large regions of the South Atlantic. This refined resolution allows us to accurately capture submesoscale turbulence and a relatively large part of the internal wave spectrum under realistic atmospheric conditions. By comparing simulations with and without tides, we find that without tidal forcing there is significantly less energy at the high frequency end of the spectrum. Energy levels in the simulation without tides are not only diminished at the well-defined tidal peaks but also in-between the frequency bands between the peaks. This indicates that internal tides facilitate non-linear interactions, such as wave-wave interaction and are therefore key to set the high-frequent end of the energy spectrum. Additionally, the first three baroclinic modes are visible in a frequency-wavenumber spectra, indicating that our model configuration resolves a large part of the internal wave field. Validation with mooring and Pressure Inverted Echo Sounder data sets deployed over a two-year period in the Walvis Ridge region indicates that the simulation with tides is more accurate in terms of high frequency energy levels. We also note that the simulation that applies tidal forcing has still slightly too less energy in between the tidal peaks and too pronounced peaks itself when compared with the observations. If compared to a coarser model configuration, the situation is even more sever. We therefore conclude, that our high-resolution model configuration can simulate parts of the internal wave turbulence, but it is still not sufficiently high resolved to capture its full magnitude.

3.1 INTRODUCTION

Ocean dynamics act on all spatial and temporal scales. Interactions between dynamics on very different scales are known to be essential in setting the large-scale ocean circulation. Therefore, immense research efforts have been carried out to

broaden our knowledge about smaller-scale ocean processes and their role for the large-scale circulation. Often, such efforts are restricted to dynamics that operate on the large to mesoscale regime since higher resolved observations and numerical model simulations are sparse (McWilliams, 2016). In this study, we want to bridge this gap by applying novel observational and modelling tools to assess the energetics of processes acting on kilometer spatial scales and sub-daily temporal scales.

The tool set that we employ ranges from satellite products of unprecedented resolution from the new Surface Water Topography (SWOT) mission, state-of-the-art Acoustic Doppler Current Profiler (ADCP) and Pressure Inverted Echo Sounder (PIES) data deployed at locations where high-frequent, small-scale processes are to be expected and a novel configuration of the ICON-O ocean model that allows to refine the horizontal grid spacing up to sub-kilometer resolution. A similar ICON-O configuration was proven of being able to resolve submesoscale dynamics (see Chap. 2). However, here, we modify this configuration such that the focus area of the grid with its highest spatial resolution is not in the North Atlantic but in the South Atlantic above the Walvis Ridge.

The Walvis Ridge is known as a source of tidally forced internal wave beams (Simmons et al., 2004), it is furthermore a place where strong mesoscale eddies, the so-called Agulhas rings, cross (Biastoch et al., 2009) and where submesoscale dynamics can be expected (Schubert et al., 2019; Schubert et al., 2020). Due to this variety of processes taking place in this area, two research cruises were carried out in April 2021 and April 2023 within the framework of the Collaborative Research Centre TRR181, with the aim of observing this rich variety of dynamics and studying their interactions. The model study applied here was designed to accomplish the data of these two research cruises which are in the following referred to as SONETT I and SONETT II.

The Walvis Ridge region is therefore a hot-spot for many interesting dynamics with very different characteristics and spatial and temporal scales. With the combination of observations and models, we aim to assess the spectral energy levels of those processes and with dedicated sensitivity simulations, we anticipate to isolate single dynamics and characterize their influence on the spectral energy.

The temporal scales of internal waves range between the inertial frequency f and the Brunt-Väisälä frequency N. Like all waves, internal waves have a dedicated dispersion relation that relates the wavelength of a wave to its frequency. While the wave length of so-called short internal waves are in the order of meters, the wave length of long internal waves can be in the order of ten kilometers and longer. Therefore, short internal waves will remain unresolvable for global ocean models during the next decades. In contrast, many models can resolve long internal waves like the frequently discussed near inertial waves with periods close to the Coriolis frequency, if hourly atmospheric wind fields are incorporated (Arbic, 2022; Lahaye et al., 2019). The aim of the underlying model configuration is also to resolve intermediate-scale internal waves, which we refer to as waves whose frequencies are already notable larger than the Coriolis frequency but which are still in hydrostatic balance. Those waves demand a kilometer-scale spatial resolution and are usually not resolved by global ocean models (Müller et al., 2015; Arbic, 2022).

Internal waves can have many sources, like e.g. barotropic tides interacting with topography (Garett and Kunze, 2007), high-frequent wind-forcing (e.g. D'Asaro and Perkins, 1984; Silverthorne and Toole, 2009) or interactions of geostrophic currents or eddies with topography to just name a few. For ocean models to successfully simulate the internal wave field, it is essential that the key sources for internal waves like tidal forcing, high-frequent wind forcing and a vibrant turbulent eddy field are represented in the ocean configuration (Müller et al., 2015; Arbic, 2022).

A key challenge of investigating kilometer-scale and sub-diurnal processes is the disentangling of the different dynamics acting on these scales (Olbers et al., 2012; Bühler, 2014; McWilliams, 2016; Shakespeare et al., 2021). Submesoscale variability, for instance, originates from symmetric, barotropic and baroclinic instabilities at high Rossby numbers (Haine and Marshall, 1998; McWilliams, 2016; Mahadevan, 2016; Gula et al., 2021). Its spatial scale can be substantially smaller than the first baroclinic Rossby radius (see Chap. 2) – a length scale that is usually associated with mesoscale turbulence. Time scales for submesoscale instabilities are more difficult to estimate. From linear stability analysis one obtains that the maximum growth rate of such instabilities can become close to the inertial frequency f and smaller (McWilliams, 2016).

Although the frequencies of waves are larger than the growth rates of submesoscale eddies, a scale separation is difficult. This can be seen from the following thought experiment: assume a train of alternating submesoscale eddies with diameters of $\lambda = 1\,\mathrm{km}$ within a moving current of $U = 0.1 - 1\,\mathrm{m\,s^{-1}}$ current speed. This eddy train will be recognized by a standing observer as a wave with a frequency of $f = 2\pi/\lambda U = 6 \times 10^{-4}\,\mathrm{s^{-1}} - 6 \times 10^{-3}\,\mathrm{s^{-1}}$. Thus, in particular for those waves of the spectrum with frequency close to f, there is no clear scale separation with submesoscale turbulence. Currently, there are some developments regarding the separation of geostrophic motions and internal wave motions (Chouksey et al., 2018; Shakespeare et al., 2021; Chouksey et al., 2023; Masur and Oliver, 2020) However, those methods are not yet in a state that they can be applied in realistic ocean model configurations.

To nevertheless disentangle the different dynamical regimes, we employ dedicated sensitivity experiments to isolate at least some of the processes. Our reference simulation, is one configuration with grid-refinement and tidal forcing and we refer to it as ICON-SMT-Wave (more details regarding all configurations can be found in the following section). Our reference configuration resolves the most processes of all our model configurations. To separate the effect of tidally forced waves, we run a sensitivity simulation that is identical to ICON-SMT-Wave but without tidal forcing (ICON-SMT). Furthermore, we also aim to study the impact of intermediate to high-frequent variability on longer time-scales and therefore, we suppress submesoscale motions and large parts of the internal wave field by a coarser model configuration with only 5 km horizontal resolution. These different sensitivity simulations allow to isolate different processes and their role for the spectral energy distribution in the ocean. Therewith, the simulations accomplish the observational data where such a disentanglement is not possible. These different model configuration and the observational data will be used to assess the impact of different ocean dynamics on high-frequent ocean variability.

The paper is structured as follows: We begin by introducing the observational and model data, showcasing the differences in the variability of the model configurations in Sec. 3.2. This is followed by a detailed description of the methods used to derive spectral estimates from remote sensing, in situ measurements, and simulations (Sec. 3.3). The results are presented in Sec. 3.4, with the discussion and conclusions provided in Sec. 3.5.

3.2 OBSERVATIONAL AND MODEL DATA

Since we are interested in high-frequent dynamics associated with high-frequent variability and since those high-frequent motions usually operate on small spatial scales, there is a strong demand on a high-spatial and temporal resolution of the data that can be used for such a study. To meet this requirement, we make use of the latest efforts in numerical modelling and remote-sensing techniques, but we also use well-established observational methods that allow for high temporal resolution. This section is dedicated to a more detailed description of the data that we apply by first discussing the observational data sets and then introducing our novel numerical model studies.

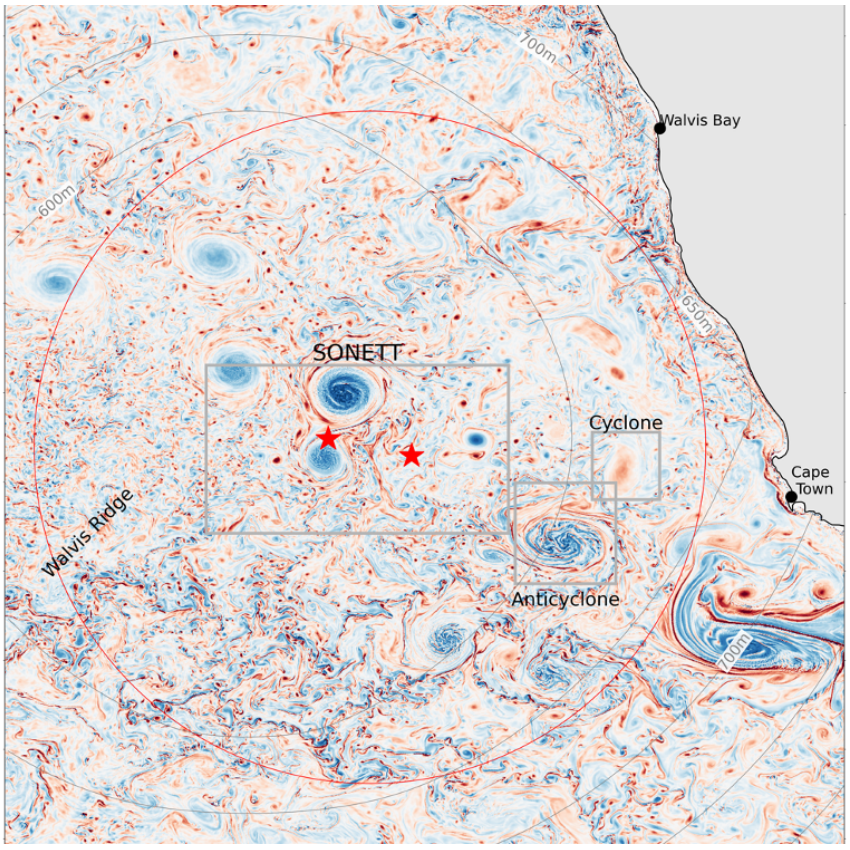

Figure 27: Snapshot of relative vorticity over planetary vorticity in the Southeast Atlantic. The study area of the SONETT cruises is marked by a large rectangle. Mooring locations are indicated with red stars, while PIES instruments are positioned near the eastern star. The red circle highlights the region included in the spectral evaluation discussed in Sec. 3.4. Grey lines represent constant horizontal resolution in the ICON-SMT-Wave model.

3.2.1 *SONETT campaign and SWOT satellite data*

In this study, we incorporate two types of observations: novel remote sensing data from the SWOT satellite and in-situ measurements from our own research cruise, SONETT. The inclusion of in-situ observations is especially valuable, as SWOT is a relatively new mission and its data is not yet fully calibrated. SONETT stands for 'Synoptic Observations - a Nested Approach to Study Energy Transfer and Turbulence' in the Ocean in the Eastern South Atlantic/Walvis Ridge. The research initiative, that was carried out within the Collaborative Research Center TRR181, focuses on observing geostrophic motions, internal gravity waves, and turbulence, conducted in parallel with the fast-sampling phase of the SWOT satellite mission. Instrumentation included two moorings, an underway CTD system, gliders, drifters, wave radar, microstructure turbulence measurements, and five PIES. This study utilizes data from the moorings and PIES, which were deployed in April 2021 and recovered in April 2023, providing a comprehensive two-year observational dataset.

IN-SITU ADCP AND PIES MOORING DATA Two moorings equipped with ADCPs were deployed at locations M1 at 4.63°E, 32.19°S and M2 at 7.11°E, 32.7°S. From the ADCP measurements we can reconstruct time series of horizontal kinetic energy over a period of two years (April 2021-2023). Mooring M1 was configured with 32 depth levels, starting at 32 m, with 8 m intervals between levels and a sampling rate of 15 min. In contrast, mooring M2 featured 16 depth levels, starting at 60 m, with 15 m intervals and a sampling rate of 30 min. To account for depth variations caused by strong currents, particularly near the surface, measurements were interpolated to align with mean depth levels. Two red stars indicate the positions of the moorings in Fig. 27.

The PIES's were deployed in the vicinity of Mooring M2 as indicated in Fig. 27. The bottom pressure signals from these instruments are used to reconstruct the SSH anomalies and compared against the SSH output of the models.[1] The sampling rate is 15 min.

SWOT SATELLITE DATA The recently (2022) launched SWOT mission provides an ideal tool to assess variability in our study area. SWOT's Ka-band Radar Interferometer (KaRin) completes a global cycle every 21 days, and we selected 29 satellite tracks from a single cycle in March 2023 that overlap our study area (see Fig. 27 and Fig. 29). SWOT captures data over two swaths, each approximately 60 km wide, situated on either side of the satellite's ground track (SWOT, 2023). To reconstruct the SSH from SWOT, we combine the mean dynamic topography with the SSH anomaly. Additionally, we incorporate higher-order processed datasets with noise reduction; for further details see (SWOT, 2023). Note that the simulated and observed periods differ, with the simulation representing March 2020 and the SWOT data corresponding to March 2023. Using the same methodology as outlined in Sec. 2, we evaluate the SWOT along-track spectra against our ICON configurations.

1 Note, that also the output generated at the sea bottom could be used to have a more direct comparison.

3.2.2 *The ICON-O SubMesoscale Telescope with tides*

For this study we make use of the ICON SubMesoscale Telescope (ICON-SMT) configuration. In Sec. 2, the model's ability to resolve submesoscale turbulence was validated through comparison with observations, see Chap. 2. Key adaptations for this study include the following:

1. The focus area of the grid was shifted from the North into the South Atlantic such that the refined part of the grid aligns well with two research cruises of the observational SONETT campaign carried out in April 2021 and April 2023 (see Fig. 27 for the study area and the grid refinement).

2. The vertical model levels were altered to have a higher resolution at intermediate and deeper levels to better represent interior wave dynamics. SMT-WAVE employs in total 128 vertical levels, with $dz \leqslant 12\,m$ vertical spacing in the upper 200 m and with $dz \leqslant 50\,m$ within the main pycnocline and $dz \leqslant 200\,m$ in the deep ocean.

3. The model spin-up was performed using the global ICON-R2B9 configuration with a horizontal resolution of 5 km, an improvement over the ICON-R2B8 configuration with 10 km resolution used in Chap. 2.

4. Tidal forcing can be optionally activated.

A number of experiments have been conducted to determine the influence of tidal forcing and model resolution. These included:

- A one-year simulation with tidal forcing (ICON-SMT-Wave)
- A four-month simulation without tidal forcing (ICON-SMT)
- A reference year simulation using the spin-up configuration with tidal forcing and a uniform 5 km horizontal resolution (ICON-R2B9-Wave).[2]

The simulation period (July 2019–2020) is shorter than the two-year observation window (April 2021–2023) due to computational limitations. Additionally, the simulation was set in a different year to accommodate constraints on computational resources, storage capacity, and the availability of reanalysis products required for model forcing.

A first impression, regarding the different dynamics represented by the different model configurations, can be obtained from the local Rossby number in the mixed layer (Fig. 28a, c, e, g) and the vertical velocity at 1000 m depth (Fig. 28b, d, f, h). Here, the Rossby number is used to illustrate the presence or absence of turbulent motions and the vertical velocity is used to illustrate the presence of wave dynamics.

2 Although the resolution of this configuration is nearly ten times coarser to ICON-SMT, it is still high compared to typical climate models with typical resolutions of 25 km-10 km.

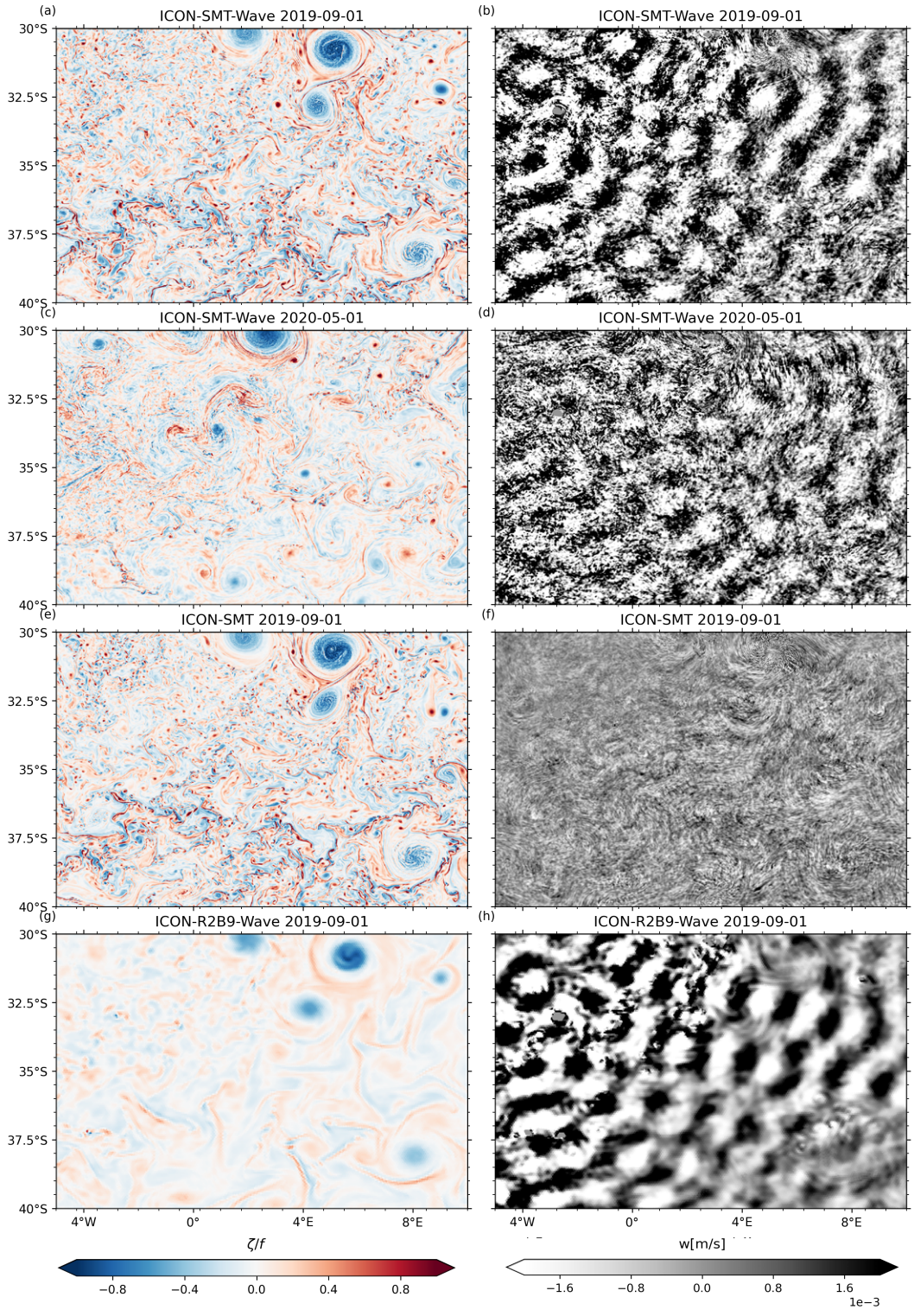

Figure 28: Snapshot of the relative over planetary vorticity at 50 m (left) and the vertical velocity at 1000 m (right). While the first two rows show ICON-SMT-Wave in winter (a,b) and summer (c,d), the lower two rows are different model configuration: Without tidal forcing ICON-SMT (e,f) and without submesoscale resolving resolution ICON-R2B9-Wave (g,h).

The configurations exhibit significant differences across both fields. Enhanced submesoscale activity is observed during local winter in the simulations with grid refinement, no matter if tides are activated (ICON-SMT-Wave, Fig. 28a) or not (ICON-SMT, Fig. 28e). However, the submesoscale motions have a strong seasonal cycle and are substantially stronger in boreal summer (Fig. 28a) compared to boreal winter (Fig. 28c). In the coarser ICON-R2B9-Wave with only 5 km horizontal resolution, submesoscale dynamics are absent (Fig. 28g). Ageostrophic motions are particularly pronounced at ocean fronts, as exemplified by the prominent front observed towards the Southern Ocean (e.g. along 37.5°S during local winter, see Fig. 28a,e).

From vertical velocity fields, a clear imprint of tidal motions is evident in all simulations with tides (Fig. 28b, d, and h). This manifests as coherent wave fronts with a wavelength of approximately 180 km and a semi-diurnal frequency running from north-west to south-east. This contrasts sharply with the configuration without tidal forcing, where such coherent wave fronts are absent (Fig. 28f).

Additionally, we find that the tidal signal becomes blurry in regions of strong negative vorticity, indicating interactions between waves and vortices (e.g. Kunze, 1985). The velocity fields are extremely rich in scale variability, as shown in Fig. 28. Beyond the dominant tidal signal, smaller-scale wave patterns are evident—for example, in the upper right of Fig. 28d, or at even smaller scales near the edge of the large eddy in the upper right of Fig. 28f. It is evident that all three different model simulations provide a rich variety of different dynamics that will be discussed in more detail in the following.

3.3 DERIVING ENERGY SPECTRA FROM OBSERVATIONAL AND MODELLING DATA

WAVENUMBER SPECTRA FROM SWOT DATA For comparison with SWOT, the data from the unstructured ICON grid configurations is mapped to the satellite tracks. Satellite tracks with data gaps exceeding 15% are excluded (see Fig. 29), while the remaining tracks typically have gaps of less than 1%. These are filled with linear interpolation. The SSH fields from ICON-SMT-Wave and ICON-R2B9-Wave are interpolated onto the satellite tracks and times, treating each track as a snapshot. Given the differing resolutions, ICON-R2B9-Wave (coarser) is mapped to a subsampled satellite track with a resolution of 5 km, while ICON-SMT-Wave is mapped directly to match the satellite track resolution. Each track consists of 69 realizations, which are used to compute individual spectral estimates. These estimates are then averaged to produce a robust spectral estimate for each track. The results are shown in Fig. 29. For all spectral computations in this study, we use the Python package XRFT (Fourier Transform for xarray). Standard spectral analysis techniques, including linear detrending and the application of a Hanning window, are also employed.

FREQUENCY SPECTRA FROM ADCP DATA To evaluate the variability in horizontal kinetic energy, we derive spectra from both model configurations and ADCP measurements. While the moored ADCPs provide data at fixed locations over a two-year period, the model generates full spatial fields but is constrained by re-

source limitations, restricting the timespan. Individual Agulhas rings can significantly influence the signal on monthly to seasonal timescales. For example, a four month timeseries at a single location would be dominated by an Agulhas ring which takes roughly two-three month to pass. To address the constraints of the relatively short simulation runtime, we derive the spectra not only at the mooring locations, but for all points within a 10° radius around the mean mooring location (indicated by the red circle in Fig. 27), gridded on a regular 0.1° grid (in total, we derive spectra for 31408 points). Finally, we average each estimate of the power spectral density that we obtained for each point to derive a robust mean spectrum from the model data.

A sensitivity analysis indicates that a one-year time series is relatively insensitive to the size of the averaging region (we test $1 - 5°$ and 10°; not shown). For shorter time series, we noted some sensitivity to the domain size (not shown) and therefore always applied the largest domain once those shorter time series were analyzed.

To obtain a robust spectral estimate of horizontal kinetic energy from the ADCP measurements, a slightly different approach is employed. Given the availability of approximately two years of time series data, the dataset is divided into 24 independent monthly time series[3]. Measurement gaps are filled using linear interpolation. Additional realizations are generated by subsampling the ADCP time series that has a frequency of 15 min (M1) and 30 min (M2) to match the model's sampling frequency of one hour. Furthermore, measurements from neighboring depth levels (e.g. for the evaluation of the 100 m level the depth measurements from 98, 108m are combined for M1; and 96, 104, 112 m for M2) are included to enhance the robustness of the spectral estimate at a specific depth. The spectral estimates for the kinetic energy are given in Fig. 30.

FREQUENCY SPECTRA FROM PIES DATA A slightly modified procedure is used to derive spectral estimates from the measurements of all five PIES. The measurement period is divided into two separate one-year intervals, and the original sampling frequency of 15 min is downsampled to match the model's one-hour sampling frequency. Finally, the spectral estimates from all five instruments are averaged to produce a single composite spectral estimate, see Fig. 31.

FREQUENCY-WAVENUMBER SPECTRA FROM MODEL DATA Another method for detecting internal wave signals is to analyze the frequency-wavenumber spectra, for other example see (e.g., Qiu et al., 2019; Cao and Jing, 2022; Lahaye et al., 2019; Arbic, 2022). In this study, we evaluate sea surface height (SSH) over a $20° \times 20°$ regular grid spanning approximately three weeks. We apply a 3D fast Fourier transform (3D FFT) to the temporally detrended SSH and reduce the second spatial dimension by binning and averaging over wavenumber k_h. Thus, we obtain a power spectral density estimate of the frequency-wavenumber of the SSH, presented in Fig. 32.

3 Note that this increase in realizations is necessary to reduce the noise at the high frequency end of the spectrum which is essential for an evaluation of the internal wave band.

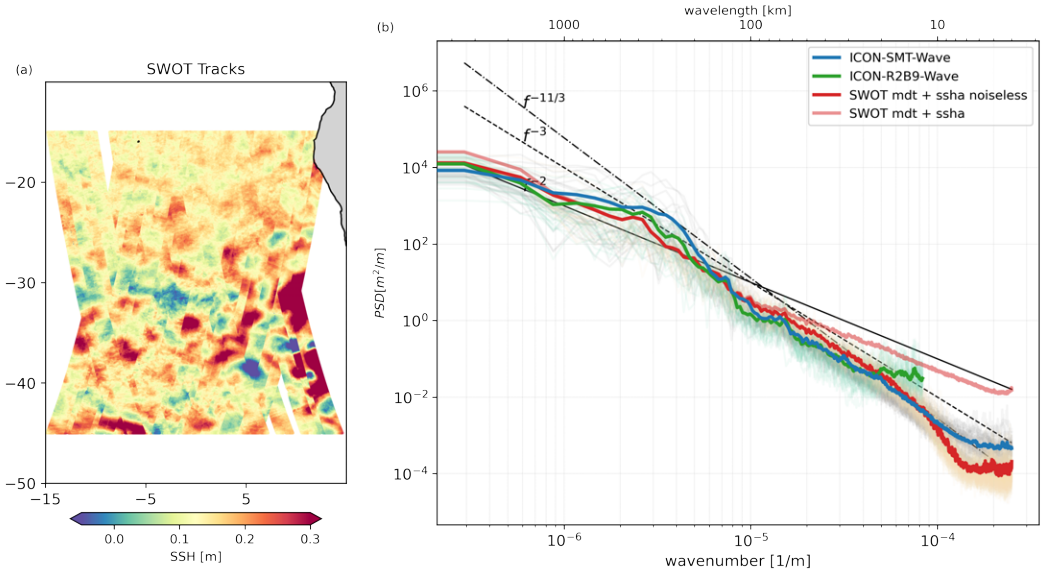

Figure 29: (a) SSH anomaly of along SWOT satellite tracks. (b) Along-track SSH anomaly wavenumber spectra derived for the SWOT data shown in (a) and for the tidally forced ICON-SMT-Wave and ICON-SMT-R2B9 configurations, which were mapped to the tracks of the SWOT satellite. Averages across all tracks for both satellite and model data are shown in the figure: the blue line represents ICON-SMT-WAVE, the green line represents ICON-R2B9-Wave, and the red lines correspond to SWOT. The dark red line specifically denotes the noise-filtered SWOT signal. Lines with weak opacity indicate spectra of single tracks. Note that, we evaluate a snapshot in March 2019 (ICON configurations) with SWOT observations in March 2023.

3.4 IMPACT OF DIFFERENT DYNAMICS ON OCEAN ENERGY SPECTRA

In this study, we assess energy frequency and wave number spectra from observational and model data. By comparing the spectra of the different sensitivity experiments, we will analyze how the represented dynamics affect parts of the energy spectra.

3.4.1 *Comparison with SWOT*

The mean spectra averaged over all tracks for SWOT, ICON-SMT-WAVE and ICON-R2B9-WAVE simulations are shown in Fig. 29. Overall, we find a strong agreement between both ICON configurations and SWOT. Differences at the high-frequency end of the spectra can be attributed to the respective noise floors of each dataset. For wavelengths between 300 km $> \lambda >$ 10 km we find a slope closer to $-11/3$ than to -5, thus in closer agreement with surface-quasi-geostrophic theory rather than quasi-geostrophic theory (Lapeyre et al., 2006; Capet et al., 2008a; Arbic, 2022; Xu et al., 2022). The noise-reduced dataset from (SWOT, 2023) refines the 'raw' signal starting at wavelengths of 80 km and extending towards shorter wavelengths. Without the application of noise filters, the observed energy levels deviate significantly from both model configurations. It is important to note that the noise-reduction process is still under development and should be interpreted with caution.

The agreement between ICON-SMT-Wave and ICON-R2B9-Wave is unexpected, given the substantial differences observed in Chap. 2 between the 10 km reference run and ICON-SMT. This indicates that ICON-R2B9-Wave demonstrates significantly better performance than the 10 km ICON configuration analyzed in Chapter 2.

3.4.2 *Continuous frequency spectrum*

Few studies have had the opportunity to directly evaluate their submesoscale-resolving models against in-situ observations. In this study, we are in the fortunate position that we can do such a comparison.

COMPARISON WITH MOORED ADCPS The averaged frequency spectra for the three model configurations and both moorings are presented in Fig. 30. At 100 m depth and for periods ranging from weeks ($2e^{-1}$[cpd]) to several hours (4[cpd]), both simulations, ICON-SMT and ICON-SMT-Wave, are in good agreement with the observations from the mooring ADCPs (see Fig. 30a). In contrast, the coarser ICON-R2B9-Wave has less energy on nearly all frequencies except the smallest estimated frequencies and the diurnal and semidiurnal frequencies. The absence of submesoscale energy at intermediate scales (between weekly and daily periods) in the ICON-R2B9-Wave compared to the high resolution model suggests a missing inverse cascade. At the high frequency end of the spectrum, there appears to be only energy at spectral peaks associated with tidal frequencies and their higher harmonics. In between those peaks, the spectrum falls of.

In ICON-SMT which does not apply tidal forcing, the missing peaks for the tidal frequencies and their subharmonics are directly evident. On frequencies at and lower than the inertial period, the spectrum from ICON-SMT is relatively similar to that from ICON-SMT-Wave, indicating that the missing tides do not play a major role for the energy levels in the low frequency range. On frequencies higher than the semi-diurnal peak, however, the spectra of ICON-SMT and ICON-SMT-Wave differ more substantially. Not only are the tidal peaks missing, as might be clear from the setup of the simulations, the energy spectrum of ICON-SMT is lower on all frequencies below the semi-diurnal frequency.

Observed kinetic energy spectra typically show a continuum of internal wave energy extending to high frequencies and high vertical wavenumbers (Garrett and Munk, 1975; Arbic, 2022). ICON-SMT-Wave appears to provide a significantly improved representation of this continuous spectrum at high frequencies, where energy levels fill in between the peaks. This contrasts sharply with the 5 km model, which only exhibits discrete tidal peaks and subharmonics. Since the internal gravity wave continuum is thought to arise from nonlinear interactions between internal gravity waves (Arbic, 2022), this suggests that ICON-SMT-Wave captures a larger fraction of these dynamics than ICON-R2B9.

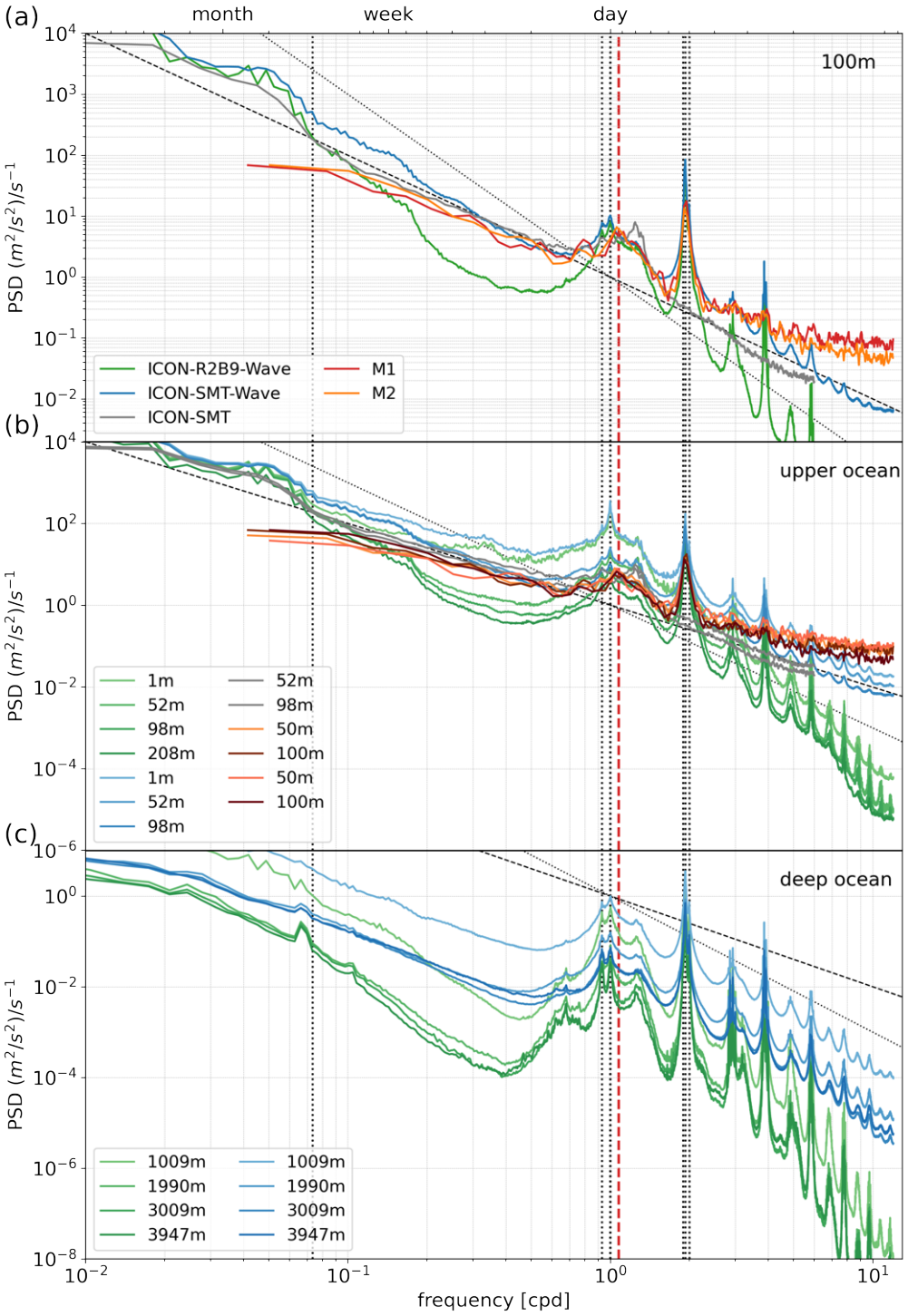

Figure 30: The frequency spectra of the horizontal kinetic energy from three ICON configurations and two moorings (M1, M2) at 98 m depth (a), in the upper ocean up to 200 m depth (b) and in the deep ocean (c). Note that the kinetic energy of ICON-SMT has an output every 2 h instead of 1 h for ICON-SMT-WAVE and ICON-R2B9-WAVE. For the evaluation, all model points within a radius of 10° radius around the mean Mooring location (Fig. 27) are gridded to a 0.1 degree grid and the individual spectra are averaged to obtain the mean spectra shown here. The Coriolis frequency is represented by a red dashed line, while the first tidal constituents are shown as grey dotted lines. Additionally, the spectral slopes of -2 (dashed) and -3 (dotted) are included.

Moreover, achieving a -2 slope in the high-resolution models is critical for consistency with theoretical predictions and observational data (Ferrari and Wunsch, 2009; Xu et al., 2022). High resolution appears to be essential for accurately capturing the energy cascade and maintaining agreement with these benchmarks.

Except for the surface layer, which seems more energetic, we observe similar spectra at 50 m, consistent with observations, as shown in Fig. 30b. At greater depths, the slope of the ICON-SMT-Wave spectrum beyond diurnal frequencies approaches a -3 slope rather than the expected -2 slope (see Fig. 30c). This may suggest that the energetic dynamics of the deep ocean are not as well represented as those of the upper ocean.

COMPARISON WITH PIES The model and observational frequency spectra of the SSH are shown in Fig. 31. At periods ranging from several months to days, we observe a good agreement of the energy levels between all model configurations and the observations. In all cases, the spectra follow a -3 slope. Although we note slightly higher energy levels between periods from five to nine days in the PIES spectrum. Near-inertial and tidal peaks, along with subharmonics, are well-represented in the tidally forced model configurations ICON-SMT-Wave and ICON-R2B9-Wave, while ICON-SMT lacks these tidal peaks. ICON-SMT also exhibits significantly lower energy levels at high frequencies and a slightly steeper slope compared to ICON-SMT-Wave. Although ICON-R2B9-Wave correctly reproduces the spectral peaks, its energy levels are much weaker and its slope is steeper than that of ICON-SMT-Wave, resembling ICON-SMT more closely.

It is important to note that the noise floor of the PIES is reached at energy levels below $10^{-1}, \mathrm{m}^2/\mathrm{s}$. At these levels, comparisons with the models are not reliable; however, we can trust the spectral peaks that exceed this limit. It is apparent that the models overestimate the spectral energy density for nearly all spectral peaks (exceptions are the peaks at $M2 + f$ and $\omega = 7[\mathrm{cpd}]$) and they underestimate the energy spectral density for frequencies in between the spectral peaks. These biases might be an indication for too weak wave turbulence that distributes the energy in spectral space from the peaks where it is forced to the neighboring frequencies.

For frequencies smaller than diurnal frequencies, there is a good agreement between the model and the PIES data. However, between frequencies corresponding to six to nine days, the PIES data seems to be slightly enhanced. This might be a consequence of the synoptic ocean state that can have a substantial influence on the spectrum, in particular when Agulhas rings are crossing. For the model data, the spatial averaging reduces the impact of the synoptic eddy field for the PIES data such an averaging is not possible which is why this data might be stronger contaminated.

Despite the described discrepancies, we nevertheless conclude that the SSH frequency spectra of all model configurations are in relatively good agreement with the observed SSH spectra from the PIES up to the semi-diurnal peak. For smaller frequencies, a higher resolution and the tidal forcing become essential in reproducing the observed spectrum.

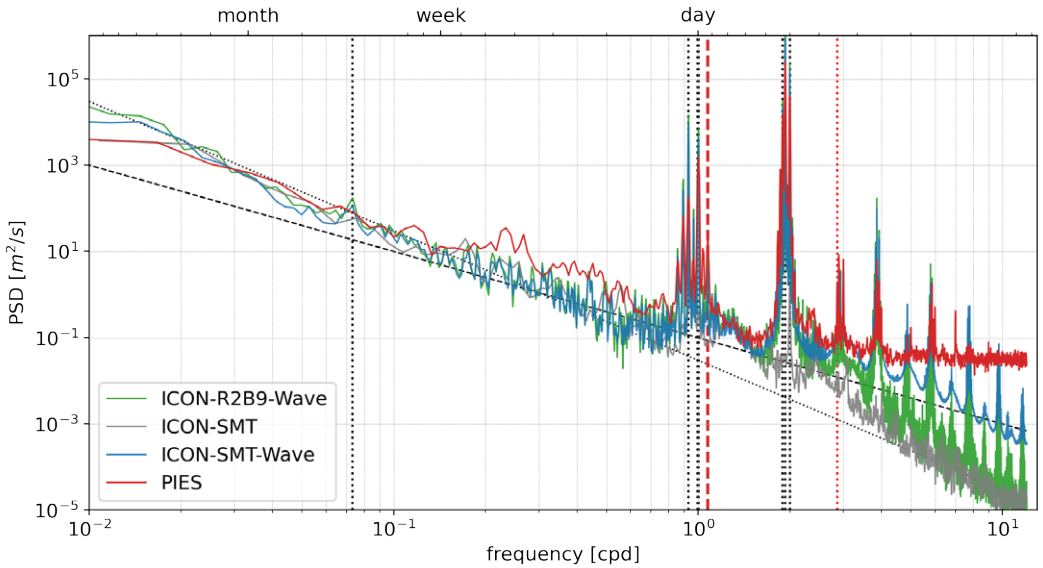

Figure 31: Averaged sea surface hight frequency spectra from the different ICON configurations and the PIES data. For the evaluation, all model points within a radius of 10° radius around the mean Mooring location (Fig. 27) are gridded to a 0.1 degree grid and the individual spectra are averaged to obtain the mean spectra shown here. The Coriolis frequency f is indicated with a red dashed line, the sum of Coriolis frequency and M2 frequency f + M2 is depicted by a red dotted line and the first tidal constituents are denoted by grey dotted lines.

INTERNAL WAVE SIGNALS IN SSH FREQUENCY-WAVENUMBER SPECTRA We present the frequency-wavenumber spectra of SSH for both ICON-SMT and ICON-SMT-Wave (Fig. 32).

The imprint of tidal forcing on internal wave generation becomes immediately evident when comparing the difference of ICON-SMT-Wave and ICON-SMT, see Fig. 32d. A comparison of the model configurations reveals that tidal forcing enhances energy levels at inertial f, semi-diurnal M2 and subharmonic frequencies, as evident from the horizontal stripes in Fig.32b,c. The only exception is a wavenumber band between 200 km-500 km, where we have more energy in the model without tidal forcing. Note that the Agulhas have a related length scale.

Additionally, we observe increased energy between tidal frequencies when submesoscale dynamics are resolved (Fig.32e,f). This finding is consistent with our previous results in Fig.31 and aligns with observations by (Lahaye et al., 2019). The presence of tidal forcing appears to facilitate nonlinear wave-wave interactions, leading to energy redistribution across scales.

We observe increased energy levels along frequencies and wavenumbers predicted by the dispersion relation in the tidally forced models (Fig. 32b,c). ICON-SMT-Wave resolves the first three baroclinic modes of long waves, while ICON-R2B9-Wave captures the first two. Since this model configuration applies the hydrostatic approximation, it does not permit short waves (Olbers et al., 2012). In the model configuration without tidal forcing, energy levels along the dispersion relation remain elevated, particularly between M2 and 2M2, albeit much weaker (Fig. 32a). This suggests the presence of internal waves generated independently of tidal forcing, likely due to wind forcing or flow-topography interactions.

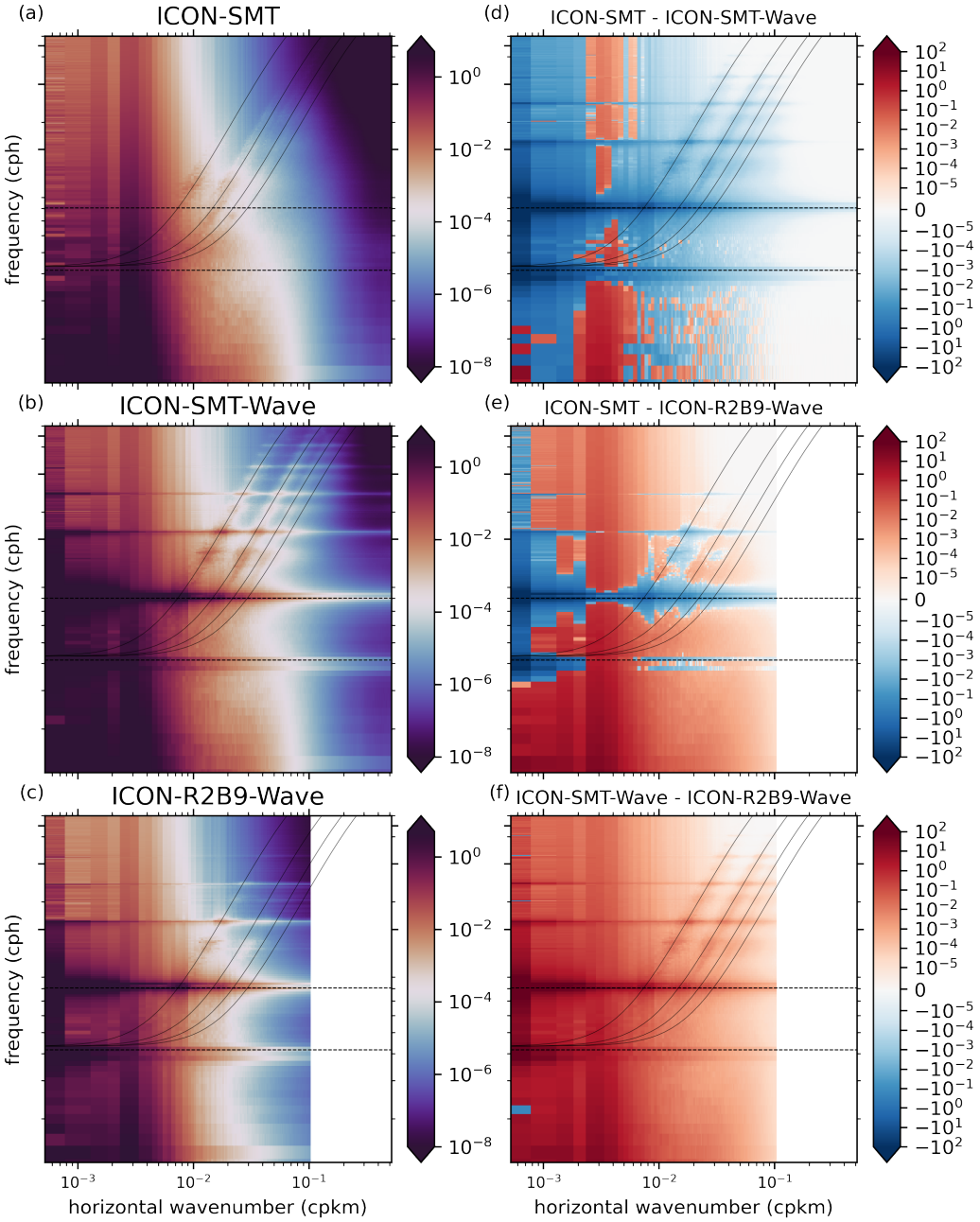

Figure 32: The frequency-wavenumber $\omega - k$ spectra of the SSH obtained from a $20° \times 20°$ region in our study area and three week time series in August (local winter) for all model configurations (left) and the difference between the model configurations (right). The Coriolis frequency and the semi-diurnal frequency are denoted by black dashed lines. Theoretical expectations of the first three wave modes are shown by thin black lines. The Brunt Väisäla frequency is estimated with $N = 1.6e^{-3}[1/s]$.

We note small differences between our estimates of the dispersion relation and the observed stripes of enhanced energy levels, which appear slightly steeper. These differences may arise because we simplify the dispersion relation using an estimated N and the first three vertical baroclinic modes, calculated as $\omega_n = \sqrt{f^2 + (N^2 k_h^2)/(k_h^2 + m_n^2)}$ and $m_n = n\pi/H$. A more accurate approach might involve computing the characteristic N and solving the Sturm-Liouville problem to obtain a better-fitting dispersion relation (Olbers et al., 2012).

3.5 SUMMARY AND CONCLUSION

In this study, we investigated ocean variability using a new configuration of ICON-o, the SubMesoscale Telescope (ICON-SMT), alongside remote sensing and in-situ observations. To disentangle the impact of submesoscale dynamics and tidal forcing, we conducted a series of simulations, including ICON-SMT-Wave (with tidal forcing), ICON-SMT (without tidal forcing), and ICON-R2B9-Wave (with tidal forcing but lower resolution). The variability of key quantities, such as horizontal kinetic energy and sea surface height, was analyzed through frequency and wavenumber spectra.

ICON-SMT-Wave demonstrates a remarkable agreement with observations across all evaluations, although limitations due to instrument noise in the observational data prevented a full evaluation across all scales, particularly at very high frequencies in the SSH spectra. While ICON-R2B9-Wave captured SSH variability reasonably well, its kinetic energy spectra revealed significantly weaker energy levels at intermediate and high frequencies. This suggests the absence of energy cascades to both larger and smaller scales, highlighting the critical importance of resolving submesoscale dynamics and including tidal forcing in accurately representing ocean variability.

The key results of this study can be summarized as follows:

- Motions on the kilometer-scale are responsible to obtain a -2 slope in the horizontal KE spectra as becomes evident from a comparison of the higher resolved ICON-SMT-Wave with the coarser ICON-R2B9-Wave, see Fig. 30. Here the former agrees well with theory and observations while the spectrum of the latter becomes to flat for higher wavenumbers as a result of the limited resolution and the damping on the grid scale.

- In contrast, the comparison with SWOT reveals a consistent -11/3 slope in the SSH wavenumber spectra across both model configurations and observational data, emphasizing that intermediate scales in the SSH variability are less influenced by kilometer-scale motions (Fig. 29).

- Dynamics related to tides are essential for the energy levels towards the high frequency end of the spectrum of SSH and KE, see Fig. 31,30. Here, near inertial and tidal peaks as well as subharmonics are well represented in the tidally forced model configurations but absent in the simulation without tides (Fig. 31).

- Tidal forcing not only improves the realism of the spectra by reproducing the expected tidal peaks and subharmonics but also by providing more energy

to frequencies which are in between the peak frequencies (30). This suggests that tidal forcing enhances non-linear interactions, such as wave-wave interactions, which play a crucial role in redistributing energy across the spectral space.

- The spectral peaks are overestimated by the model configurations and the energy level in between the peaks is underestimated. While this effect is strongly reduced in ICON-SMT-Wave it is more apparent in the coarser ICON-R2B9-Wave (Fig. 31). This points to missing wave-wave interactions in both configurations but ultimately stronger in the coarser ICON-R2B9-Wave configuration.

- The reduced energy levels on daily to weekly frequencies in ICON-R2B9-Wave (Fig. 30), compared with ICON-SMT-Wave is most likely associated with the missing submesoscale eddy field. From this one might conclude on a submesoscale turbulent timescale ranging roughly from one to seven days in the South Atlantic.

- Internal Wave signature in the frequency-wavenumber spectra. ICON-SMT-Wave can resolve the first three and ICON-R2B9-Wave can resolve the first two baroclinic modes. Additionally, we find evidence for internal waves in ICON-SMT, generated from wind and or topography.

Our results demonstrate that submesoscale-resolving models, such as ICON-SMT, significantly enhance the representation of ocean variability, marking a major step toward more realistic ocean simulations. In particular, these models capture the crucial processes of energy cascades across scales, both upward and downward. Additionally, we show that incorporating tidal forcing in such simulations is essential. Furthermore, we demonstrate that our optimal model configuration, ICON-SMT-Wave, can resolve the first three baroclinic modes. Additionally, we highlight that the model exhibits an internal wave imprint even in the absence of tidal forcing. Internal tides facilitate nonlinear interactions with mesoscale eddies, which is crucial for energy transfer to both smaller and larger scales. This process contributes to elevated energy levels at high frequencies, making tidal forcing fundamental for accurately representing the wave continuum. Such sub-kilometer scale models can therefore form an essential tool in better understanding high-frequent dynamics in the ocean, and they can accomplish observations which are often sparse in time or space.

4

HIGH-FREQUENCY VARIABILITY GENERATED BY MESOSCALE EDDIES INTERACTING WITH BATHYMETRY IN A SUBMESOSCALE-RESOLVING SIMULATION OF THE SOUTH ATLANTIC

This chapter is based on an early-stage manuscript titled **Epke, M., Brüggemann, N.**, (2025): "High-Frequency Variability Generated by Mesoscale Eddies Interacting with Bathymetry in a Submesoscale-Resolving Simulation of the South Atlantic".

ABSTRACT:

Agulhas Rings play a crucial role in the dynamics of the South Atlantic, particularly through their interactions with the Walvis Ridge. However, the influence of mesoscale eddies, their interaction with bathymetric features, and their effects on high-frequency ocean dynamics remain poorly understood, especially in realistic setups. To address this, we combine high-resolution numerical simulations with telescopic grid refinement, achieving horizontal resolutions below 600 meters across large regions of the South Atlantic.

Using an eddy-tracking algorithm, we investigate the evolution of three anticyclones interacting with bathymetric features, notably the Vema Seamount (rising 35 meters below the surface) and the Walvis Ridge (extending 800 meters below sea level where the eddies cross). We observe a significant interaction between a large Agulhas Ring and the Vema Seamount, which leads to the redistribution of water masses, a marked deepening of the mixed layer, and the generation of various processes such as barotropic and baroclinic instabilities, and Lee waves. Hovmöller plots reveal the presence of near-inertial waves and Lee waves generated by these eddy-topography interactions.

By isolating eddies from the flow field, we derive energy frequency spectra for the flow within and outside of Agulhas Rings. Inside these eddies, we observe a notable shift towards higher power spectral densities—approximately an order of magnitude larger greater—across both small and large frequencies. During an interaction of an eddy with the Vema Seamount energy levels increase by three orders of magnitude at intermediate and high frequencies. These findings provide new insights into mesoscale-bathymetry interactions and their crucial role in shaping high-frequency ocean dynamics in the South Atlantic.

4.1 INTRODUCTION

Mesoscale eddies play a crucial role in ocean dynamics by redistributing energy across scales. As they propagate, these eddies interact with ocean topography, influencing the transfer of energy and the generation of high-frequency motions. In this study, we investigate how ocean topography modulates energy redistribution, with a particular focus on submesoscale dynamics and the generation of internal

waves. Our study region provides an ideal test bed for exploring the interplay between topography, mesoscale eddies, baroclinic tides, and internal waves.

The Agulhas Current system is a major component of global ocean circulation, facilitating water mass exchange between the Indian and Atlantic Oceans (Talley et al., 2011). A defining feature of this system is the formation of Agulhas rings—large mesoscale eddies shed at the Agulhas retroflection. Unlike typical baroclinic instability-driven eddies, Agulhas rings are generated primarily by the zonal momentum flux of the retroflecting Agulhas jet (Pichevin et al., 1999). These rings are among the most energetic features in the global ocean and play a key role in Agulhas leakage, transporting warm, saline Indian Ocean waters into the South Atlantic, with substantial subsurface transport (Schouten et al., 2000; Richardson, 2007; Schmid et al., 2003). This process has significant implications for the Atlantic Meridional Overturning Circulation (AMOC) and global climate (Biastoch et al., 2009; Beal et al., 2011; Laxenaire et al., 2020). Additionally, Agulhas rings influence regional ecosystems by affecting nutrient transport and plankton communities (Krug et al., 2014; Guerra et al., 2022).

Beyond their role in interoceanic exchange (Schmid et al., 2003), Agulhas rings strongly interact with bathymetric features such as the Walvis Ridge as they propagate through the Cape Basin. These interactions generate energetic internal waves, particularly lee waves, which are known to be prominent in this region (Nikurashin and Ferrari, 2011). Lee waves play a crucial role in energy dissipation, acting as a major sink for geostrophic currents (Ferrari and Wunsch, 2009; Musgrave et al., 2022). Together with internal tides, these waves contribute to energy redistribution by facilitating breaking, turbulence, and mixing across the basin (Ferrari and Wunsch, 2009; Nikurashin and Ferrari, 2013; Musgrave et al., 2022).

Recent studies have simulated lee waves and compared them with observations of steady lee waves (Marez et al., 2020a), as well as evaluated their influence on Southern Ocean circulation (Yang et al., 2021). However, studies of lee waves in realistic ocean models remain sparse due to their inherently small scales. Few model configurations can resolve these waves, and those that do have not been extensively used to investigate their role in energy transfer. Additionally, previous nested simulations have faced limitations, such as boundary condition constraints. We demonstrate that our high-resolution model is capable of resolving lee wave generation and propagation, providing new insights into how transient mesoscale eddies generate and modulate lee waves as they interact with bathymetric features like isolated seamounts and the Walvis Ridge.

Previous studies have shown that the SubMesoscale Telescope (ICON-SMT), a novel model configuration utilizing continuous grid refinement, can resolve kilometer-scale turbulence and is in remarkable agreement with both in situ and remote sensing observations, see Chap. 3. These studies demonstrated that tidal forcing and resolved submesoscale dynamics play a fundamental role in setting energy levels at the high-frequency end (see Chap. 2 and Chap. 3). Additionally, ICON-SMT effectively captures a large fraction of internal wave dynamics, making it an ideal configuration for studying high-frequency processes in a realistic environment.

In this study, we take a step further by disentangling the processes contributing to high-frequency variability, focusing on the impact of mesoscale eddies and

indirectly triggered phenomena such as internal waves. This study focuses on mesoscale eddies interacting with topography and their role in generating high-frequency variability. We aim to disentangle the processes leading to enhanced variability, particularly the generation of submesoscale dynamics and internal waves at topographic features. To achieve this, we employ two high-resolution model configurations with grid refinement in the South Atlantic, enabling us to study the evolution of mesoscale eddies and their interactions with topography. Previous work has demonstrated that this model setup effectively resolves kilometer-scale turbulence (see Chap 2 and Chap. 3). Addressing this gap is essential for improving our understanding of mesoscale-topography interactions and their broader implications for ocean circulation and climate.

The paper is structured as follows: After a brief discussion of the model configuration (Sec. 4.2), the eddy tracks and composition methods as well as the evolution of six anticyclones are described in Sec. 4.3. In addition, the interaction of an eddy with a seamount is highlighted in Sec. 4.4. The impact of mesoscale eddies on the wave field is introduced in Sec. 4.5. Finally, we close with a conclusion (Sec. 4.6).

4.2 MODEL CONFIGURATION

In this study, we utilize the telescoping model configurations described in Chapter 3, focusing on the South Atlantic region near the Walvis Ridge. In Sub-Mesoscale-Telescope (SMT) model, the horizontal resolution varies between 530 m in the focus area and 11 km away from this focus area (see Fig. 27 in Chap. 3 for more details regarding the horizontal resolution). We employ the ICON-SMT configuration, which is a four-month (July 2019 - October 2019) simulation without tidal forcing, and ICON-SMT-Wave, a one-year (July -2019 -July 2020) simulation with tidal forcing. In addition, a reference year simulation using the spin-up configuration with tidal forcing and a 5 km horizontal resolution (ICON-R2B9-Wave) has been carried out. SMT-WAVE employs in total 128 vertical levels, with $dz \leqslant 12\,m$ vertical spacing in the upper 200 m and with $dz \leqslant 50\,m$ with the main pycnocline and $dz \leqslant 200\,m$ in the deep ocean. The model's ability to resolve submesoscale turbulence and a large part of the internal wave spectrum has been successfully shown in Chap. 2 and Chapter 3.

4.3 EDDY TRACKS AND COMPOSITES

To study the behavior of the Agulhas rings, we develop a novel methodological approach. First, we track the trajectories of the largest six anticyclones in the study area using an eddy tracking algorithm[1], see the tracks in Fig. 33. For each identified eddy, we perform a coordinate transformation to reposition the center of the grid at the eddy core, ensuring that the eddy core remained consistently centered throughout the analysis. Next, we interpolate the data from the native model grid onto a 0.01° regular grid, cropping a $5 \times 5^\circ$-region centered around the eddy core. We repeat this process for each time step, generating a sequence of spatial fields that we concatenate to construct a four-dimensional composite dataset rep-

1 for details see the python package PYEDDYTRACKER from (Delepoulle et al., 2022)

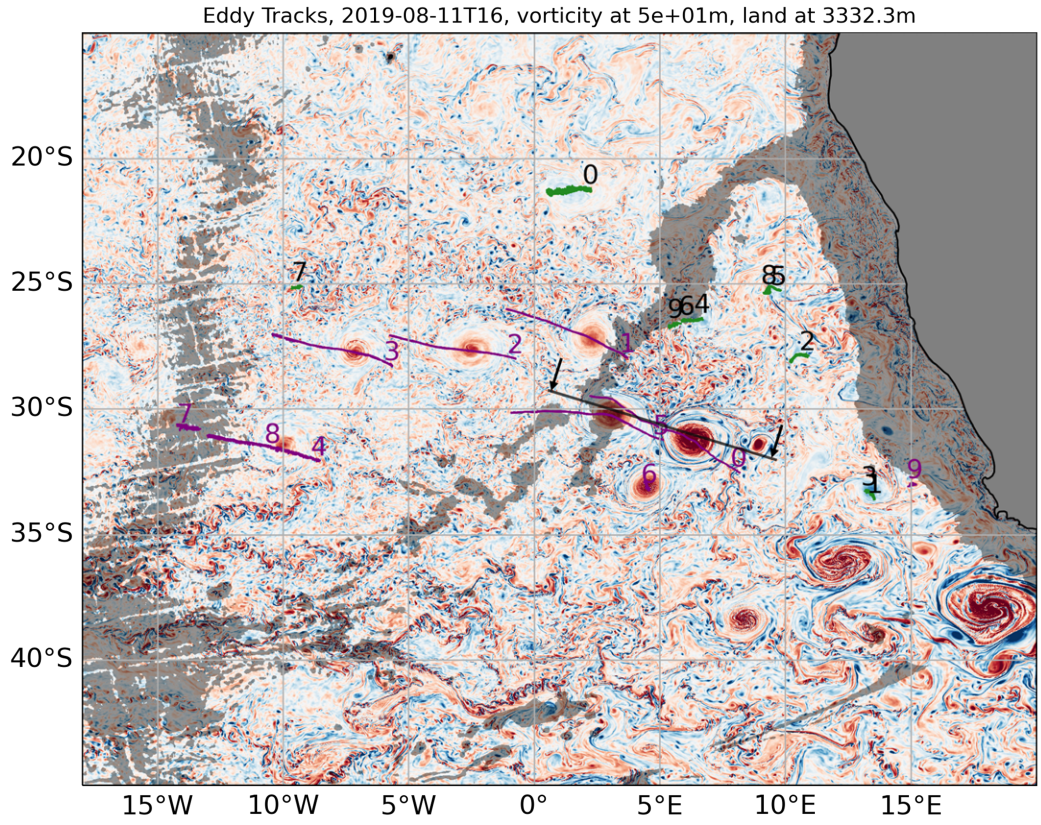

Figure 33: Above a snapshot of the vorticity at 50 m the Tracks of anticyclones (purple) over a four-month period from July-October 2019 are shown. The grey shading indicates sea floor topography at 3392 m. Note that the eddy tracking can fail at single time steps and thus results in double labeling (e.g. eddy ID 4 and 8 describe the same eddy). The color limits of the vorticity are -1 and 1. The section in Fig. 38 is indicated with a black line and two arrows.

resenting the eddy evolution over two months. A comparative snapshot of two anticyclones is shown in Fig. 34.

For long-lived anticyclones, we observe a gradual weakening and reduction in size as they propagate northwestward from their formation in the retroflection region to the vicinity of the Mid-Atlantic Ridge (Fig. 33). Our findings align with drifter observations reported by Richardson (2007), which indicate that Agulhas rings become more circular and coherent over time. This evolution is particularly evident in the vorticity field when comparing young eddies located east of the Walvis Ridge with older eddies west of it (Fig. 33). Additionally, the tracks of eddies ID0, ID1, and ID5 support the observation by Schouten et al. (2000) that eddies often cross the Walvis Ridge at its deepest point.

The characteristics of two anticyclones are presented in Fig. 34. These eddies have notably higher energy levels compared with the background flow. Eddy ID0 exhibits a periodicity of approximately $5-6$ days, consistent with previous observations by Schouten et al. (2000). East of the Walvis Ridge, the horizontal scale of these eddies in the upper ocean spans between $1.8-2.7° \approx 100-200$ km. Both eddies strongly displace the pycnocline downward by approximately 300 m and therewith increasing the thickness of the upper-ocean mixed layer. Enhanced ki-

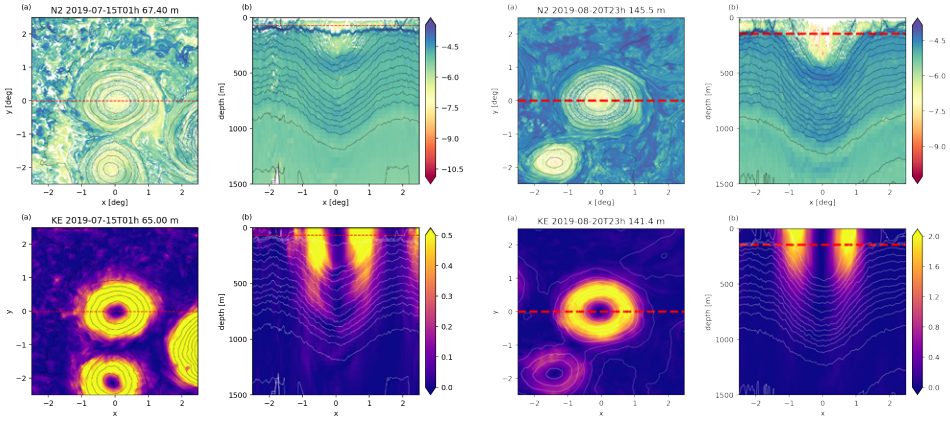

Figure 34: A snapshot of anticyclones ID5 (2019-07-15, left) and ID0 (2019-08-20, right) showing stratification (top), kinetic energy (middle), and turbulent kinetic energy (bottom). Notably, Eddy ID0 experienced strong interaction with the Vema Seamount, resulting in a mixed layer depth extending up to 400 m. The red dashed lines indicate the locations of the lateral and vertical sections. Black contours represent constant values of SSH and density.

netic energies can be observed up to a depth of below 1300 m indicating the vertical scale of these eddies. This agrees with observations by Casanova-Masjoan et al. (2017), who reported eddy-driven penetration reaching up to 2000 m.

4.4 IMPACT OF BATHYMETRY ON ANTICYCLONES

The eddy track of ID0 passes very close to the Vema Seamount, a solitary feature that rises up to a distance of 35 m to the surface. This seamount is known to influence the pathways of Agulhas rings, often causing eddy splitting, as observed by Schouten et al. (2000). In this simulation, we observe strong interactions between the eddy and the seamount during the first three weeks of July 2019. These interactions are clearly visible in the vorticity field (Fig. 35), where small vortices are generated downstream in the lee of the seamount, forming a Kármán vortex street that is advected with the rotating eddy.

An analysis of the mean horizontal kinetic energy, evaluated at a single depth level, reveals a significant reduction of approximately one-third over three weeks (not shown). This indicates a substantial energy transfer into smaller-scale eddies and potentially also into internal waves in regions with vertical density stratification. Additionally, the interaction between the eddy and the seamount leads to intense mixing, causing the mixed layer depth to merge with the depth of the pycnocline, as illustrated in Fig. 34. Given that the eddy penetrates nearly the entire water column, we expect a range of dynamic processes to occur at different layers, including the mixed layer, the pycnocline, and the deep ocean.

It is worth noting that other eddy tracks also interact with bathymetric features. For example, Eddy ID5 crosses the Walvis Ridge, which rises to a depth of 1400 m (Fig. 38). However, this interaction differs from that of the Vema Seamount due to two key factors: (1) the eddy's velocities are concentrated primarily in the upper

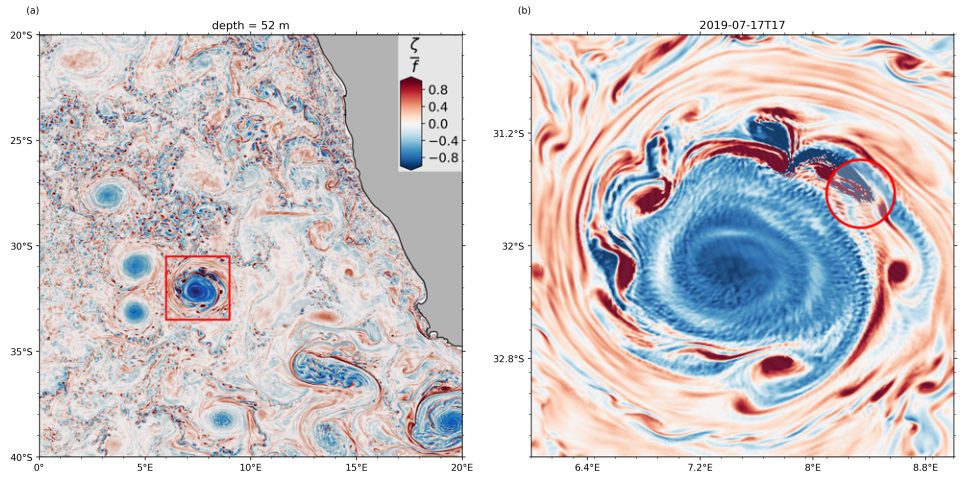

Figure 35: Snapshot of the relative vorticity divided by the planetary vorticity (ζ/f) at 52 m depth. The zoom in panel (b) on Eddy ID0 reveals a Kármán strait generated in the lee of the eddy rim current hitting a seamount named 'Vema' crest. The Vema crest at the upper right part of the eddy extents up to 35 m below the surface (indicated with a red circle)

400 m, and (2) the ridge topography is elongated, whereas the Vema Seamount is more cylindrical, which plays a critical role in the formation of the vortex street.

4.4.1 *Impact on the eddy spectra*

To evaluate how the eddies and their interactions with bathymetry influence variability, we analyze the spectra of several single eddies with and without topographic interaction. Therefore, we apply the derivation of spectral estimates described in Chap. 3 to only those points containing eddies and to those points without eddy activity. To isolate the eddy signal from the background flow, we apply a spatial mask to the eddy composite. This mask encompasses a one-degree radius around the eddy core, referred to as the 'inside' of the eddy. The mask is then inverted to define the 'outside' region, representing the background flow. Using the two-month time series of the composite, we compute the kinetic energy spectra both inside and outside the eddy. This allows for a detailed comparison of energy distributions within the eddy core and the surrounding background flow.

In Fig. 36, we present the kinetic energy spectra for regions inside and outside the eddy, comparing scenarios with and without topographic interaction. The spectrum of eddy ID5 (Fig. 36a) thereby appears to be characteristic for all six evaluated anticyclones that do not show an interaction with the topography as strong as that of ID0. Energy levels inside these eddies are significantly enhanced at mid and high frequencies compared to the background ('outside' the eddy). This pattern holds down to depths of about 1300 m; below this depth, the spectra inside the eddies become increasingly similar to the spectra outside of the eddies. Interestingly, energy is enhanced across the entire frequency spectrum within the eddies, rather than being concentrated at their characteristic frequency, $f_{eddy} = 1/2(\partial_x v - \partial_y u)$ (Kunze, 1985) where u and v are the zonal and meridional velocities, respectively. Moreover, we do not observe a pronounced shift in the effective frequency, defined

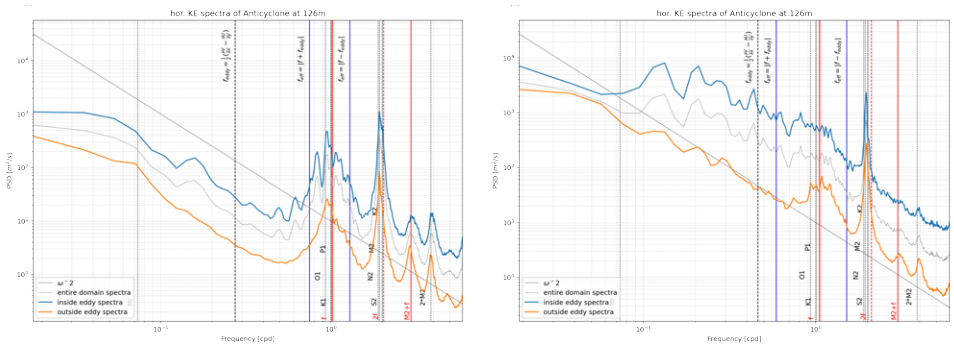

Figure 36: Kinetic energy spectra inside and outside of the eddy, with Eddy ID5 (left) and eddy ID0 (right; see Fig. 33 for the individual eddy tracks). Note that Eddy ID0 is strongly interacting with the bathymetry (Fig. 35). The vertical structure of of the stratification and kinetic energy for both eddies is shown in Fig. 34. Tidal peaks, near inertial peaks, their sub-harmonics and eddy frequencies are indicated by vertical lines. The black dashed line indicates a -2 spectral slope.

as with the zonal and meridional velocity u, v, respectively, or a strong impact on the effective frequency $f_{eff} = f + f_{eddy}$ suggesting that eddy dynamics influence the spectral distribution more broadly rather than solely modifying specific frequency bands. Notably, tidal peaks are also enhanced within the eddy, possibly indicating enhanced tidal wave activity. Despite these energy enhancements, the slope of the kinetic energy spectra remains largely unaffected by the presence of the eddies.

Eddy ID0 undergoes an intense bathymetry interaction, shown in Fig. 36b, and exhibits a significant shift across all energy levels, which is $\mathcal{O}(1-2)$ orders larger than the shift observed in EddyID5. Aside from the semi-diurnal peak, tidal peaks are barely visible. Instead, the energy appears to be distributed across all scales, following a slope of approximately -2. We speculate that the interaction between the eddy and the seamount triggers various processes such as mixing, submesoscale eddies and wave generation. These processes likely result in a nearly continuous energy spectrum, obscuring signals at specific frequencies associated with wave generation.

An inspection of the ID0 energy spectrum for the time period after ID0 has passed Vema crest, reveals that the energy spectrum of the eddy after the interaction closely resembles that of Eddy ID5 (not shown). This suggests that the seamount interaction enhances the energy cascade, particularly amplifying intermediate and high-frequency components. However, this enhanced energy rapidly diminishes once the eddy moves away from the seamount (not shown).

The coordinate transformation used to generate the eddy composites may introduce a Doppler shift; however, we argue that this effect is minimal, as the eddies translate slowly. A potentially more significant source of Doppler shifting arises from relatively fast advection (Ferrari and Wunsch, 2009; Delpech et al., 2024), such as eddy rotation. Here, the strong circular currents within the eddy may contribute to frequency shifts in the spectra. However, when comparing spectra computed 'inside' the eddy (fast velocities) with those 'outside' (slow velocities), we do not observe a frequency shift, particularly when examining the positions of tidal peaks. This suggests that Doppler shift is not dominant in our spectral esti-

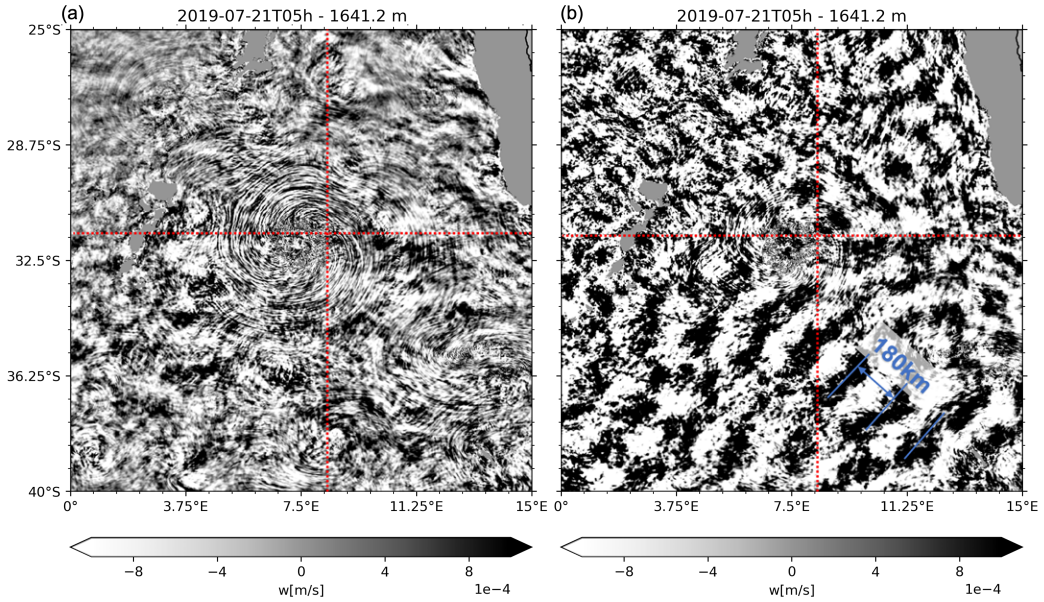

Figure 37: Snapshots of vertical velocity from ICON-SMT (a) and ICON-SMT-Wave (b) at 1641 m. Red line indicate zonal and meridional section crossing the location of seamount Vema at 8.36°E and 31.60°W.

mates. For a broader discussion on Doppler shift contamination, see (Ferrari and Wunsch, 2009).

4.5 IMPACT OF EDDY-BATHYMETRY INTERACTION ON THE WAVE FIELD

In the previous section, we observed that eddies can generate small-scale vortices when interacting with topography. Here, we examine topographically generated waves caused by a passing anticyclone, which is likely given that eddy tracks frequently cross both small and large topographic features, see Fig. 33.

4.5.1 *Eddies can stimulate waves*

To pinpoint wave generation types and locations, we analyze vertical velocities at 1641 m of both model configurations, see Fig. 37. The anticyclone IDo is placed in the center, here shown at a time step, where the seamount Vema is inside the eddy, see the red cross in Fig. 37 and Fig. 35. The figure captures overlapping large- and small-scale patterns, suggesting multiple interacting processes across different scales.

In ICON-SMT (left panel of Fig. 37), large-scale background waves propagate from southwest to northeast. These waves have a frequency which matches the near inertial frequency at 43°S and thus are most likely generated from storms in the Southern Ocean. In contrast, in the tidally forced configuration ICON-SMT-Wave (Fig. 37b), the dominant wave signal consists of waves originating from the Walvis Ridge and moving southeast. A distinct tidal beam with a wavelength of approximately 180 km aligns well with observations and storm tide simulations

(see Müller et al., 2012, and see Fig. 37b). It is the M2 tide with a semi-diurnal frequency. Snapshots across the water column reveal that these large wave patterns are particularly strong between 1500 m and 2000 m.

On a smaller scale, we observe circular wave patterns radiating outward from Eddy ID0 (Fig. 37a). These waves propagate away from the eddy, appearing throughout the water column. They also appear in the mixed layer, however with significantly weaker amplitude (not shown). These smaller waves originating from the eddy rim, can also be found in the tidally forced configuration ICON-SMT-Wave. Although here, they are more difficult to identify in the strong background wave field dominated by the M2 tides (e.g. slightly below the red cross at 32.6° Fig. 37b).

Eddy ID0 undergoes a strong interaction with the Vema seamount, as discussed above and indicated in Fig. 35b. Waves appear to be generated primarily downstream of the seamount, where they are advected by the eddy currents while continuing to propagate outward (towards the west starting from seamount Vema, along the zonal section indicates with a red line Fig. 37a). This wave signal is particularly pronounced during the three weeks when the eddy is directly interacting with the seamount, as in this snapshot. Interestingly, other eddies also exhibit similar wave generation, for example see the circular pattern in the upper left corner of Fig. 37a or close to the young Agulhas Ring with an elliptic shape in the lower right corner Fig. 37a and Fig. 35a. For instance, eddies ID5 and ID1 produce comparable wave patterns when crossing the Walvis Ridge (not shown in this snapshot). Eddy ID0 also continues to cause these waves after it passed the Vema crest at a later stage of the simulation (not shown). However, in the latter examples, the waves are significantly weaker, likely due to shallower bathymetry and weaker eddy currents at these depths, see Fig. 34.

4.5.2 *Wave patterns in layers of enhanced stratification*

The eddies and the above mentioned wave signals can also be identified from the vertical temperature gradient (see Fig. 38 for a section around the Walvis Ridge and Vema seamount).

Note that in this figure, eddy ID5 is sliced roughly in the center, while eddy ID1 is sliced at the outer rim, see Fig. 33. Several stratified layers are evident: (1) a thin band with an enhanced temperature gradient at approximately 100 m indicates the mixed layer base; (2) a broader, deeper layer with enhanced temperature gradient represents the main pycnocline. The latter is stretched within the eddies. Finally, we find (3) an additional region of enhanced stratification around 4200 m depth. A snapshot taken a month later shows the eddies advancing toward the Walvis Ridge, with eddy ID5 crossing the ridge and eddy ID0 moving away from the seamount. At this point, eddy ID0 is sliced near its center, while eddy ID5 is cut at its outer rim, see Fig. 33.

The seamount has a strong influence on the stratification of Eddy ID0, leading to intense mixing, indicated by enhanced turbulent kinetic energy (not shown) and a significantly deeper mixed layer compared to Eddy ID5, see Fig. 38a. An animation of the section reveals wave dynamics across multiple scales, including fluctuations of approximately 50 m at the mixed layer base, at the pycnocline and in other stratified layers, such as a distinct layer at 4200 m depth, highlighting active wave

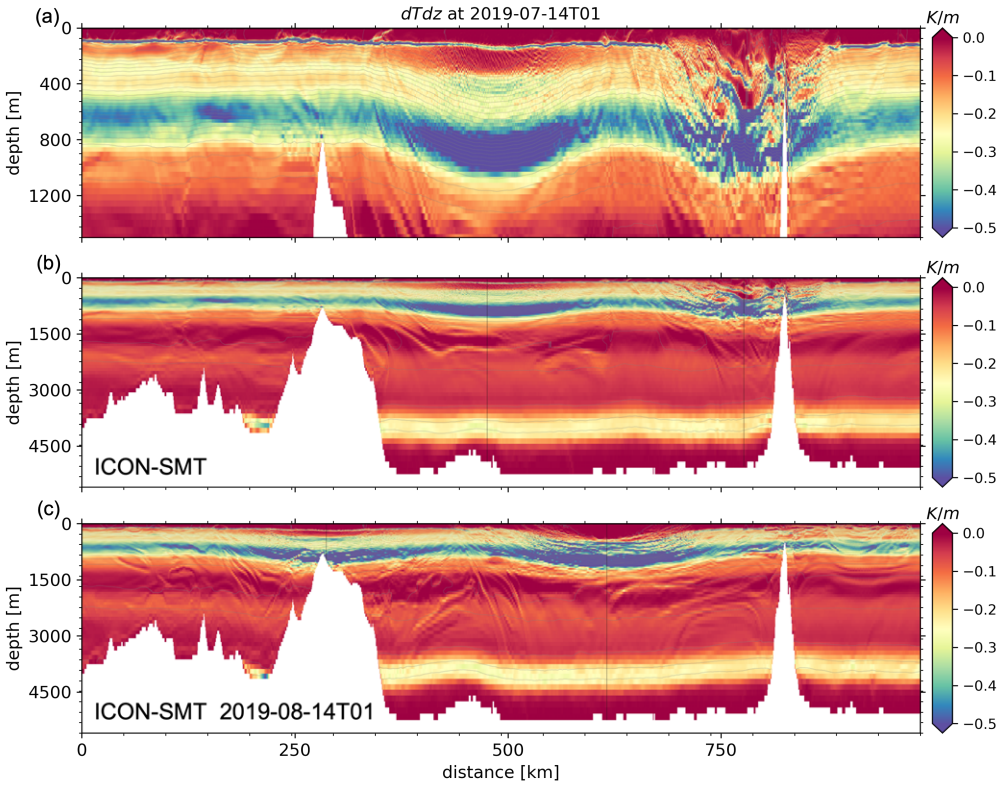

Figure 38: Snapshot of vertical temperature gradient for a section through the Walvis Ridge and two anticyclones (ID0 and ID5). The section is crossing the Vema seamount. A zoom from the surface to 1500 m (a) is shown along a full depth section during interaction with the seamount (b) and a month later (c). Isotherms are indicated with contour plots. The eddy positions are indicated with black vertical lines. The Eddy closer to the Walvis Ridge has ID5 and closer to mount Vema ID0, see also corresponding tracks in Fig. 33.

processes. Notably, wave patterns propagate outward from the eddy rims, particularly below the mixed layer and above 1000 m depth, in both eddies and in both directions (as shown in Fig. 38). These patterns correspond to the smaller waves observed in Fig. 37a. In the section depicting the vertical temperature gradient, these waves become particularly evident within layers of enhanced stratification, see the diamond pattern between the two eddies in Fig. 38a.

These wave patterns can also be inferred from vertical velocity, shown along the same section, see Fig. 39. An additional analysis of the vertical velocity field at two different time steps further illustrates the profound impact of eddies on the dynamics throughout the entire water column (Fig. 39). The strongest velocities are observed between 1500 m and 3500 m and near the seamounts, with the former indicating the baroclinicity of the flow. Notably, nearly vertical stripes appear throughout the water column at the eddy rims, particularly pronounced in Fig. 39b. The location of these vertical stripes coincides with the intense eddy velocities at the eddy rim. The topography and the flow thus generate these strong velocities, which extend throughout the water column.

The comparison between ICON-SMT and ICON-SMT-Wave shows significantly stronger vertical velocities throughout the water column in the tidally forced model

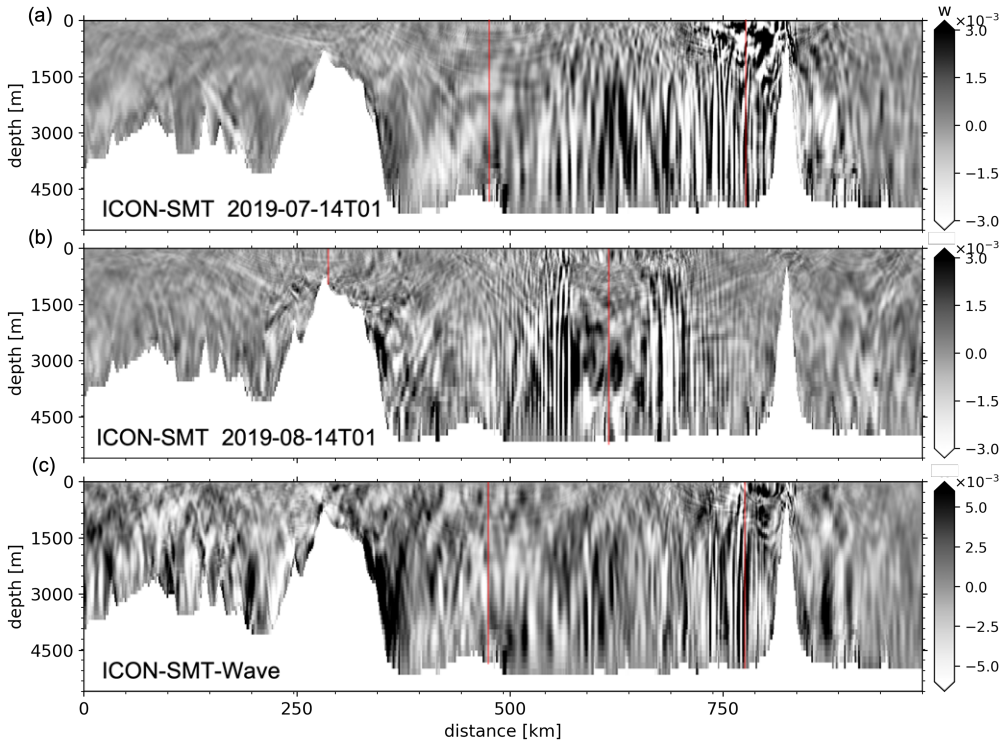

Figure 39: A snapshot of the vertical velocity section through the Walvis Ridge and two anticyclones (ID0 and ID5). The section is shown for ICON-SMT and ICON-SMT-Wave at the same time step, a and c respectively. And an additional snapshot of ICON-SMT is given a month later (b). The section is crossing the Vema seamount. Note the adapted color limits for ICON-SMT-Wave. The eddy positions are indicated with vertical red lines.

(Fig. 39a and c). The vertical velocity indicates that internal waves are reflected near the surface. This pattern shows strong similarities to idealised simulations of internal tide generation at a ridge, see e.g. (Musgrave et al., 2022).

4.5.3 *Hovmöller Plots*

To investigate the waves generated by the eddy-seamount interaction, we present both zonal and meridional Hovmöller plots for the ICON-SMT and ICON-SMT-Wave models in Fig. 40. The sections are indicated with red lines in Fig. 37. Additionally, we include the longitude and latitude of the core of Eddy ID0, tracked in Fig. 33, showing its movement toward the Northwest. We observe strong perturbations in the velocity field, highlighting the region of the highest eddy velocities, roughly between 1° - 1.6° longitude, which coincides with the region of maximum kinetic energy at 1641 m (Fig. 34). The Hovmöller plots reveal stripes with varying inclinations, which may suggest different wave propagation speeds (fast vs. slow).

NEAR INERTIAL WAVES The steeper stripes, marked with green lines in Fig. 40c, have a period of 9 cycles over 7 days. The phase indicates northeastward propagation, which aligns with the findings from the animation and also Fig. 37a. The frequency is slightly larger than the local near-inertial frequency (NIW) at 32°S.

From the frequency and propagation direction of these NIWs, we derive that they must originate from the Southern Ocean at roughly 43°S – a location with strong storm activity. In the tidally forced model, the NIW signal is superimposed by the tidal wave signal. From the inclination of the wave fronts, we infer a south-eastward propagation of the waves, which is also consistent with the observations from Fig. 37a.

STEADY LEE WAVES The Hovmöller diagram also indicates a standing wave pattern (visible as horizontal stripes that remain fixed in location for approximately two weeks; see purple arrow in Fig. 40). As discussed above, this signal corresponds to a standing wave that is caused by the eddy swirl velocity interacting with the local bathymetry. It can also be identified from an animation of Fig. 37 (not shown). Such standing waves have also been reported in previous studies, e.g. topographically-generated internal waves over the Charleston Bump in the Gulf Stream (Marez et al., 2020a). Notably, the standing wave emerges only when eddy ID0 is nearby, indicating that it is induced by the eddy rather than the background flow.

LEE WAVES In addition to the NIW signal, we observe waves originating from the eddy rim propagating outwards in all directions (indicated by blue lines in Fig. 40). These waves correspond directly to those observed in Fig.37a and Fig.38, reinforcing our assumption that they are lee waves. On top of these larger beams, we also detect a smaller wave pattern traveling along the individual beams, indicated by yellow arrows in Fig. 40. However, it remains unclear whether these patterns represent real waves or are artifacts arising from interference or other model limitations, particularly when considering the temporal and spatial resolution constraints of the model.

GEOSTROPHIC ADJUSTMENT Internal waves can originate from geostrophic adjustment, a process in which the ocean responds to an initial imbalance by generating waves and adjusting to a new equilibrium state. In our simulation, all state variables that are required to provide an initial state of ICON-SMT are interpolated from the coarser simulation of ICON-R2B9. Since this includes an interpolation of the horizontal velocities, it can be assumed that those are largely in agreement with the pressure field but also with the local forcing conditions. However, certain features, such as the transition from coarse to fine bathymetry, may still induce adjustment effects. An animation of the vertical velocity field at 1641 m shows indeed some fast adjustment processes in the form of fast gravity waves. These waves originate, however, rather from bathymetric obstacles than from characteristic flow patterns like eddies. Notably, eddies such as ID5 do not emit waves during the initial phase, indicating that their structure remains largely unaffected by the geostrophic adjustment process.

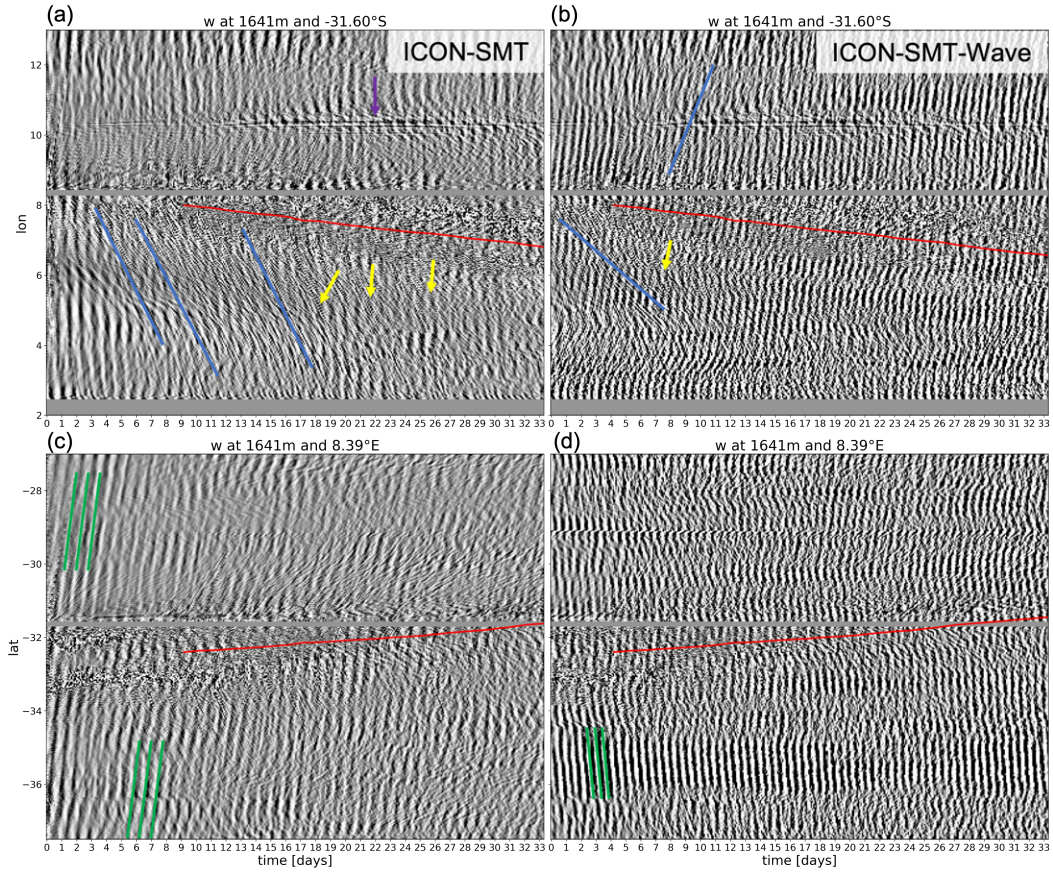

Figure 40: Snapshots of vertical velocity from ICON-SMT (left) and ICON-SMT-Wave (right) at 1641 m. The time series is illustrated as zonal (upper) and meridional (lower) Hovmöller plots. Sections are chosen to intersect the Vema Seamount at 8.39°E, 31.60°S. The red line in the center of the plot marks the eddy center, detected using an eddy tracking algorithm (see Fig. 33). Vema seamount is visible as a grey bar in the middle of the figure. The Walvis Ridge can also be seen at 2°E in zonal section (upper). Green lines highlight wave patterns with a period of approximately 9–10 cycles per 7 days. The blue line denotes a wave pattern with significantly higher frequencies. Yellow arrows point to wave patterns visible on striped structures. Note that the time series of ICON-SMT-Wave is starting 6 days after ICON-SMT and ends also 6 days later. Note that the ICON-SMT time series starts with initialization from a coarser model run, and we assume a robust spin-up after two weeks. The same colorbar is applied as in Fig. 39a.

4.6 CONCLUSION

This study examines mesoscale oceanic eddies and their impact on ocean variability in the Agulhas Ring Path near the Walvis Ridge, using a submesoscale-resolving ICON configuration. By applying an eddy tracking algorithm, we compile four-dimensional datasets of six anticyclones, enabling a detailed analysis of their evolution and influence. While propagating through the Cape Basin, the eddies have a dominant influence on velocity and stratification throughout the water column. Spectral analysis of the composites reveal, that the energy levels are 1-2 orders of magnitude higher within the eddy than the background.

We observe multiple eddy-bathymetry interactions, including three eddies crossing the Walvis Ridge and one interacting with the Vema Seamount, a solitary peak rising to 35 m below sea level. These interactions significantly impact ocean variability, stratification, and the wave field. The Vema Seamount interaction, in particular, leads to strong reduction in eddy kinetic energy over a month and an increase in mixed layer depth from 100 m to 400 m. This event also generates a striking Kármán vortex street with alternating vorticity patches.

Additionally, bathymetric interactions induce wave generation, with propagating wave patterns visible in vertical velocity snapshots and Hovmöller plots. These waves, including lee waves, extend from the mixed layer to deeper stratified layers (e.g., 4200 m depth) and are present in both ICON-SMT and ICON-SMT-Wave simulations. Multiple eddies (ID0, ID5, and ID1) generate similar wave patterns when interacting with the Walvis Ridge, highlighting the widespread influence of eddy-topography interactions.

Finally, as eddies traverse the Cape Basin, standing wave patterns emerge in animations and Hovmöller plots, indicating persistent wave features.

We summarize the key conclusions as follows:

- Formation of Kármán vortex street with patches of positive and negative vorticity advected by the eddy swirl
- The interaction of the eddies with Vema Seamount and the Walvis ridge modifies the stratification, particularly in the mixed layer and pycnocline and beyond.
- Spectral analysis of the composites reveal, that the energy levels are 1-2 orders of magnitude higher within the eddy than the background. The energy levels are even more enhanced within an eddy that interacts with the Vema seamount.
- We observe topographically generated waves produced by Agulhas rings as they cross the Walvis Ridge and interact with the Vema Seamount. These waves propagate throughout the water column. Although weaker we also observe these waves when anticyclones cross the Walvis Ridge.
- Additionally, we identify lee waves in the form of standing waves, generated by the presence of the eddy.

This initial exploration highlights the potential of kilometer-scale models for evaluating small-scale ocean dynamics, such as the interaction of mesoscale-sub-

mesoscale eddies and internal waves, in a more complex and dynamically rich environment.

5

SUMMARY AND CONCLUSIONS

Wir möchten gerne die Welle kennen,
auf welcher wir im Ozean treiben,
allein wir sind diese Welle selbst.

— Jacob Burckhardt, 1867

In this thesis, 'Kilometer-Scale Ocean Turbulence and Waves in the North and South Atlantic', we explore mixed layer instabilities and internal waves using a novel telescoping model with continuous grid refinement to achieve unprecedented resolution.

We demonstrated that both applications of the novel ICON-SMT configuration can successfully reproduce geostrophic turbulence, as validated against the latest remote sensing techniques, such as SWOT, as well as in situ observations from our concurrent observational campaign. Spectral analysis of frequency and wavenumber spectra of sea surface height (SSH) and kinetic energy revealed a remarkable agreement with observations. However, we note that observational datasets remain too coarse to fully evaluate the model at its finest resolved scales. Our results highlight that once submesoscale processes are resolved in ocean models, variability increases not only at the kilometer scale of submesoscale eddies but also at larger scales. This enhanced variability improves agreement with both established and novel satellite and in situ observations compared to coarser model configurations. We further demonstrated that ICON-SMT-Wave is able to resolve a large fraction of the internal wave field.

We employed this model in the North and South Atlantic to find answers for three research questions:

How well do theoretical estimates and parameterizations capture the restratification of mixed layer fronts by submesoscale instabilities in a kilometer-scale ocean simulation with realistic forcing?

We have successfully demonstrated that our model configuration can resolve mixed layer submesoscale eddies. Once these processes are resolved, submesoscale eddies drive the overturning of ocean fronts, resulting in frontal re-stratification and a downward buoyancy flux, which is in agreement with theoretical predictions and results from idealized simulations. To quantify this, we identified and analyzed 45 fronts, calculating the eddy-induced overturning and re-stratification through their associated buoyancy fluxes. Mixed layer eddy parameterizations can capture the effect of the mixed layer overturning within an accuracy that lies within an order of magnitude. We further analyzed whether submesoscale eddies form at the rim of mesoscale eddies and to what extent parameterizations capture their

impact. Overall, the eddies experience less re-stratification along the eddy rim than suggested by the parameterizations.

What impact do mixed layer eddies and tides have on high-frequency ocean dynamics?

Our results show that submesoscale dynamics are crucial for achieving improved energy levels at intermediate scales and for obtaining a -2 spectral slope, consistent with ADCP observations. In contrast, comparisons with SWOT reveal a consistent -11/3 slope in the SSH wavenumber spectra across both model configurations and observational data, highlighting the robustness of this spectral characteristic in sea surface height variability. The frequency-wavenumber spectra confirm that we resolve a considerable portion of the internal wave band, successfully representing the first three baroclinic modes.

We demonstrated that tidal dynamics play a crucial role in shaping the energy distribution at the high-frequency end of the SSH and KE spectra. Tidal forcing enhances the realism of the spectra by reproducing expected tidal peaks and subharmonics while also injecting energy into intermediate frequencies, suggesting that wave-wave interactions are key to the spectral energy distribution. However, the model overestimates spectral peaks while underestimating energy levels between them. This effect is significantly reduced in ICON-SMT-Wave but remains more pronounced in the coarser ICON-R2B9-Wave configuration. These findings suggest that both configurations lack some degree of wave-wave interactions, with the deficiency being more severe in the lower-resolution model.

What is the influence of mesoscale eddies and their interaction with bathymetry on high-frequency variability? Which role do topographically-generated internal waves play here?

We employed a novel methodology to assess the influence of mesoscale eddies on ocean variability. By combining an eddy tracking algorithm with composite analysis on the high-resolution data from the high-resolution configurations ICON-SMT-Wave with tidal forcing, ICON-SMT without tidal forcing and the coarser resolved ICON-R2B9-Wave with tidal forcing, we examined their behavior and variability, including horizontal kinetic energy spectra. Spectral analysis of the composites reveals that energy levels within eddies are 1–2 orders of magnitude higher than the surrounding background, with a significant increase during interactions with the Vema Seamount. We demonstrate, that a portion of this energy is transferred into the generation of internal waves. We further observed topographically-generated internal waves as Agulhas rings cross the Walvis Ridge, with these waves propagating throughout the entire Cape Basin.

Next Steps: This chapter represents an initial exploration, and further investigations are planned. Specifically, we aim to leverage our model configurations

with and without tidal forcing to better quantify the energy transferred to Lee waves and estimate the contribution of tidal waves. Additionally, we plan to assess whether Lee wave generation by mesoscale eddies can be identified within our two year observational datasets.

Kilometer-scale models showcase impressive capabilities, but this thesis also showed where those model still have limitations. For example, their short run times may lead to uncertainties in attributing fluxes to specific processes or model drift. Technical constraints also hinder the ability to assess the impact of mixed layer eddies on subdecadal or decadal timescales. While the resolution is sufficient for resolving mixed layer instabilities under winter conditions, it struggles with thin mixed layers and cannot fully capture the required dynamical range. Additionally, the coarse atmospheric forcing limits realism by missing high-frequency wind motions and related wave generation. However, ongoing development of coupled kilometer-scale models may soon address these challenges. Overall, these models represent a significant step forward in ocean simulations, enabling new research, but still face technical and dynamical limitations. We also look forward to future SWOT datasets with reduced noise and other observational campaigns, which will allow for more detailed evaluations on smaller scales.

I hope that these findings contribute to improve our understanding of mixed layer instabilities and waves in kilometer-scale ocean models. May this small step help refine ocean and ultimately climate models, guiding us forward on our voyage that never ends.

BIBLIOGRAPHY

Andrews, D G, J R Holton, and C B Leovy (Jan. 1987). *Middle atmosphere dynamics*. Academic Press Inc.,Orlando, FL. URL: https://www.osti.gov/biblio/5936274.

Andrews, D. G. and M. E. McIntyre (1976). "Planetary Waves in Horizontal and Vertical Shear: the Generalized Eliassen-Palm Relation and the Mean Zonal Acceleration." In: 33.11, pp. 2031–2048. ISSN: 00224928. DOI: 10.1175/1520-0469(1976)033<2031:PWIHAV>2.0.CO;2.

— (1978). "Generalized Eliassen-Palm and Charney-Drazin Theorems for Waves on Axismmetric Mean Flows in Compressible Atmospheres." In: *Journal of Atmospheric Sciences* 35.2, pp. 175 –185. DOI: 10.1175/1520-0469(1978)035<0175:GEPACD>2.0.CO;2. URL: https://journals.ametsoc.org/view/journals/atsc/35/2/1520-0469_1978_035_0175_gepacd_2_0_co_2.xml.

Arbic, Brian K. (2022). "Incorporating tides and internal gravity waves within global ocean general circulation models: A review." In: *Progress in Oceanography* 206.May, p. 102824. ISSN: 00796611. DOI: 10.1016/j.pocean.2022.102824. URL: https://doi.org/10.1016/j.pocean.2022.102824.

Aviso-C3S (2021). *Global Ocean Gridded L4 Sea Surface Heights and Derived Variables Reprocessed*. Accessed: 2025-01-03. DOI: 10.48670/moi-00145. URL: https://doi.org/10.48670/moi-00145.

Bartello, Peter (1995). "Geostrophic adjustment and inverse cascades in rotating stratified turbulence." In: *Journal of the atmospheric sciences* 52.24.

Beal, Lisa M. et al. (2011). "On the role of the Agulhas system in ocean circulation and climate." In: *Nature* 472.7344, pp. 429–436. ISSN: 00280836. DOI: 10.1038/nature09983.

Bell, T. H. (1975). "Topographically generated internal waves in the open ocean." In: *Journal of Geophysical Research* 80.3, pp. 320–327. DOI: 10.1029/jc080i003p00320.

Biastoch, A. et al. (2009). "Increase in Agulhas leakage due to poleward shift of Southern Hemisphere westerlies." In: *Nature* 462.7272, pp. 495–498. ISSN: 00280836. DOI: 10.1038/nature08519.

Boccaletti, Giulio, Raffaele Ferrari, and Baylor Fox-Kemper (2007). "Mixed layer instabilities and restratification." In: *Journal of Physical Oceanography* 37.9, pp. 2228–2250. ISSN: 00223670. DOI: 10.1175/JPO3101.1.

Bodner, Abigail S. et al. (2023). "Modifying the Mixed Layer Eddy Parameterization to Include Frontogenesis Arrest by Boundary Layer Turbulence." In: *Journal of Physical Oceanography* 53.1, pp. 323–339. ISSN: 15200485. DOI: 10.1175/JPO-D-21-0297.1.

Boyer Montégut C., de (2023). "Mixed layer depth climatology computed with a density threshold criterion of 0.03kg/m3 from 10 m depth value." In: *SEANOE*. DOI: 10.17882/91774.

Brannigan, Liam et al. (2017). "Submesoscale instabilities in mesoscale eddies." In: *Journal of Physical Oceanography* 47.12, pp. 3061–3085. ISSN: 15200485. DOI: 10.1175/JPO-D-16-0178.1.

Brüggemann, Nils and Carsten Eden (2014). "Evaluating Different Parameterizations for Mixed Layer Eddy Fluxes induced by Baroclinic Instability." In: *Journal of Physical Oceanography* 44.9, pp. 2524–2546. ISSN: 0022-3670. DOI: 10.1175/JPO-D-13-0235.1. URL: http://journals.ametsoc.org/doi/10.1175/JPO-D-13-0235.1.

— (2015). "Routes to dissipation under different dynamical conditions." In: *Journal of Physical Oceanography* 45.8, pp. 2149–2168. ISSN: 15200485. DOI: 10.1175/JPO-D-14-0205.1.

Brunner-Suzuki, Anne Marie E.G., Miles A. Sundermeyer, and M. Pascale Lelong (2014). "Upscale energy transfer by the vortical mode and internal waves." In: *Journal of Physical Oceanography* 44.9, pp. 2446–2469. ISSN: 15200485. DOI: 10.1175/JPO-D-12-0149.1.

Bühler, Oliver, Max Kuang, and Esteban G. Tabak (2017). "Anisotropic Helmholtz and wave-vortex decomposition of one-dimensional spectra." In: *Journal of Fluid Mechanics* 815, pp. 361–387. ISSN: 14697645. DOI: 10.1017/jfm.2017.57.

Bühler, Oliver and Michael E. McIntyre (2005). "Wave capture and wave-vortex duality." In: *Journal of Fluid Mechanics* 534, pp. 67–95. ISSN: 00221120. DOI: 10.1017/S0022112005004374.

Bühler, Oliver (2014). *Waves and Mean Flows*. 2nd ed. Cambridge Monographs on Mechanics. Cambridge University Press.

Callies, Jörn and Raffaele Ferrari (2018a). "Baroclinic instability in the presence of convection." In: *Journal of Physical Oceanography* 48.1, pp. 45–60. ISSN: 15200485. DOI: 10.1175/JPO-D-17-0028.1.

— (2018b). "Note on the rate of restratification in the baroclinic spindown of fronts." In: *Journal of Physical Oceanography* 48.7, pp. 1543–1553. ISSN: 15200485. DOI: 10.1175/JPO-D-17-0175.1.

Callies, Jörn et al. (2015). "Seasonality in submesoscale turbulence." In: *Nature Communications* 6, pp. 1–8. ISSN: 20411723. DOI: 10.1038/ncomms7862.

Calvert, Daley et al. (2020). "The impact of a parameterisation of submesoscale mixed layer eddies on mixed layer depths in the NEMO ocean model." In: *Ocean Modelling* 154.August 2019, p. 101678. ISSN: 14635003. DOI: 10.1016/j.ocemod.2020.101678. URL: https://doi.org/10.1016/j.ocemod.2020.101678.

Cao, Haijin and Zhiyou Jing (2022). "Submesoscale Ageostrophic Motions Within and Below the Mixed Layer of the Northwestern Pacific Ocean." In: *Journal of Geophysical Research: Oceans* 127.2, pp. 1–22. ISSN: 21699291. DOI: 10.1029/2021JC017812.

Capet, Xavier et al. (2008a). "Mesoscale to submesoscale transition in the California Current system. Part I: Flow structure, eddy flux, and observational tests." In: *Journal of Physical Oceanography* 38.1, pp. 29–43. ISSN: 00223670. DOI: 10.1175/2007JPO3671.1.

— (2008b). "Mesoscale to submesoscale transition in the California current system. Part III: Energy balance and flux." In: *Journal of Physical Oceanography* 38.10, pp. 2256–2269. ISSN: 00223670. DOI: 10.1175/2008JPO3810.1.

Casanova-Masjoan, M. et al. (2017). "Characteristics and evolution of an Agulhas ring." In: *Journal of Geophysical Research: Oceans* 122.9, pp. 7049–7065. ISSN: 2169-9275. DOI: 10.1002/2017JC012969. URL: https://agupubs.onlinelibrary.wiley.com/doi/10.1002/2017JC012969.

Chassignet, Eric P. and David P. Marshall (2008). "Gulf stream separation in numerical ocean models." In: *Geophysical Monograph Series* 177, pp. 39–61. ISSN: 23288779. DOI: 10.1029/177GM05.

Chassignet, Eric P. et al. (2020). "Impact of horizontal resolution on global ocean-sea ice model simulations based on the experimental protocols of the Ocean Model Intercomparison Project phase 2 (OMIP-2)." In: *Geoscientific Model Development* 13.9, pp. 4595–4637. ISSN: 19919603. DOI: 10.5194/gmd-13-4595-2020.

Chelton, Dudley B. et al. (1998). "Geographical variability of the first baroclinic Rossby radius of deformation." In: *Journal of Physical Oceanography* 28.3, pp. 433–460. ISSN: 00223670. DOI: 10.1175/1520-0485(1998)028<0433:GVOTFB>2.0.CO;2.

Chouksey, Manita, Carsten Eden, and Nils Brüggemann (2018). "Internal gravity wave emission in different dynamical regimes." In: *Journal of Physical Oceanography* 48.8, pp. 1709–1730. ISSN: 15200485. DOI: 10.1175/JPO-D-17-0158.1.

Chouksey, Manita et al. (2023). "A comparison of methods to balance geophysical flows." In: *Journal of Fluid Mechanics* 971, A2. ISSN: 0022-1120. DOI: 10.1017/jfm.2023.602. URL: https://www.cambridge.org/core/product/identifier/S002211202300602X/type/journal_article.

Chrysagi, Evridiki et al. (2021). "High-Resolution Simulations of Submesoscale Processes in the Baltic Sea: The Role of Storm Events." In: *Journal of Geophysical Research Oceans* 126.3. ISSN: 21699291. DOI: 10.1029/2020JC016411.

Danilov, S. (2022). "On the Resolution of Triangular Meshes." In: *Journal of Advances in Modeling Earth Systems* 14.10, pp. 1–7. ISSN: 19422466. DOI: 10.1029/2022MS003177.

D'Asaro, E. A. and Henry Perkins (1984). "A Near-Inertial Internal Wave Spectrum for the Sargasso Sea in Late Summer." In: *Journal of Physical Oceanography* 14.3, pp. 489–505. ISSN: 0022-3670. DOI: 10.1175/1520-0485(1984)014<0489:ANIIWS>2.0.CO;2. arXiv: arXiv:1011.1669v3. URL: http://journals.ametsoc.org/doi/10.1175/1520-0485(1984)014%3C0489:ANIIWS%3E2.0.CO;2.

de Boyer Montégut, Clément (2004). "Mixed layer depth over the global ocean: An examination of profile data and a profile-based climatology." In: *Journal of Geophysical Research* 109.C12, p. C12003. ISSN: 0148-0227. DOI: 10.1029/2004JC002378. URL: http://doi.wiley.com/10.1029/2004JC002378.

Delepoulle, Antoine et al. (Oct. 2022). *AntSimi/py-eddy-tracker: v3.6.1*. Version v3.6.1. DOI: 10.5281/zenodo.7197432. URL: https://doi.org/10.5281/zenodo.7197432.

Delpech, Audrey et al. (2024). "Eddy–Internal Wave Interactions and Their Contribution to Cross-Scale Energy Fluxes: A Case Study in the California Current." In: *Journal of Physical Oceanography* 54.3, pp. 741–754. ISSN: 15200485. DOI: 10.1175/JPO-D-23-0181.1.

Dong, Jihai et al. (2020a). "The scale of submesoscale baroclinic instability globally." In: *Journal of Physical Oceanography* 50.9, pp. 2649–2667. ISSN: 15200485. DOI: 10.1175/JPO-D-20-0043.1.

— (2020b). "The Seasonality of Submesoscale Energy Production, Content, and Cascade." In: *Geophysical Research Letters* 47.6, pp. 1–9. ISSN: 19448007. DOI: 10.1029/2020GL087388.

Dunphy, Michael and Kevin G. Lamb (2014). "Focusing and vertical mode scattering of the first mode internal tide by mesoscale eddy interaction." In: *Journal of Geophysical Research: Oceans* 119.1, pp. 523–536. ISSN: 21699291. DOI: 10.1002/2013JC009293.

Eady, E. T. (1949). "Long Waves and Cyclone Waves." In: *Tellus* 1.3, pp. 33–52. ISSN: 0040-2826. DOI: 10.3402/tellusa.v1i3.8507.

Eden, Carsten, Manita Chouksey, and Dirk Olbers (2019a). "Gravity wave emission by shear instability." In: *Journal of Physical Oceanography* 49.9, pp. 2393–2406. ISSN: 15200485. DOI: 10.1175/JPO-D-19-0029.1.

Eden, Carsten, Friederike Pollmann, and Dirk Olbers (2019b). "Numerical Evaluation of Energy Transfers in Internal Gravity Wave Spectra of the Ocean." In: *Journal of Physical Oceanography* 49.3, pp. 737–749. ISSN: 0022-3670. DOI: 10.1175/JPO-D-18-0075.1. URL: https://journals.ametsoc.org/view/journals/phoc/49/3/jpo-d-18-0075.1.xml.

Ferrari, Raffaele and Carl Wunsch (2009). "Ocean circulation kinetic energy: Reservoirs, sources, and sinks." In: *Annual Review of Fluid Mechanics* 41, pp. 253–282. ISSN: 00664189. DOI: 10.1146/annurev.fluid.40.111406.102139.

Fox-Kemper, B. et al. (2011). "Parameterization of mixed layer eddies. III: Implementation and impact in global ocean climate simulations." In: *Ocean Modelling* 39.1-2, pp. 61–78. ISSN: 14635003. DOI: 10.1016/j.ocemod.2010.09.002. URL: http://dx.doi.org/10.1016/j.ocemod.2010.09.002.

Fox-Kemper, Baylor, Raffaele Ferrari, and Robert Hallberg (2008). "Parameterization of mixed layer eddies. Part I: Theory and diagnosis." In: *Journal of Physical Oceanography* 38.6, pp. 1145–1165. ISSN: 00223670. DOI: 10.1175/2007JPO3792.1.

Garett, Chris and Eric Kunze (2007). "Internal tide generation in the deep ocean." In: *Annual Review of Fluid Mechanics* 39, pp. 57–87. ISSN: 00664189. DOI: 10.1146/annurev.fluid.39.050905.110227.

Garrett, Christopher and Walter Munk (1975). "Space-time scales of internal waves: A progress report." In: *Journal of Geophysical Research* 80.3, pp. 291–297. ISSN: 01480227. DOI: 10.1029/JC080i003p00291. URL: http://doi.wiley.com/10.1029/JC080i003p00291.

Gaspar, Philippe, Yves Grégoris, and Jean-Michel Lefevre (1990). "A simple eddy kinetic energy model for simulations of the oceanic vertical mixing: Tests at station Papa and long-term upper ocean study site." In: *Journal of Geophysical Research: Oceans* 95.C9, pp. 16179–16193. ISSN: 0148-0227. DOI: 10.1029/jc095ic09p16179.

Gent, Peter R. and James C. Mcwilliams (1990). "Isopycnal Mixing in Ocean Circulation Models." In: *Journal of Physical Oceanography* 20.1, pp. 150–155. ISSN: 0022-3670. DOI: 10.1175/1520-0485(1990)020<0150:IMIOCM>2.0.CO;2. URL: http://journals.ametsoc.org/doi/10.1175/1520-0485(1990)020%3C0150:IMIOCM%3E2.0.CO;2.

Gill, Adrian E. (1982). *Atmosphere-ocean dynamics*. Academic Press, New Nork.

Green, J. S. A. (1970). "Transfer properties of the large-scale eddies and the general circulation of the atmosphere." In: *Quarterly Journal of the Royal Meteorological Society* 96.408, pp. 157–185. ISSN: 0035-9009. DOI: 10.1002/qj.49709640802. URL: https://rmets.onlinelibrary.wiley.com/doi/10.1002/qj.49709640802.

Grooms, I. et al. (2021). "Diffusion-Based Smoothers for Spatial Filtering of Gridded Geophysical Data." In: *Journal of Advances in Modeling Earth Systems* 13.9, pp. 1–24. ISSN: 19422466. DOI: 10.1029/2021MS002552.

Guerra, Luiz Alexandre A., Guilherme N. Mill, and Afonso M. Paiva (2022). "Observing the spread of Agulhas Leakage into the Western South Atlantic by tracking mode waters within ocean rings." In: *Frontiers in Marine Science* 9, pp. 1–20. ISSN: 22967745. DOI: 10.3389/fmars.2022.958733.

Gula, Jonathan, Jeroen J. Molemaker, and James C. Mcwilliams (2014). "Submesoscale cold filaments in the Gulf Stream." In: *Journal of Physical Oceanography* 44.10, pp. 2617–2643. ISSN: 15200485. DOI: 10.1175/JPO-D-14-0029.1.

Gula, Jonathan et al. (Sept. 2021). "Submesoscale processes and mixing." In: todo, pp. 181–214. ISBN: 978-0-12-821512-8. DOI: 10.1016/B978-0-12-821512-8.00015-3.

Haine, Thomas W.N. and John Marshall (1998). "Gravitational, symmetric, and baroclinic instability of the ocean mixed layer." In: *Journal of Physical Oceanography* 28.4, pp. 634–658. ISSN: 00223670. DOI: 10.1175/1520-0485(1998)028<0634:GSABIO>2.0.CO;2.

Hasselmann, Klaus (1966). "Feynman diagrams and interaction rules of wave-wave scattering processes." In: *Reviews of Geophysics* 4.1, pp. 1–32.

Held, Isaac M. and Tapio Schneider (1999). "The surface branch of the zonally averaged mass transport circulation in the troposphere." In: *Journal of the Atmospheric Sciences* 56.11, pp. 1688–1697. ISSN: 00224928. DOI: 10.1175/1520-0469(1999)056<1688:TSBOTZ>2.0.CO;2.

Hersbach, H. et al. (2023). *ERA5 hourly data on single levels from 1940 to present*. DOI: 10.24381/cds.adbb2d47. URL: https://doi.org/10.24381/cds.adbb2d47.

Hohenegger, Cathy et al. (2023). "ICON-Sapphire: Simulating the components of the Earth system and their interactions at kilometer and subkilometer scales." In: *Geoscientific Model Development* 16.2, pp. 779–811. ISSN: 19919603. DOI: 10.5194/gmd-16-779-2023.

Holte, James et al. (2017). "An Argo mixed layer climatology and database." In: *Geophysical Research Letters* 44.11, pp. 5618–5626. ISSN: 19448007. DOI: 10.1002/2017GL073426.

Kara, A. Birol, Peter A. Rochford, and Harley E. Hurlburt (2000). "An optimal definition for ocean mixed layer depth." In: *Journal of Geophysical Research: Oceans* 105.C7, pp. 16803–16821. ISSN: 21699291. DOI: 10.1029/2000jc900072.

Klein, Patrice, Stefan Llewellyn Smith, and Guillaume Lapeyre (2004). "Organization of near-inertial energy by an eddy field." In: *Quarterly Journal of the Royal Meteorological Society* 130.598 PART A, pp. 1153–1166. ISSN: 00359009. DOI: 10.1256/qj.02.231.

Korn, P. et al. (2022). "ICON-O: The Ocean Component of the ICON Earth System Model—Global Simulation Characteristics and Local Telescoping Capability." In: *Journal of Advances in Modeling Earth Systems* 14.10, pp. 1–29. ISSN: 19422466. DOI: 10.1029/2021MS002952.

Korn, Peter (2017). "Formulation of an unstructured grid model for global ocean dynamics." In: *Journal of Computational Physics* 339, pp. 525–552. ISSN: 10902716. DOI: 10.1016/j.jcp.2017.03.009. URL: http://dx.doi.org/10.1016/j.jcp.2017.03.009.

Krug, Marjolaine, J. Tournadre, and F. Dufois (2014). "Interactions between the Agulhas Current and the eastern margin of the Agulhas Bank." In: *Continental Shelf Research* 81.June, pp. 67–79. ISSN: 02784343. DOI: 10.1016/j.csr.2014.02.020.

Kunze, Eric (1985). "Near-Inertial Wave Propagation In Geostrophic Shear." In: *Journal of Physical Oceanography* 15.5, pp. 544–565. ISSN: 0022-3670. DOI: 10.1175/1520-0485(1985)015<0544:NIWPIG>2.0.CO;2. URL: http://journals.ametsoc.org/doi/10.1175/1520-0485(1985)015%3C0544:NIWPIG%3E2.0.CO;2.

Lahaye, Noé, Jonathan Gula, and Guillaume Roullet (2019). "Sea Surface Signature of Internal Tides." In: *Geophysical Research Letters* 46.7, pp. 3880–3890. ISSN: 19448007. DOI: 10.1029/2018GL081848.

Lapeyre, Guillaume, Patrice Klein, and Bach Lien Hua (Aug. 2006). "Oceanic Restratification Forced by Surface Frontogenesis." In: *Journal of Physical Oceanography* 36.8. Publisher: American Meteorological Society, pp. 1577–1590. ISSN: 0022-3670. DOI: 10.1175/JPO2923.1. URL: http://dx.doi.org/10.1175/JPO2923.1.

Laxenaire, R., S. Speich, and A. Stegner (2020). "Agulhas Ring Heat Content and Transport in the South Atlantic Estimated by Combining Satellite Altimetry and Argo Profiling Floats Data." In: *Journal of Geophysical Research: Oceans* 125.9, pp. 1–27. ISSN: 21699291. DOI: 10.1029/2019JC015511.

Legg, Sonya and Alistair Adcroft (2003). "Internal wave breaking at concave and convex continental slopes." In: *Journal of Physical Oceanography* 33.11, pp. 2224–2246. ISSN: 00223670. DOI: 10.1175/1520-0485(2003)033<2224:IWBACA>2.0.CO;2.

Mahadevan, A., A. Tandon, and R. Ferrari (2010). "Rapid changes in mixed layer stratification driven by submesoscale instabilities and winds." In: *Journal of Geophysical Research: Oceans* 115.3, pp. 1–12. ISSN: 21699291. DOI: 10.1029/2008JC005203.

Mahadevan, Amala (2016). "The Impact of Submesoscale Physics on Primary Productivity of Plankton." In: *Annual Review of Marine Science* 8, pp. 161–184. ISSN: 19410611. DOI: 10.1146/annurev-marine-010814-015912.

Mahadevan, Amala et al. (2012). "Eddy-driven stratification initiates North Atlantic spring phytoplankton blooms." In: *Science* 336.6090, pp. 54–58. ISSN: 10959203. DOI: 10.1126/science.1218740.

Marez, Charly de, Noé J. Lahaye, and Jonathan Gula (2020a). "Interaction of the Gulf Stream with small scale topography: a focus on lee waves." In: *Scientific Reports* 10.1, pp. 1–10. ISSN: 20452322. DOI: 10.1038/s41598-020-59297-5.

Marez, Charly de et al. (2020b). "Study of the stability of a large realistic cyclonic eddy." In: *Ocean Modelling* 146.December 2019, p. 101540. ISSN: 14635003. DOI: 10.1016/j.ocemod.2019.101540. URL: https://doi.org/10.1016/j.ocemod.2019.101540.

Masur, G. T. and M. Oliver (2020). "Optimal balance for rotating shallow water in primitive variables." In: *Geophysical and Astrophysical Fluid Dynamics* 114.4-5, pp. 429–452. ISSN: 10290419. DOI: 10.1080/03091929.2020.1745789.

McWilliams, James C. (2016). "Submesoscale currents in the ocean." In: *Proceedings of the Royal Society A: Mathematical, Physical and Engineering Sciences* 472.2189. ISSN: 14712946. DOI: 10.1098/rspa.2016.0117.

Modis-Aqua (2019). *MODIS Aqua Sea Surface Temperature (SST) Data; v2019 Reprocessing*. Accessed: 2025-01-03. URL: https://oceandata.sci.gsfc.nasa.gov/MODIS-Aqua.

Molemaker, M. Jeroen, James C. McWilliams, and Xavier Capet (2010). "Balanced and unbalanced routes to dissipation in an equilibrated Eady flow." In: *Journal of Fluid Mechanics* 654, pp. 35–63. ISSN: 14697645. DOI: 10.1017/S0022112009993\-272.

Monterey, Grigory Isayev and Sydney Levitus (1997). "Seasonal variability of mixed layer depth for the world ocean." In: *NOAA atlas NESDIS; 14*. URL: https://repository.library.noaa.gov/view/noaa/49153.

Müller, M. et al. (2012). "Global M2 internal tide and its seasonal variability from high resolution ocean circulation and tide modeling." In: *Geophysical Research Letters* 39.19, pp. 1–6. ISSN: 00948276. DOI: 10.1029/2012GL053320.

Müller, Malte et al. (2015). "Toward an internal gravity wave spectrum in global ocean models." In: *Geophysical Research Letters* 42.9, pp. 3474–3481. ISSN: 0094-8276. DOI: 10.1002/2015GL063365. URL: https://agupubs.onlinelibrary.wiley.com/doi/10.1002/2015GL063365.

Munk, Walter H. (1966). "Abyssal recipes." In: *Deep-Sea Research and Oceanographic Abstracts* 13.4, pp. 707–730. ISSN: 00117471. DOI: 10.1016/0011-7471(66)90602-4.

Musgrave, Ruth et al. (2022). "Chapter 6 - The lifecycle of topographically-generated internal waves." In: *Ocean Mixing*. Ed. by Michael Meredith and Alberto Naveira Garabato. Elsevier, pp. 117–144. ISBN: 978-0-12-821512-8. DOI: https://doi.org/10.1016/B978-0-12-821512-8.00013-X. URL: https://www.sciencedirect.com/science/article/pii/B978012821512800013X.

Nikurashin, Maxim and Raffaele Ferrari (2011). "Global energy conversion rate from geostrophic flows into internal lee waves in the deep ocean." In: *Geophysical Research Letters* 38.8, pp. 1–6. ISSN: 00948276. DOI: 10.1029/2011GL046576.

— (2013). "Overturning circulation driven by breaking internal waves in the deep ocean." In: *Geophysical Research Letters* 40.12, pp. 3133–3137. ISSN: 00948276. DOI: 10.1002/grl.50542.

Olbers, Dirk, Jürgen Willebrand, and Carsten Eden (2012). *Ocean Dynamics*. Vol. 53. Berlin, Heidelberg: Springer Berlin Heidelberg. ISBN: 978-3-642-23449-1. DOI: 10.1007/978-3-642-23450-7. URL: http://link.springer.com/10.1007/978-3-642-23450-7.

Pichevin, Thierry, Doron Nof, and Johann Lutjeharms (1999). "Why are there Agulhas rings?" In: *Journal of Physical Oceanography* 29.4, pp. 693–707. ISSN: 00223670. DOI: 10.1175/1520-0485(1999)029<0693:WATAR>2.0.CO;2.

Qiu, Bo et al. (2019). "Reconstructing upper ocean vertical velocity field from sea surface height in the presence of unbalanced motion." In: *Journal of Physical Oceanography* 49.10, pp. 55–79. ISSN: 15200485. DOI: 10.1175/JPO-D-19-0172.1.

Richardson, Philip L. (2007). "Agulhas leakage into the Atlantic estimated with subsurface floats and surface drifters." In: *Deep-Sea Research Part I: Oceanographic Research Papers* 54.8, pp. 1361–1389. ISSN: 09670637. DOI: 10.1016/j.dsr.2007.04.010.

Riley, James J. and Marie-Pascale Lelong (2000). "Fluid Motions in the Presence of Strong Stable Stratification." In: *Annual Review of Fluid Mechanics* 32.1, pp. 613–

657. ISSN: 0066-4189. DOI: 10.1146/annurev.fluid.32.1.613. URL: https://www.annualreviews.org/doi/10.1146/annurev.fluid.32.1.613.

Sasaki, Hideharu et al. (2017). "Regionality and seasonality of submesoscale and mesoscale turbulence in the North Pacific Ocean." In: *Ocean Dynamics* 67.9, pp. 1195–1216. ISSN: 16167228. DOI: 10.1007/s10236-017-1083-y.

Schmid, Claudia et al. (2003). "Early evolution of an Agulhas Ring." In: *Deep-Sea Research Part II: Topical Studies in Oceanography* 50.1, pp. 141–166. ISSN: 09670645. DOI: 10.1016/S0967-0645(02)00382-X.

Schouten, Mathijs W. et al. (2000). "Translation, decay and splitting of Agulhas rings in the southeastern Atlantic Ocean." In: *Journal of Geophysical Research: Oceans* 105.C9, pp. 21913–21925. ISSN: 21699291. DOI: 10.1029/1999jc000046.

Schubert, R. et al. (2019). "Submesoscale Impacts on Mesoscale Agulhas Dynamics." In: *Journal of Advances in Modeling Earth Systems* 11.8, pp. 2745–2767. ISSN: 19422466. DOI: 10.1029/2019MS001724.

Schubert, René et al. (2020). "The submesoscale kinetic energy cascade: Mesoscale absorption of submesoscale mixed layer eddies and frontal downscale fluxes." In: *Journal of Physical Oceanography* 50.9, pp. 2573–2589. ISSN: 15200485. DOI: 10.1175/JPO-D-19-0311.1.

Scott, Robert B. and Brian K. Arbic (2007). "Spectral energy fluxes in geostrophic turbulence: Implications for ocean energetics." In: *Journal of Physical Oceanography* 37.3, pp. 673–688. ISSN: 00223670. DOI: 10.1175/JPO3027.1.

Sebastia Saez, Pablo, Carsten Eden, and Manita Chouksey (2024). "Evolution of Internal Gravity Waves in a Mesoscale Eddy Simulated Using a Novel Model." In: *Journal of Physical Oceanography* 54.4, pp. 985–1002. ISSN: 15200485. DOI: 10.1175/JPO-D-23-0095.1.

Shakespeare, Callum J. et al. (2021). "A New Open Source Implementation of Lagrangian Filtering: A Method to Identify Internal Waves in High-Resolution Simulations." In: *Journal of Advances in Modeling Earth Systems* 13.10. ISSN: 19422466. DOI: 10.1029/2021MS002616.

Silverthorne, Katherine E. and John M. Toole (2009). "Seasonal kinetic energy variability of near-inertial motions." In: *Journal of Physical Oceanography* 39.4, pp. 1035–1049. ISSN: 00223670. DOI: 10.1175/2008JPO3920.1.

Simmons, Harper L., Robert W. Hallberg, and Brian K. Arbic (2004). "Internal wave generation in a global baroclinic tide model." In: *Deep-Sea Research Part II: Topical Studies in Oceanography* 51.25-26 SPEC. ISS. Pp. 3043–3068. ISSN: 09670645. DOI: 10.1016/j.dsr2.2004.09.015.

Sören, Thomsen, Carsten Eden, and Lars Czeschel (2014). "Stability analysis of the Labrador current." In: *Journal of Physical Oceanography* 44.2, pp. 445–463. DOI: 10.1175/JPO-D-13-0121.1.

Stone, Peter H. (1966). "On Non-Geostrophic Baroclinic Stability." In: *Journal of the Atmospheric Sciences* 23.4, pp. 390–400. DOI: 10.1175/1520-0469(1966)023<0390:ONGBS>2.0.CO;2. URL: http://journals.ametsoc.org/doi/10.1175/1520-0469(1966)023%3C0390:ONGBS%3E2.0.CO;2.

— (1970). "On Non-Geostrophic Baroclinic Stability: Part II." In: *Journal of the Atmospheric Sciences* 27.5, pp. 721–726. ISSN: 0022-4928. DOI: 10.1175/1520-0469(1970)027<0721:ONGBSP>2.0.CO;2. URL: http://journals.ametsoc.org/doi/10.1175/1520-0469(1970)027%3C0721:ONGBSP%3E2.0.CO;2.

— (1972). "On Non-Geostrophic Baroclinic Stability: Part III. The Momentum and Heat Transports." In: *Journal of the Atmospheric Sciences* 29.3, pp. 419–426. ISSN: 0022-4928. DOI: 10.1175/1520-0469(1972)029<0419:ONGBSP>2.0.CO;2. URL: http://journals.ametsoc.org/doi/10.1175/1520-0469(1972)029%3C0419:ONGBSP%3E2.0.CO;2.

Su, Zhan et al. (2018). "Ocean submesoscales as a key component of the global heat budget." In: *Nature Communications* 9.1, pp. 1–8. ISSN: 20411723. DOI: 10.1038/s41467-018-02983-w. URL: http://dx.doi.org/10.1038/s41467-018-02983-w.

Susanto, R Dwi, Q Zheng, and Leonid Mitnik (2005). *Ocean internal waves observed in the Lombok Strait*. Vol. submitted. 4, pp. 1–16.

SWOT (2023). *The SWOT L3 SSH product, derived from the L2 SWOT KaRIn Low rate ocean data products (NASA/JPL and CNES), is produced and made freely available by AVISO and DUACS teams as part of the DESMOS Science team project*. Accessed: 2025-01-03. DOI: 10.24400/527896/A01-2023.018. URL: https://doi.org/10.24400/527896/A01-2023.018.

Talley, Lynne D. et al. (2011). *Descriptive Physical Oceanography*. Elsevier. ISBN: 978075-0645522. DOI: 10.1016/C2009-0-24322-4. URL: https://linkinghub.elsevier.com/retrieve/pii/C20090243224.

Thomas, Leif N. (2005). "Destruction of potential vorticity by winds." In: *Journal of Physical Oceanography* 35.12, pp. 2457–2466. ISSN: 00223670. DOI: 10.1175/JPO2830.1.

Uchida, Takaya et al. (2022). "Cloud-based framework for inter-comparing submesoscale-permitting realistic ocean models." In: *Geoscientific Model Development* 15.14, pp. 5829–5856. ISSN: 1991-9603. DOI: 10.5194/gmd-15-5829-2022. URL: https://gmd.copernicus.org/articles/15/5829/2022/.

Vanneste, Jacques (1993). "The Kelvin-Helmholtz instability in a non-geostrophic baroclinic unstable flow." In: *Mathematical and Computer Modelling* 17.1, pp. 149–154. ISSN: 08957177. DOI: 10.1016/0895-7177(93)90099-K.

Vanneste, Jacques and William R. Young (2022). "Stokes drift and its discontents." In: *Philosophical Transactions of the Royal Society A: Mathematical, Physical and Engineering Sciences* 380.2225, pp. 45–72. ISSN: 1364-503X. DOI: 10.1098/rsta.2021.0032. URL: https://royalsocietypublishing.org/doi/10.1098/rsta.2021.0032.

Verma, Vicky, Hieu T. Pham, and Sutanu Sarkar (2019). "The submesoscale, the finescale and their interaction at a mixed layer front." In: *Ocean Modelling* 140.January, p. 101400. ISSN: 14635003. DOI: 10.1016/j.ocemod.2019.05.004. arXiv: 1910.07625. URL: https://doi.org/10.1016/j.ocemod.2019.05.004.

Wong, Annie P.S. et al. (2020). "Argo Data 1999–2019: Two Million Temperature-Salinity Profiles and Subsurface Velocity Observations From a Global Array of Profiling Floats." In: *Frontiers in Marine Science* 7.July, pp. 1–23. ISSN: 22967745. DOI: 10.3389/fmars.2020.00700.

Wunsch, Carl and Raffaele Ferrari (2004). "Vertical mixing, energy, and the general circulation of the oceans." In: *Annual Review of Fluid Mechanics* 36.1, pp. 281–314. ISSN: 00664189. DOI: 10.1146/annurev.fluid.36.050802.122121.

Xu, Xiaobiao et al. (2022). "On the Spatial Variability of the Mesoscale Sea Surface Height Wavenumber Spectra in the Atlantic Ocean." In: *Journal of Geophysical Research: Oceans* 127.10, pp. 1–18. ISSN: 21699291. DOI: 10.1029/2022JC018769.

Yang, Luwei et al. (2021). "The Impact of Lee Waves on the Southern Ocean Circulation." In: *Journal of Physical Oceanography* 51.9, pp. 2933–2950. ISSN: 15200485. DOI: 10.1175/JPO-D-20-0263.1.

Yu, Xiaolong et al. (2019). "An annual cycle of submesoscale vertical flow and restratification in the upper Ocean." In: *Journal of Physical Oceanography* 49.6, pp. 1439–1461. ISSN: 15200485. DOI: 10.1175/JPO-D-18-0253.1.

Zhang, Jinchao, Zhiwei Zhang, and Bo Qiu (2023). "Parameterizing Submesoscale Vertical Buoyancy Flux by Simultaneously Considering Baroclinic Instability and Strain-Induced Frontogenesis." In: *Geophysical Research Letters* 50.8, pp. 1–10. ISSN: 19448007. DOI: 10.1029/2022GL102292.

Zhang, Zhiwei et al. (2021). "Submesoscale currents in the subtropical upper ocean observed by long-term high-resolution mooring arrays." In: *Journal of Physical Oceanography* 51.1, pp. 187–206. ISSN: 15200485. DOI: 10.1175/JPO-D-20-0100.1.

Zheng, Ruixi and Zhiyou Jing (2024). "Diurnal Variability of Mixed Layer Overturning Instabilities From Glider Array Observations in the South China Sea." In: *Geophysical Research Letters* 51.11. ISSN: 19448007. DOI: 10.1029/2023GL107694.

EIDESSTATTLICHE VERSICHERUNG | DECLARATION ON OATH

Hiermit erkläre ich an Eides statt, dass ich die vorliegende Dissertationsschrift selbst verfasst und keine anderen als die angegebenen Quellen und Hilfsmittel benutzt habe. Sofern im Zuge der Erstellung der vorliegenden Dissertationsschrift generative Künstliche Intelligenz (gKI) basierte elektronische Hilfsmittel verwendet wurden, versichere ich, dass meine eigene Leistung im Vordergrund stand und dass eine vollständige Dokumentation aller verwendeten Hilfsmittel gemäß der Guten wissenschaftlichen Praxis vorliegt. Ich trage die Verantwortung für eventuell durch die gKI generierte fehlerhafte oder verzerrte Inhalte, fehlerhafte Referenzen, Verstöße gegen das Datenschutz- und Urheberrecht oder Plagiate.

Hamburg, February 4, 2025

Moritz Epke

Hinweis / Reference

Die gesamten Veröffentlichungen in der Publikationsreihe des MPI-M
„Berichte zur Erdsystemforschung / Reports on Earth System Science“,
ISSN 1614-1199

sind über die Internetseiten des Max-Planck-Instituts für Meteorologie erhältlich:
https://mpimet.mpg.de/forschung/publikationen

All the publications in the series of the MPI -M
„Berichte zur Erdsystemforschung / Reports on Earth System Science“,
ISSN 1614-1199

are available on the website of the Max Planck Institute for Meteorology:
https://mpimet.mpg.de/en/research/publications